NANOMITES TO NANO-COATINGS: MANIPULATION OF PLASMONIC GOLD NANOPARTICLE INTERFACES

by

Cady Anne Lancaster

A dissertation submitted to the faculty of
The University of Utah
in partial fulfillment of the requirements for the degree of

Doctor of Philosophy

Department of Chemistry

The University of Utah

May 2017

The University of Utah Graduate School

STATEMENT OF DISSERTATION APPROVAL

The dissertation of **Cady Anne Lancaster**

has been approved by the following supervisory committee members:

Jennifer Shumaker-Parry	, Chair	**Dec. 8, 2016** Date Approved
Joel Mark Harris	, Member	**Dec. 8, 2016** Date Approved
Scott L. Anderson	, Member	**Dec. 8, 2016** Date Approved
Bruce K. Gale	, Member	**Dec. 8, 2016** Date Approved
Marc D. Porter	, Member	**Dec. 8, 2016** Date Approved

and by **Cynthia Burrows**, Chair/Dean of

the Department/College/School of **Chemistry**

and by David B. Kieda, Dean of The Graduate School.

ABSTRACT

Plasmonic nanomaterials have tunable optical properties that are exploited for sensing applications. When designing nanoparticle substrates, trade-offs are often made: sensitivity or stability, customization or cost. To narrow the gap of these trade-offs, research focused on optimization parameters for nanoparticle substrates. A protective oxide coating was introduced to heterogeneous nanoparticle surfaces to improve substrate robustness and chemical stability after long-term storage. In order to maintain sensitivity, methods to control the chemical reactivity of the substrates were optimized by improving the surface chemistry for favorable thin film deposition. Improved thin film deposition addressed the challenges of transporting nanoparticle substrates for collaborative work. A novel nanoparticle substrate capable of high surface enhancement for Raman spectroscopy and increased sensitivity to the local refractive index was also designed. Structural modifications of fabricated nanostructures were achieved via synthetic decorations to improve sensitivity while maintaining scalability.

To increase nanostructure robustness, ultraviolet ozone (UVO) and oxygen plasma treatments were investigated to determine the impact of these standard cleaning techniques on the nucleation of alumina with atomic layer deposition (ALD) on heterogeneous substrates of nanostructured gold (Au) on glass. In addition to physical protection, introducing a protective oxide preserved the chemical reactivity of the

nanostructure for on-site functionalization by our collaborators. These areas of research addressed the challenges of transporting nanoparticle substrates over large distances and variable time scales. It was demonstrated that the use of oxygen plasma was detrimental to Au nanodisks. UVO treatments successfully cleaned Au and aged alumina surfaces for continued alumina deposition without damaging the structure. Alumina ALD was also used to probe the behavior of nanocrescent arrays from the visible to IR. Empirical and theoretical approaches were used to describe the behavior of the plasmonic near-field.

By uniting top-down fabrication with bottom-up synthesis approaches, highly branched gold “nanomite” decorations were synthesized on fabricated gold nanoparticle “hosts.” To maintain scalability of fabricated structures, a one-pot synthesis was used that incorporated a low temperature phase to improve nucleation on the minimally crystalline fabricated structures. By increasing the density of plasmonic hotspots via branching, the response of Au nanoparticles for surface-enhanced Raman spectroscopy increased 200-fold over undecorated structures. The nanomite synthesis is applicable to other fabricated systems without compromising the host nanoparticles’ inherent plasmonic properties, such as polarization-dependent resonance modes.

TABLE OF CONTENTS

LIST OF TABLES

ACKNOWLEDGEMENTS

I would like to thank Dr. Jennifer Shumaker-Parry for her research guidance and all of the opportunities she has provided for me. Her continued support and advice about life, jobs, and the balance that goes along with that has been invaluable. Jennifer has funded my attendance to fantastic conferences that have introduced me to a broader community and inspired significant portions of my research. Thank you, Jennifer. I would not be the chemist I am today without you.

I would like to thank all of my friends and Utah family who have kept me sane! These last few years have been interesting and having all of your support has eased the bumps in the road.

Finally, I would like to thank my Family. Like many youngest children, I owe my resilience and thick skin to my two brothers. These are qualities few grad students can survive without. Finally, I would like to thank my parents for their moral support and pushing me to excel at whatever I chose to do.

CHAPTER 1

INTRODUCTION

The plasmonic properties of gold and silver nanoparticles have been observed in human-made artifacts as far back as the fourth century. In the seventeenth century, Roman metallurgists constructed the Lyucurgus Cup, which is the earliest known example of dichroic glass and the rarest example of diatretum, or carved glass, craftsmanship. When illuminated from within, the chalice glows blood red, and when illuminated from the front, the chalice is jade green (Figure 1.1). The intentional utilization and characterization of these peculiar optical properties for nanoscale gratings did not resurface until the 1900s.[1-3] "Plasmonics," the term used to describe this particular field of science, was not formalized until 1956.[4]

The gold (Au) and silver (Ag) nanoparticles in the Lycurgus Cup exhibit localized surface plasmon resonance (LSPR), a collective oscillation of free electrons caused by incident light. This optical phenomenon occurs when the wavelength of incident light is much larger than the diameter of the metallic nanoparticle; as the electromagnetic (EM) wave passes over the particle, the electric field component perturbs and repels the free electrons at the metal-dielectric interface. This generates coherently oscillating electrons that form regions of high electron density, called hotspots, which create an evanescent

Figure 1.1 Lycurgus Cup. Left: Illuminated from within. Right: Front lit. Reprinted with permission by The Trustees of the British Museum.

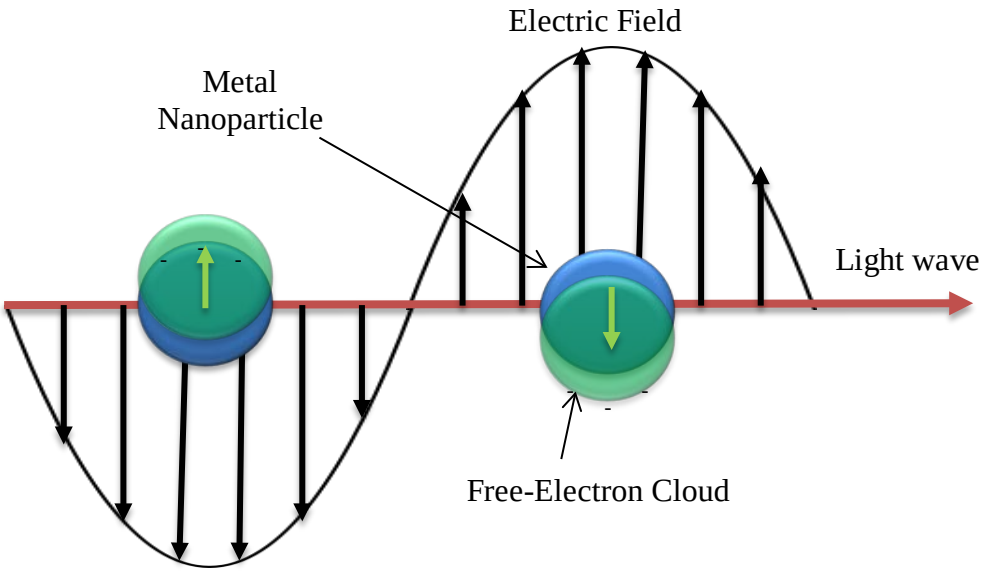

Figure 1.2 Diagram of localized surface plasmon resonance where conduction electrons in the nanoparticle are constrained into dipolar oscillation due to strong coupling with incident light.

wave within the near-field of the nanostructure (Figure 1.2).[5] The enhanced EM field generated by the LSPR is sensitive to changes in the local refractive index (RI) and can amplify chemical signals. The signal enhancement is utilized in a variety of spectroscopic applications such as surface-enhanced Raman spectroscopy (SERS), infrared absorption (SEIRA), and in ex vivo and in vivo label-free biosensing.[6-19] Because of the promising applications of surface-enhanced substrates, the field of LSPR substrate design and application has been growing rapidly. One organization that is focused on the utilization of these structures to probe single chemical events in real space and time is the Chemistry at the Space Time Limit (CaSTL) Center for Chemical Innovation.

The National Science Foundation funded CaSTL Center is focused on collaborative work between several groups at Northwestern University, University of Utah, University of California Irvine, Penn State, and University of Pittsburgh. In collaboration with this Center, my research has focused on manipulating the near-field of Au plasmonic nanoparticles (PNPs) for high surface-enhancement and protecting nanostructures for time-resolved measurements. I have also focused on investigating methods to maintain the chemical reactivity of nanoparticle surfaces for onsite functionalization. In addition to being fundamentally interesting to the field of plasmonics, these areas of research address the challenges of transporting nanoparticle substrates over large distances and variable time scales (days to weeks). When a metal nanoparticle sample is fabricated, it must be chemically and physically stable for transport from Utah to any one of the Center's locations. There is also the possibility that some form of chemical functionalization needs to occur onsite prior to spectroscopy and so the surface chemistry of the structure must be known. It has been my goal to develop a

novel nanoparticle substrate capable of high surface enhancement for a broad EM range and develop an alumina thin-film methodology to protect nanostructures from rigorous analysis performed by the CaSTL Center while maintaining high sensitivity for spectroscopic applications.

1.1 Surface Enhancement Strategies

There are many current strategies used to enhance the sensitivity of nanoparticles for sensing applications. Three of these are detailed by Guo et al. in a thorough review.[20] They identified (i) refractive index sensing, (ii) plasmon coupling, and (iii) nanoparticle growth as the most predominant methods of LSPR sensing. For refractive index (RI)-based sensing, the broad categories of composition, size, shape, assembly, and resonance coupling can be tuned to increase sensitivity and spectral range. The composition of the plasmonic nanostructure is highly dependent on the application and wavelength regime. Generally, noble metals are preferred because they are least susceptible to environmental corrosion and, due to the cost and ease of fabrication, silver (Ag) and gold (Au) are the most common plasmonic materials. Gold is a specifically advantageous material due to its stability in biosensing applications.[6] Other non-noble metals are also used; for example, aluminum is used for ultraviolent (UV) plasmonics due to its relatively low losses compared to Ag and Ag in the UV.[21-23] Beyond composition, the shape of a nanoparticle improves refractive index sensing and overall sensitivity via antenna effects: sharp-tipped nanostructures confine the electric field to a smaller volume, which leads to larger field enhancements.[24]

The second predominant method, plasmon coupling, can be used for colorimetric

sensing (LSPR shift) by increasing aggregate size via enzyme, antibody, protein, and/or nanoparticle coupling. By minimizing the distance between nanoparticle aggregates, a stronger local coupling occurs, which can be observed using scattering signals with methods like dark-field microscopy. Among plasmon coupling techniques are methods that combine top-down and bottom-up fabrication methods to take advantage of the strong local field of coupled nanoparticles. Using a nanorod-impregnated, thermos-responsive polymer, Nguyen et al.[25] developed a nanotriangle array that uses the enhancement created by coupling nanorods with the nanotriangle surface. As the temperature changes, the polymer contracts and brings the two plasmonic particles together which then alters the LSPR.

The final strategy for sensing is to control nanoparticle growth. In these methods, enzyme catalyzed reactions are used to alter the presence of reducing agents that changes the sizes of the nanoparticles. This work has primarily involved deoxyribonucleic acid (DNA) targets, which has shown improved sensitivity over traditional fluorophore techniques by nearly two orders of magnitude.[26-27]

Beyond the overall sensing strategies outlined above, the symmetry of nanoparticles and nanoparticle assemblies also plays a role in application. For example, anisotropic plasmonic structures support multiple resonance modes across a broad spectral range. When these structures are arrayed in nonrandom, repeating orientation, the resonance modes are polarization-dependent and can be used as substrates for multiple probe and sensing techniques.[28-30] The efficacy of the various techniques depends on the method of nanoparticle production: top-down fabrication or bottom-up synthesis.

1.1.1 *Bottom-Up Synthesis*

Bottom-up nanoparticle production uses synthetic techniques to develop an astounding variety of shapes via facet passivation. Synthesis of Au nanoparticles can take many forms: coprecipitation, chemical reduction, photochemical reduction, thermal decomposition, and others.[28, 31-38] To increase signal enhancement of synthetic nanoparticles, structures can be randomly aggregated or dimerized in a controllable fashion. Both techniques generate nanogaps that are known to have highly concentrated EM fields.[39-41] Another option is to generate sharp tips to confine the EM near-field. Nanorods, prisms, and nanostars are among the many possible synthetic routines.[37, 42] In general, there are two methods of synthetic design: seed and non-seed growth. The use of the traditional seed method relies on the passivation of crystalline facets of preformed nanoparticles that leads to reduction of the Au precursor in a specific orientation. Due to the need for seed nanoparticles, multiple purification steps are required. Non-seed strategies, or "one-pot" syntheses, have the benefit of fewer steps, and therefore fewer reactants to purify from the completed nanostructures.[43-44] Facet passivation is well-studied and many different geometries have been developed in addition to nanostars including nanocubes, nanorods, dumbbells, and dog bones.[37, 45-48] Using different capping agents, reactions can be run sequentially to target different facets or deposit additional metals.

While synthetic nanoparticles can have very sensitivity LSPR responses to ideal analyte conditions and solutions, they are vulnerable to complex solutions. Generally, solutions with high pH, high ionic strength, or biological salt conditions lead to nanoparticle instability. This is a particular problem for surface-enhanced Raman

scattering (SERS), where particle instability leads to undesired aggregation, and thus signal fluctuation and poor reproducibility.[49] Nanostars, one of the most promising SES synthetic substrates, are only stable in solution for 5 h to 3 weeks depending on synthesis protocol, limiting their commercial viability.[43, 50-51] To overcome these issues, patterned SES substrates using top-down fabrication have been used to control nanoparticle aggregation and increase reproducibility.[52-53]

1.1.2 *Top-Down Fabrication*

Top-down approaches to nanoparticle fabrication begin with bulk material that is physically scaled via vapor deposition (typically with nanoscale templates), laser generation, or direct write techniques. Top-down fabrication generates nanoparticle substrates that are well-ordered and not prone to aggregation. As a general rule, nanostructures are prepared by templating or periodic array writing and fixed to a solid substrate. Exceptions to this rule are laser-ablation and grinding techniques which are used to generate high yields of nanoparticles through films. However, the nanoparticle shape is limited and, until recently, the laser-ablation techniques lacked size control.[12, 23, 54-57] The most popular techniques for plasmonics are electron-beam lithography and colloidal lithography. Electron-beam lithography is used to direct-write periodic arrays but it is expensive and has a low yield. Two colloidal lithography techniques, nanosphere lithography (NSL) and nanosphere template lithography (NTL), are low cost, high yield techniques that use inexpensive polystyrene nanosphere templates to generate a variety of shapes in either arrayed or dispersed patterns.[23, 56-60]

Most colloidal lithography techniques use similar procedures in slightly different

sequences to introduce novel shapes and geometries. In NSL, nanosphere templates are deposited on a substrate followed by metal deposition. The metal deposits into the interstitial between the close-packed nanosphere templates and when the templates are removed the metal remains in the shape of a nanotriangle (Figure 1.3A). Using NSL, Van Duyne has established the use of silver nanotriangles as a viable SERS substrate.[5, 52, 55, 61] The Shumaker-Parry group has specialized in the fabrication of nanocrescents (NC) using NTL and copper mask-NTL.[23, 57] In the NTL process, NCs are fabricated using precise angles and template shrinking to in-fill the shadow of the template with metal (Figure 1.3B).[57, 60] After template deposition, metal is deposited at an angle. The substrate is etched normal to the surface to remove any material not covered by the template. When the template is removed, metal remains in the former shadow of the nanostructure as a nanocrescent. The sharp tips generate strong near-fields, which is ideal for surface-enhanced spectroscopies.[28, 62] By using the polarization anisotropy of nanocrescents (NCs), the resonance modes can be induced by controlling the wavelength and polarization of the incident field, which is ideal for CaSTL applications.[23, 60, 62-65] By changing the metal, angle of metal deposition, size of the template, and rotation during metal deposition, nanocrescents can easily be tuned from the UV to the IR.[23, 64-65] Other colloidal lithography techniques change the order of template and metal deposition to access new structures such as rings and nanodisks (Figure 1.3C and D).[10-11]

1.2 Nanoparticle Protection: Atomic Layer Deposition

Plasmonic nanoparticles have disadvantages related to high surface sensitivity and defined structure, which have limited their utility. One disadvantage is the fragility of the

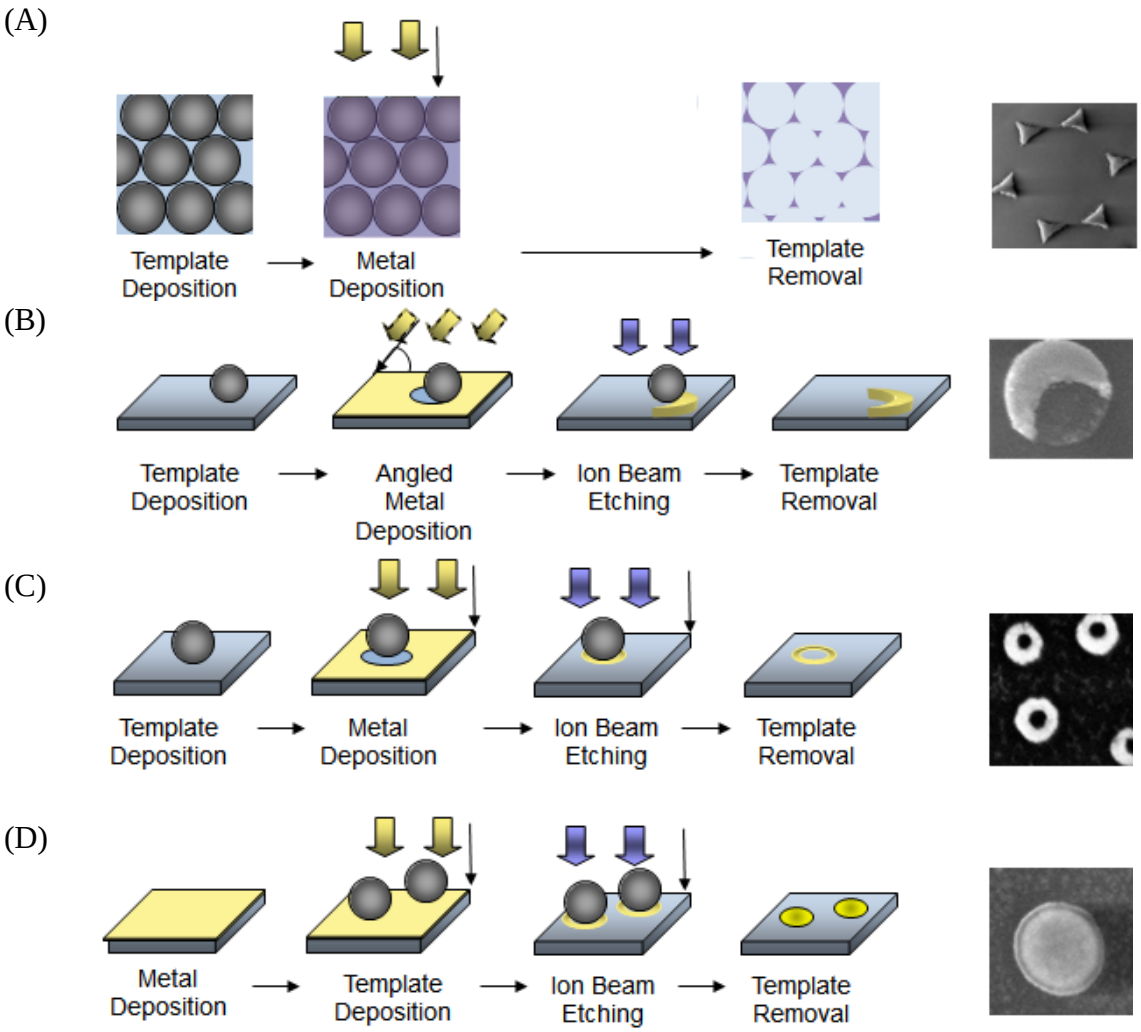

Figure 1.3. Colloidal template lithography depicting; (A) fabrication of nanotriangles via nanosphere lithgraphy, (B) fabrication of nanocrescents via nanosphere template lithography and (C) nanorings and (D) nanodisks.

structures, as PNPs lose their distinctive LSPR or enhancement over time due to structural degradation from cleaning or aggressive spectroscopies. For example, nanoparticles are generally not reusable for methods such as femtosecond(fs)-laser excitation because the sharp tips will deform.[66] Another challenge is their poor shelf life due to changes in surface properties over very short periods. The relative hydrophobicity and wettability of a metal is an important factor and can be impaired with time: the surface of Au will develop oxide layers and adsorb hydrocarbons, both of which decrease sensitivity and increase hydrophobicity.[67-69] In addition to sensitivity concerns, it is important to maintain native surface properties because many applications of PNPs require surface modification of the Au structures. There is also interest in using the near-field to enhance signals but concern over the influence of the near-field on the chemistry itself. By introducing an oxide spacer, the metal surface is distanced from the molecules or reaction being interrogated allowing the system to be probed without being impacted by the strong EM near field of the nanoparticle. Currently, evidence of "hot-electrons" and plasmon mediated chemistry is being proposed by some.[70-71] The use of the oxide spacer to potentially control these effects may be necessary in the future.

In the past, these challenges limit the use of PNPs in surface-enhanced spectroscopy and sensing. However, these challenges have been largely overcome by incorporating an ultra-thin, defect-free protective coating that is able to cover complex, high aspect ratio structures over large surface areas via atomic layer deposition (ALD). ALD provides excellent spatial resolution due to the ability to deposit angstrom-thick monolayers of Al_2O_3. A conformal thin film is achieved via sequential self-limiting surface reactions of trimethylaluminum (TMA) and water resulting in an Al_2O_3 film.[72-73]

The driving force of the reaction is the strong formation of the Al-O bond. With a reaction enthalpy of -1573 kJ/mol, ALD of Al_2O_3 is one of the most energetically favorable for any ALD process.[74] The overall reaction is:

$$2\ Al\ (CH_3)_3 + 3H_2O \rightarrow Al_2O_3\ + 3CH_4 \qquad \Delta H = -1573\ \text{kJ/mol} \qquad (1.1)$$

This highly favorable enthalpy also makes Al_2O_3 the most widely used low-temperature ALD system. Additionally, the growth of Al_2O_3 is one of the most understood mechanisms in atomic layer deposition and many of methods have been used to confirm the process.[72-75]

The physical robustness of Al_2O_3 protected structures has been documented for fs-laser excitation of sharp-tipped nanotriangles and for thermal cleaning treatments up to 400 °C of island films.[19, 66] These studies have shown that Al_2O_3 protected structures retain morphology and physical properties under harsh experimental and cleaning conditions. Despite the many benefits of this system, Al_2O_3 deposition comes with its own considerations.

On most metal surfaces, Al_2O_3 films form via island growth; nucleating at a few defect sites from which the islands grow together after several deposition cycles to coalesce into a film.[74] Island growth can lead to pinhole defects when the islands do not completely coalesce. Island growth can also lead to irregular surfaces if the film nucleates inefficiently due to surface chemistry mismatch. For example, on hydrophobic, -CH_3 terminated self-assembled monolayers (SAM) surfaces, Al_2O_3 nucleation occurs via water droplets on the surface that lead to dome-like structures. On a hydrophilic surface of OH-SiO_2, water droplets do not form due to increased wettability resulting in a smooth surface after deposition. The difference in surface wettability of the hydrophobic and

hydrophilic surfaces highlights the need to control surface nucleation to maintain atomically smooth morphologies.[76]

Temperature also plays in an important role in the nucleation and growth per cycle (GPC) of alumina (Al_2O_3). At very low temperatures, the GPC is low and purge times must be increased due to slow surface reaction kinetics and low vapor pressure of the reactants.[77] At high temperatures, there is a lower hydroxyl group concentration due to dehydroxlyation, which leads to lower GPC due to inferior nucleation. High-temperature depositions can also be problematic for sharp-tipped nanostructures due to the low melting point of nanostructured Au. Therefore, low-temperature ALD is favored for PNPs.

Thin films for PNPs are balanced between thermal and physical protection (which favors thicker films) and sensitivity of the plasmonic near-field (which favors thin films). Due to the evanescent decay of the plasmonic near-field, the surface enhancement drops off exponentially as the analyte of interest is removed from the metal surface. In order to establish defect-free, ultrathin films at low temperatures, the nucleation of Al_2O_3 must be controlled via surface cleaning and preparation. Al_2O_3 thin films and bulk Au films are both well-studied systems and achieving hydrophilic *bulk* Au surfaces is a well-known process.[67, 78-79] However, the interaction of these cleaning techniques on *nanostructured* surfaces is not well-studied. To understand why Al_2O_3 nucleation needs to be studied on nanoparticles as intensively as it was studied on bulk films, one needs to understand the source of defects in films.

On polished copper (Cu) surfaces, the defect density of Al_2O_3 via ALD is 8 defects cm^{-2}.[80] On an evaporated aluminum (Al) film, which is inherently terminated in

Al_2O_3, the defect density is 6000 defects cm^{-2}.[81] The key difference between evaporated Al and polished Cu is the surface roughness. Using atomic force microscopy, copper-plate electrodeposition, and water vapor transmission rates, a relatively low-temperature (80 °C) ALD study was performed on copper and calcium (Ca) films to determine the defect rate as a function of Al_2O_3 thickness.[81-83] The authors found that defects would form in any region where there was a step-edge in the surface. When depositing a 5 nm Al_2O_3 film on calcium, a 7 nm step-edge of the Ca film always resulted in defects of the alu Al_2O_3. The defects were attributed to poor Al_2O_3 nucleation or increased condensation. The critical thickness for the Al_2O_3 film was 25 nm: at this thickness, the defect density compared to film thickness was no longer linearly dependent. For PNPs, 25 nm is well beyond the reach of the plasmonic near-field which eliminates utility of surface-enhanced sensing. Most research evaluating the use of Al_2O_3 coatings for PNPs focuses on 1 to 5 nm coatings due to the rapid plasmonic decay off after 5 nm.[19, 66] For a nanostructured surface, the roughness is extremely high and every contour of the nanoparticle becomes an opportunity for thin-film defects. Therefore, finding ways to decrease defect density while maintaining a < 5 nm thin film is crucial to the long-term use of PNPs.

1.3 Dissertation Outline

1.3.1 *Surface Preparation of Gold Nanostructures*

Chapter 1 details the investigation of two methods for Au nanoparticle (AuNP) surface preparation: oxygen plasma and UVO treatment. Both techniques have surface chemistry benefits and are used extensively in chemistry and engineering to generate the

hydrophilic surfaces needed for uniform Al_2O_3 deposition.[67, 79, 84] At room temperature, UVO treatments result in a rapid loss of surface bound hydrocarbons and oxycarbons, and treated Au films are stable to repeated rinses with water and ethanol without changes to surface morphology.[85] Oxygen plasma is used in microelectromechanical systems fabrication to clean surfaces without increasing surface roughness.[79] The benefits of oxygen plasma on Au films include the prevention of protective Au_2O_3 layer removal and negligible mechanical erosion.[86] However, there have been conflicting reports on the impact of oxygen plasma on nanoparticles.[87-88] Using the LSPR response and physical evidence shown by scanning electron microscopy, it was established that oxygen plasma treatments are detrimental to nanoparticles. Moreover, we proposed the use of UVO to clean heterogeneous Au nanoparticle surfaces as a superior technique for preparation of thin film deposition when a hydrophilic surface is required.

1.3.2 *Near-Field Behavior of Nanocrescents from the Visible to Mid-IR*

In order to rationally design and manipulate the physical and chemical properties of nanoparticles, the relationship between the physical properties and the optical properties of the nanostructure need to be fully understood. Chapter 2 uses ALD of Al_2O_3 to show the decay-length dependence and behavior of polarization-dependent resonance modes of Au nanocrescents over a broad spectral range. Finite-difference time-domain simulations provide insight to behavior of the EM near-field with increasing Al_2O_3 thickness.

1.3.3 *Nanomite Synthesis*

Nanostars have the largest signal-enhancements in plasmonics due to the sharpness and large number of tips per particle. However, aggregation is a significant challenge that has hindered their further development. To overcome this challenge, top-down fabrication methods have been used to design substrates that are not sensitive to environmental factors that contribute to aggregation.

Chapter 4 describes the development of a hybrid substrate that uses affordable and simple methods from both top-down fabrication and bottom-up synthetic techniques. To avoid using expensive electron-beam lithography or other traditional, time-intensive lithographic techniques, nanosphere lithography (NSL) was employed. NSL is a simple two-step process of polystyrene nanosphere template deposition and Au evaporation to generate a well-patterned array of nanotriangles.[58] Using a one-pot synthesis, the nanostructure array acted as the seed, or "host," for a nanostar-based synthesis that did not require any additional purification beyond rinsing the solid substrate. The combination of these two techniques generates fixed substrates with branched decorations, or "nanomites."

1.3.4 *Nanomite Spectroscopy*

Chapter 5 shows the preliminary spectroscopic applications of nanomite decorated Au nanotriangles and Au nanocrescents arrays. By using arrayed structures, a large surface density substrate is fabricated that can be used for spectroscopy, and the optical properties of the host nanoparticle maintain polarization dependence resonance modes. The combined fabrication/synthesis technique allows any fabricated nanoparticle

to be used as a host for the synthesis of branched nanoparticles to improve sensitivity for refractive index sensing and increase enhancement for SERS.

1.4 References

1. Barber, D. J.; Freestone, I. C. An Investigation of the Origin of the Colour of the Lycurgus Cup by Analytical Transmission Electron Microscopy. *Archaeometry* **1990,** *32* (1), 33-45.

2. Wood, R. W. In *On a Remarkable Case of Uneven Distribution of Light in a Diffraction Grating Spectrum*, Proceedings of the Physical Society of London, 1902; p 269.

3. Garnett, J. C. M. In *Colours in Metal Glasses and in Metallic Films*, Philosophical Transactions of the Royal Society of London. 1904; p 385.

4. Pines, D. Collective Energy Losses in Solids. *Rev. Mod. Phys.* **1956,** *28* (3), 184-198.

5. Willets, K. A.; Van Duyne, R. P. Localized Surface Plasmon Resonance Spectroscopy and Sensing. *Ann. Rev. Phys. Chem.* **2007,** *58* (1), 267-297.

6. Soares, L.; Csaki, A.; Jatschka, J.; Fritzsche, W.; Flores, O.; Franco, R.; Pereira, E. Localized Surface Plasmon Resonance (Lspr) Biosensing Using Gold Nanotriangles: Detection of DNA Hybridization Events at Room Temperature. *Analyst* **2014,** *139* (19), 4964-4973.

7. Doria, G.; Conde, J.; Veigas, B.; Giestas, L.; Almeida, C.; Assunção, M.; Rosa, J.; Baptista, P. V. Noble Metal Nanoparticles for Biosensing Applications. *Sensors* **2012,** *12* (2), 1657.

8. Raphael, M. P.; Christodoulides, J. A.; Mulvaney, S. P.; Miller, M. M.; Long, J. P.; Byers, J. M. A New Methodology for Quantitative Lspr Biosensing and Imaging. *Anal. Chem.* **2011,** *84* (3), 1367-1373.

9. He, X.; Wang, K.; Cheng, Z. In Vivo Near-Infrared Fluorescence Imaging of Cancer with Nanoparticle-Based Probes. *Wiley Interdiscip. Rev. Nanomed. Nanobiotechnol.* **2010,** *2* (4), 349-366.

10. Aizpurua, J.; Hanarp, P.; Sutherland, D. S.; Käll, M.; Bryant, G. W.; García de Abajo, F. J. Optical Properties of Gold Nanorings. *Phys. Rev. Lett.* **2003,** *90* (5), 057401.

11. Hanarp, P.; Käll, M.; Sutherland, D. S. Optical Properties of Short Range Ordered Arrays of Nanometer Gold Disks Prepared by Colloidal Lithography. *J. Phys.*

Chem. B **2003,** *107* (24), 5768-5772.

12. Neddersen, J.; Chumanov, G.; Cotton, T. M. Laser Ablation of Metals: A New Method for Preparing Sers Active Colloids. *Appl. Spectrosc.* **1993,** *47* (12), 1959-1964.

13. Kahl, M.; Voges, E.; Kostrewa, S.; Viets, C.; Hill, W. Periodically Structured Metallic Substrates for Sers. *Sens. Actuators, B* **1998,** *51* (1–3), 285-291.

14. Kennedy, B. J.; Spaeth, S.; Dickey, M.; Carron, K. T. Determination of the Distance Dependence and Experimental Effects for Modified Sers Substrates Based on Self-Assembled Monolayers Formed Using Alkanethiols. *J. Phys. Chem. B* **1999,** *103* (18), 3640-3646.

15. Sánchez-Cortés, S.; Domingo, C.; García-Ramos, J. V.; Aznárez, J. A. Surface-Enhanced Vibrational Study (Seir and Sers) of Dithiocarbamate Pesticides on Gold Films. *Langmuir* **2001,** *17* (4), 1157-1162.

16. Le, F.; Brandl, D. W.; Urzhumov, Y. A.; Wang, H.; Kundu, J.; Halas, N. J.; Aizpurua, J.; Nordlander, P. Metallic Nanoparticle Arrays: A Common Substrate for Both Surface-Enhanced Raman Scattering and Surface-Enhanced Infrared Absorption. *ACS Nano* **2008,** *2* (4), 707-718.

17. Küstner, B.; Gellner, M.; Schütz, M.; Schöppler, F.; Marx, A.; Ströbel, P.; Adam, P.; Schmuck, C.; Schlücker, S. Sers Labels for Red Laser Excitation: Silica-Encapsulated Sams on Tunable Gold/Silver Nanoshells. *Angew. Chem. Int.* **2009,** *48* (11), 1950-1953.

18. Bantz, K. C.; Meyer, A. F.; Wittenberg, N. J.; Im, H.; Kurtulus, O.; Lee, S. H.; Lindquist, N. C.; Oh, S.-H.; Haynes, C. L. Recent Progress in Sers Biosensing. *PCCP* **2011,** *13* (24), 11551-11567.

19. Mahurin, S. M.; John, J.; Sepaniak, M. J.; Dai, S. A Reusable Surface-Enhanced Raman Scattering (Sers) Substrate Prepared by Atomic Layer Deposition of Alumina on a Multi-Layer Gold and Silver Film. *Appl. Spectrosc.* **2011,** *65* (4), 417-422.

20. Guo, L.; Jackman, J. A.; Yang, H.-H.; Chen, P.; Cho, N.-J.; Kim, D.-H. Strategies for Enhancing the Sensitivity of Plasmonic Nanosensors. *Nano Today* **2015,** *10* (2), 213-239.

21. Meziani, M. J.; Bunker, C. E.; Lu, F.; Li, H.; Wang, W.; Guliants, E. A.; Quinn, R. A.; Sun, Y.-P. Formation and Properties of Stabilized Aluminum Nanoparticles. *ACS Appl. Mat. Interfaces* **2009,** *1* (3), 703-709.

22. Knight, M. W.; King, N. S.; Liu, L.; Everitt, H. O.; Nordlander, P.; Halas, N. J. Aluminum for Plasmonics. *ACS Nano* **2014,** *8* (1), 834-840.

23. Swartz, M.; Rodriguez, M.; Quast, A. D.; Cooper, C. T.; Blair, S.; Shumaker-Parry, J. S. Aluminum Nanocrescent Plasmonic Antennas Fabricated by Copper Mask Nanosphere Template Lithography. *J. Phys. Chem. C* **2016**.

24. Novotny, L.; Bian, R. X.; Xie, X. S. Theory of Nanometric Optical Tweezers. *Phys. Rev. Lett.* **1997,** *79* (4), 645-648.

25. Nguyen, M.; Kanaev, A.; Sun, X.; Lacaze, E.; Lau-Truong, S.; Lamouri, A.; Aubard, J.; Felidj, N.; Mangeney, C. Tunable Electromagnetic Coupling in Plasmonic Nanostructures Mediated by Thermoresponsive Polymer Brushes. *Langmuir* **2015,** *31* (46), 12830-12837.

26. Zayats, M.; Baron, R.; Popov, I.; Willner, I. Biocatalytic Growth of Au Nanoparticles: From Mechanistic Aspects to Biosensors Design. *Nano Lett.* **2005,** *5* (1), 21-25.

27. Taton, T. A.; Mirkin, C. A.; Letsinger, R. L. Scanometric DNA Array Detection with Nanoparticle Probes. *Science* **2000,** *289* (5485), 1757-1760.

28. Kottmann, J. P.; Martin, O. J.; Smith, D. R.; Schultz, S. Non-Regularly Shaped Plasmon Resonant Nanoparticle as Localized Light Source for near-Field Microscopy. *J. Microsc.* **2001,** *202* (Pt 1), 60-5.

29. Wang, P. H.; Salcedo, W. J.; Pichaandi, J.; van Veggel, F. C. J. M.; Brolo, A. G. Polarization-Dependent Extraordinary Optical Transmission from Upconversion Nanoparticles. *Nanoscale* **2015,** *7* (43), 18250-18258.

30. Wirth, J.; Garwe, F.; Meyer, R.; Csáki, A.; Stranik, O.; Fritzsche, W. Plasmonically Enhanced Electron Escape from Gold Nanoparticles and Their Polarization-Dependent Excitation Transfer Along DNA Nanowires. *Nano Lett.* **2014,** *14* (7), 3809-3816.

31. Sardar, R.; Shumaker-Parry, J. S. 9-Bbn Induced Synthesis of Nearly Monodisperse Ω-Functionalized Alkylthiol Stabilized Gold Nanoparticles. *Chem. Mater.* **2009,** *21* (7), 1167-1169.

32. Shem, P. M.; Sardar, R.; Shumaker-Parry, J. S. One-Step Synthesis of Phosphine-Stabilized Gold Nanoparticles Using the Mild Reducing Agent 9-Bbn. *Langmuir* **2009,** *25* (23), 13279-13283.

33. Brown, K. R.; Walter, D. G.; Natan, M. J. Seeding of Colloidal Au Nanoparticle Solutions. 2. Improved Control of Particle Size and Shape. *Chem. Mater.* **2000,** *12* (2), 306-313.

34. Sauthier, M. L.; Carroll, R. L.; Gorman, C. B.; Franzen, S. Nanoparticle Layers Assembled through DNA Hybridization: Characterization and Optimization. *Langmuir* **2002,** *18* (5), 1825-1830.

35. Cao, Y. C.; Jin, R.; Mirkin, C. A. Nanoparticles with Raman Spectroscopic Fingerprints for DNA and Rna Detection. *Science* **2002,** *297* (5586), 1536-1540.

36. Fahmi, A.; D'Aleo, A.; Williams, R. M.; De Cola, L.; Gindy, N.; Voegtle, F. Converting Self-Assembled Gold Nanoparticle/Dendrimer Nanodroplets into Horseshoe-Like Nanostructures by Thermal Annealing. *Langmuir* **2007,** *23* (14), 7831-7835.

37. Jana, N. R.; Gearheart, L.; Murphy, C. J. Wet Chemical Synthesis of High Aspect Ratio Cylindrical Gold Nanorods. *J. Phys. Chem B* **2001,** *105* (19), 4065-4067.

38. Frens, G. Controlled Nucleation for the Regulation of the Particle Size in Monodisperse Gold Suspensions. *Nature* **1973,** *241* (105), 20-22.

39. Wustholz, K. L.; Henry, A.-I.; McMahon, J. M.; Freeman, R. G.; Valley, N.; Piotti, M. E.; Natan, M. J.; Schatz, G. C.; Duyne, R. P. V. Structure− Activity Relationships in Gold Nanoparticle Dimers and Trimers for Surface-Enhanced Raman Spectroscopy. *J. Am. Chem. Soc.* **2010,** *132* (31), 10903-10910.

40. Huang, Y.-F.; Wu, D.-Y.; Zhu, H.-P.; Zhao, L.-B.; Liu, G.-K.; Ren, B.; Tian, Z.-Q. Surface-Enhanced Raman Spectroscopic Study of P-Aminothiophenol. *Phys. Chem. Chem. Phys.* **2012,** *14* (24), 8485-8497.

41. Xia, X.; Li, W.; Zhang, Y.; Xia, Y. Silica-Coated Dimers of Silver Nanospheres as Surface-Enhanced Raman Scattering Tags for Imaging Cancer Cells. *Interface Focus* **2013,** *3* (3).

42. Straney, P. J.; Marbella, L. E.; Andolina, C. M.; Nuhfer, N. T.; Millstone, J. E. Decoupling Mechanisms of Platinum Deposition on Colloidal Gold Nanoparticle Substrates. *J. Am. Chem. Soc.* **2014,** *136* (22), 7873-7876.

43. Minati, L.; Benetti, F.; Chiappini, A.; Speranza, G. One-Step Synthesis of Star-Shaped Gold Nanoparticles. *Colloids Surf., A* **2014,** *441* (0), 623-628.

44. Wang, Z.; Zhang, J.; Ekman, J. M.; Kenis, P. J. A.; Lu, Y. DNA-Mediated Control of Metal Nanoparticle Shape: One-Pot Synthesis and Cellular Uptake of Highly Stable and Functional Gold Nanoflowers. *Nano Lett.* **2010,** *10* (5), 1886-1891.

45. Hasan, S. A Review on Nanoparticles: Their Synthesis and Types. *Res. J. Rec. Sci. ISSN* **2015,** *2277*, 2502.

46. McMahon, J. M.; Wang, Y.; Sherry, L. J.; Van Duyne, R. P.; Marks, L. D.; Gray, S. K.; Schatz, G. C. Correlating the Structure, Optical Spectra, and Electrodynamics of Single Silver Nanocubes. *J. Phys. Chem. C* **2009,** *113* (7), 2731-2735.

47. Khoury, C. G.; Vo-Dinh, T. Gold Nanostars for Surface-Enhanced Raman

Scattering: Synthesis, Characterization and Optimization. *J. Phys. Chem. C* **2008,** *112* (48), 18849-18859.

48. Wojtysiak, S.; Solla-Gullón, J.; Dłużewski, P.; Kudelski, A. Synthesis of Core–Shell Silver–Platinum Nanoparticles, Improving Shell Integrity. *Colloids Surf., A* **2014,** *441* (0), 178-183.

49. Ming, L.; Scott, K. C.; Jianming, Z.; Jessica, L.; Zoraida, P. A.; Dongling, M.; Nianqiang, W. Shape-Dependent Surface-Enhanced Raman Scattering in Gold–Raman-Probe–Silica Sandwiched Nanoparticles for Biocompatible Applications. *Nanotechnology* **2012,** *23* (11), 115501.

50. Ramsey, J. D.; Zhou, L.; Kyle Almlie, C.; Lange, J. D.; Burrows, S. M. Achieving Plasmon Reproducibility from Surfactant Free Gold Nanostar Synthesis. *New J. Chem.* **2015,** *39* (12), 9098-9108.

51. Hsiangkuo, Y.; Christopher, G. K.; Hanjun, H.; Christy, M. W.; Gerald, A. G.; Tuan, V.-D. Gold Nanostars: Surfactant-Free Synthesis, 3d Modelling, and Two-Photon Photoluminescence Imaging. *Nanotechnology* **2012,** *23* (7), 075102.

52. Haes, A. J.; Van Duyne, R. P. A Nanoscale Optical Biosensor: Sensitivity and Selectivity of an Approach Based on the Localized Surface Plasmon Resonance Spectroscopy of Triangular Silver Nanoparticles. *J. Am. Chem. Soc.* **2002,** *124* (35), 10596-10604.

53. Zheng, P.; Li, M.; Jurevic, R.; Cushing, S. K.; Liu, Y.; Wu, N. A Gold Nanohole Array Based Surface-Enhanced Raman Scattering Biosensor for Detection of Silver(I) and Mercury(Ii) in Human Saliva. *Nanoscale* **2015,** *7* (25), 11005-11012.

54. Amendola, V.; Meneghetti, M. What Controls the Composition and the Structure of Nanomaterials Generated by Laser Ablation in Liquid Solution? *PCCP* **2013,** *15* (9), 3027-3046.

55. Haynes, C. L.; Van Duyne, R. P. Nanosphere Lithography: A Versatile Nanofabrication Tool for Studies of Size-Dependent Nanoparticle Optics. *J. Phys. Chem. B* **2001,** *105* (24), 5599-5611.

56. Zheng, Y. B.; Juluri, B. K.; Kiraly, B.; Huang, T. J. Ordered Au Nanodisk and Nanohole Arrays: Fabrication and Applications. *J. Nanotech. Eng. Med.* **2010,** *1* (3), 031011-031011.

57. Shumaker-Parry, J. S.; Rochholz, H.; Kreiter, M. Fabrication of Crescent-Shaped Optical Antennas. *Adv. Mater.* **2005,** (17), 2131-2134.

58. Haynes, C. L.; Van Duyne, R. P. Nanosphere Lithography: A Versatile Nanofabrication Tool for Studies of Size-Dependent Nanoparticle Optics. *J. Phys. Chem. B* **2001,** *105* (24), 5599-5611.

59. Malinksy, M. D.; Kelly, K. L.; Schatz, G. C.; Van Duyne, R. P. Nanosphere Lithography: Effect of Substrate on the Localized Plasmon Resonance Spectrum of Silver Nanoparticles. *J. Phys. Chem. B* **2001,** *105*, 2343-2350.

60. Bukasov, R.; Shumaker-Parry, J. S. Highly-Tunable Infrared Extinction Properties of Gold Nanocrescents. *Nano Lett.* **2007,** *7*, 1113-1118.

61. Dieringer, J. A.; McFarland, A. D.; Shah, N. C.; Stuart, D. A.; Whitney, A. V.; Yonzon, C. R.; Young, M. A.; Zhang, X.; Van Duyne, R. P. Introductory Lecture Surface Enhanced Raman Spectroscopy: New Materials, Concepts, Characterization Tools, and Applications. *Faraday Discuss.* **2006,** *132* (0), 9-26.

62. Bukasov, R.; Ali, T. A.; Nordlander, P.; Shumaker-Parry, J. S. Probing the Plasmonic near-Field of Gold Nanocrescent Antennas. *ACS Nano* **2010,** *4* (11), 6639-6650.

63. Bukasov, R.; Shumaker-Parry, J. S. Siver Nanocrescents with Infrared Plasmonic Properties as Tunable Substrates for Surface Enhanced Infrared Absorption Spectrscopy. *Anal. Chem.* **2009,** *81* (4531-4535).

64. Cooper, C. T.; Rodriguez, M.; Blair, S.; Shumaker-Parry, J. S. Polarization Anisotropy of Multiple Localized Plasmon Resonance Modes in Noble Metal Nanocrescents. *J. Phys. Chem. C* **2014,** *118* (2), 1167–1173.

65. Cooper, C. T.; Rodriguez, M.; Blair, S.; Shumaker-Parry, J. S. Mid-Infrared Localized Plasmons through Structural Control of Gold and Silver Nanocrescents. *J. Phys. Chem. C* **2015,** *119* (21), 11826–11832.

66. Sung, J.; Kosuda, K. M.; Zhao, J.; Elam, J. W.; Spears, K. G.; Van Duyne, R. P. Stability of Silver Nanoparticles Fabricated by Nanosphere Lithography and Atomic Layer Deposition to Femtosecond Laser Excitation. *J. Phys. Chem. C* **2008,** *112* (15), 5707-5714.

67. Hook, D. A.; Olhausen, J. A.; Krim, J.; Dugger, M. T. Evaluation of Oxygen Plasma and Uv Ozone Methods for Cleaning of Occluded Areas in Mems Devices. *J. of Microelectromech. S.* **2010,** *19* (6), 1292-1298.

68. Gaines Jr, G. L. On the Water Wettability of Gold. *J. Colloid Interface Sci.* **1981,** *79* (1), 295.

69. Smith, T. The Hydrophilic Nature of a Clean Gold Surface. *J. Colloid Interface Sci.* **1980,** *75* (1), 51-55.

70. Brongersma, M. L.; Halas, N. J.; Nordlander, P. Plasmon-Induced Hot Carrier Science and Technology. *Nat Nano* **2015,** *10* (1), 25-34.

71. Wu, K.; Chen, J.; McBride, J. R.; Lian, T. Efficient Hot-Electron Transfer by a Plasmon-Induced Interfacial Charge-Transfer Transition. *Science* **2015,** *349*

(6248), 632.

72. Dillon, A. C.; Ott, A. W.; Way, J. D.; George, S. M. Surface Chemistry of Al2o3 Deposition Using Al(Ch3)3 and H2o in a Binary Reaction Sequence. *Surf. Sci.* **1995,** *322* (1–3), 230-242.

73. Puurunen, R. L. Surface Chemistry of Atomic Layer Deposition: A Case Study for the Trimethylaluminum/Water Process. *J. Appl. Phys.* **2005,** *97* (12), 121301-1-52.

74. George, S. M. Atomic Layer Deposition: An Overview. *Chem. Rev.* **2010,** *110* (1), 111-131.

75. Devloo-Casier, K.; Ludwig, K. F.; Detavernier, C.; Dendooven, J. In Situ Synchrotron Based X-Ray Techniques as Monitoring Tools for Atomic Layer Deposition. *J. Vac. Sci. Technol. A* **2014,** *32* (1), 14.

76. Kobayashi, N. P.; Donley, C. L.; Wang, S.-Y.; Williams, R. S. Atomic Layer Deposition of Aluminum Oxide on Hydrophobic and Hydrophilic Surfaces. *J. Cryst. Growth* **2007,** *299* (1), 218-222.

77. Groner, M. D.; Fabreguette, F. H.; Elam, J. W.; George, S. M. Low-Temperature Al2o3 Atomic Layer Deposition. *Chem. Mater.* **2004,** *16* (4), 639-645.

78. Walker, M.; Nordquist, C.; Czaplewski, D.; Patrizi, G.; McGruer, N.; Krim, J. Impact of in Situ Oxygen Plasma Cleaning on the Resistance of Ru and Au-Ru Based Rf Microelectromechanical System Contacts in Vacuum. *J. Appl. Phys.* **2010,** *107* (8), 084509.

79. Berman, D.; Krim, J. Impact of Oxygen and Argon Plasma Exposure on the Roughness of Gold Film Surfaces. *Thin Solid Films* **2012,** *520* (19), 6201-6206.

80. Zhang, Y.; Bertrand, J. A.; Yang, R.; George, S. M.; Lee, Y. C. Electroplating to Visualize Defects in Al2o3 Thin Films Grown Using Atomic Layer Deposition. *Thin Solid Films* **2009,** *517* (11), 3269-3272.

81. Klumbies, H.; Karl, M.; Hermenau, M.; Rösch, R.; Seeland, M.; Hoppe, H.; Müller-Meskamp, L.; Leo, K. Water Ingress into and Climate Dependent Lifetime of Organic Photovoltaic Cells Investigated by Calcium Corrosion Tests. *Sol. Energy Mater. Sol. Cells* **2014,** *120*, 685-690.

82. Klumbies, H.; Müller-Meskamp, L.; Mönch, T.; Schubert, S.; Leo, K. The Influence of Laterally Inhomogeneous Corrosion on Electrical and Optical Calcium Moisture Barrier Characterization. *Rev. Sci. Intstrum.* **2013,** *84* (2), 024103.

83. Klumbies, H.; Schmidt, P.; Hähnel, M.; Singh, A.; Schroeder, U.; Richter, C.; Mikolajick, T.; Hoßbach, C.; Albert, M.; Bartha, J. W.; Leo, K.; Müller-

Meskamp, L. Thickness Dependent Barrier Performance of Permeation Barriers Made from Atomic Layer Deposited Alumina for Organic Devices. *Org. Electron.* **2015,** *17*, 138-143.

84. Lin, Y.-S. A Surface Analysis on Oxygen Plasma-Cleaned Gold Pattern-Plated Substrates for Wire Bondability. *Surf. Coat. Technol.* **2003,** *173* (1), 47-57.

85. King, D. E. Oxidation of Gold by Ultraviolet Light and Ozone at 25 °C. *J. Vac. Sci. Technol. A* **1995,** *13* (3), 6.

86. Pétigny, S.; Mostéfa-Sba, H.; Domenichini, B.; Lesniewska, E.; Steinbrunn, A.; Bourgeois, S. Superficial Defects Induced by Argon and Oxygen Bombardments on (110) Tio2 Surfaces. *Surf. Sci.* **1998,** *410* (2–3), 250-257.

87. Hohertz, D.; Romanuik, S. F.; Gray, B. L.; Kavanagh, K. L. Recycling Gold Nanohole Arrays. *J. Vac. Sci. Technol. A* **2014,** *32* (3), 031403.

88. Winkler, K.; Wojciechowski, T.; Liszewska, M.; Gorecka, E.; Fialkowski, M. Morphological Changes of Gold Nanoparticles Due to Adsorption onto Silicon Substrate and Oxygen Plasma Treatment. *RSC Adv.* **2014,** *4* (25), 12729-12736.

CHAPTER 2

SURFACE PREPARATION OF GOLD NANOSTRUCTURES ON GLASS BY ULTRAVIOLET OZONE AND OXYGEN PLASMA FOR THERMAL ATOMIC LAYER DEPOSITION OF AL_2O_3

2.1 Prelude

Published and reprinted with permission from Lancaster, C. A.; Shumaker-Parry, J. S. Surface preparation of gold nanostructures on glass by ultraviolet ozone and oxygen plasma for thermal atomic layer deposition of Al_2O_3. *Thin Solid Films* **2016**, *612*, 141-146.

2.2 Abstract

Thin film deposition to create robust plasmonic nanomaterials is a growing area of research. Plasmonic nanomaterials have tunable optical properties and can be used as substrates for surface-enhanced spectroscopies. Due to the surface sensitivity and the dependence of the near-field behavior on structural details, degradation from cleaning or spectroscopic interrogation causes plasmonic nanostructures to lose distinctive localized surface plasmon resonances or exhibit diminished optical near-field enhancements over time. To decrease degradation, conformal thin films of alumina are deposited on

nanostructured substrates using atomic layer deposition. While film growth on homogenous surfaces has been studied extensively, atomic layer deposition-based film growth on heterogeneous nanostructured surfaces is not well characterized. In this report, we have evaluated the impact of oxygen plasma and ultraviolet ozone pre-treatments on Au nanoparticle substrates for thin film growth by monitoring changes in plasmonic response and nanostructure morphology. We have found that ultraviolet ozone is more effective than oxygen plasma for cleaning gold nanostructured surfaces, which is in contrast to bulk films of the same material. Our results show that oxygen plasma treatment negatively impacts the nanostructure and alumina coating based on both SEM analysis of morphology and changes in the plasmonic response.

2.3 Introduction

At the nanoscale, materials exhibit different electrical, conductive, optical, and mechanical properties. One example of a nanoscale optical phenomenon is the localized surface plasmon resonance (LSPR) response of metal nanoparticles. In the presence of electromagnetic (EM) waves, coherent oscillations of electrons in metal nanoparticles lead to wavelength selective absorption and scattering of light as well as locally enhanced EM fields around the particles.[1] The LSPR response is highly dependent on the structural properties and dielectric environment of the nanoparticles and this behavior has formed the basis for using metal nanoparticles in sensing and spectroscopy applications.[2-6] Due to the strong dependence on structural characteristics, plasmonic nanoparticles can lose distinctive LSPR responses and EM fields enhancements may diminish over time due to structural degradation from functionalization or cleaning

procedures. In addition, exposure of the metal nanostructures to high-energy femtosecond lasers also often leads to deformation or melting of metal nanostructures, especially when plasmons are induced leading to focusing of the incident intensity due to plasmonic antenna effects.[7] Degradation of the surface of nanoparticles limits shelf life (i.e. storage under N_2, etc.), especially due to oxidation processes of materials such as silver and adsorption of molecules from the surrounding environment leading to changes in surface properties over very short time periods. In order to inhibit or avoid surface degradation and structural damage, incorporation of ultra-thin protective coatings to cover complex, high aspect ratio structures over large surface areas has been investigated.[7-9]

One approach to introduce a thin protective coating is atomic layer deposition (ALD) of alumina (Al_2O_3). In ALD of alumina, a sub-nanometer conformal thin film is deposited by self-terminating reactions of trimethylaluminum (TMA) and water via a well-understood mechanism. [10-13] ALD-based film deposition is an especially good approach for protecting plasmonic nanostructures because the near field enhancements decay rapidly, on the order of a few nanometers to tens of nanometers from the surface. The physical robustness of Al_2O_3 protected metal nanostructures has been documented for femtosecond laser excitation[7] and for thermal cleaning treatments up to 400 °C.[9] These studies have shown that Al_2O_3 protected structures retain morphology and plasmonic properties under harsh experimental and cleaning conditions. While these alumina ALD studies are done on nanostructured surfaces, there is yet no research into the quality of the alumina film covering the nanostructures, unlike in Al_2O_3 film coverage of continuous metal films on substrates which has been studied more extensively.[14, 15]

On most continuous metal surfaces, an Al_2O_3 film forms via island growth, nucleating at a few defect sites from which the islands grow together after several deposition cycles to eventually form a film.[10] This type of growth can lead to pinhole defects and irregular surfaces and is especially problematic for fabricated gold nanoparticles. After a few minutes of exposure to air, gold becomes hydrophobic due to surface adsorption of species in the environment, which can negatively impact alumina deposition.[16, 17] One approach to establish defect-free alumina films is through control of the TMA nucleation by increasing the hydrophilicity of the gold substrate using surface cleaning techniques. However, surface modification is more challenging for a heterogeneous surface such as metal nanostructures supported on a substrate because of the presence of different materials (i.e., the nanostructures and the underlying substrate). With increasing interest in thin film deposition on heterogeneous nanostructured surfaces, it is important to take into account the unique properties the nanoscale regime offers. Modification of the metal nanoparticle structure leads to changes in the LSPR response, which ultimately impacts any application based on tailoring the optical properties through control of structural features. Sub-nanometer controlled deposition of a reproducible, defect-free ultrathin film is necessary, especially when the desired application depends on accessing the exponentially decaying EM near-field. Ideally, the surface preparation needs to leave the underlying nanostructure undamaged while also yielding a defect free, ultra-thin film.

Two surface preparation techniques, oxygen plasma and ultraviolet-ozone (UVO), are used extensively in fabrication to remove hydrocarbon contaminants from bulk Au and Si surfaces and from nanostructured surfaces.[14, 18-23] Both techniques generate

hydrophilic surfaces, which is ideal for Al_2O_3 deposition. However, the comparative impact of these techniques on nanostructured surfaces with different materials exposed (e.g., gold and SiO_2) has yet to be examined to the same extent as has been observed for uniform Au films or silicon surfaces. Recently, reports have indicated that oxygen plasma can be destructive to Au nanoparticles (AuNPs) [24, 25] but others have argued that the plasma does not alter the AuNP surface or damage only happens under very aggressive conditions.[21] In the case of UVO cleaning of surfaces, early studies were conducted for continuous planar metal films, but the assessment of the impact of UVO cleaning has not been extended to nanostructured surfaces.

In this report, fabricated plasmonic Au nanodisks (AuNDs) on glass were used as the model heterogeneous nanostructured substrate to investigate the effects of oxygen plasma compared to UVO treatment as a surface preparation process for Al_2O_3 thin film deposition. Due to the surface sensitivity of the LSPR response of AuNDs, any changes of the structure (shape changes, etching effects, etc.) as well as the local environment of the structure (the alumina film), can be monitored with UV/vis spectroscopy. Our studies demonstrate that when oxygen plasma cleaning procedures used for bulk metal films and glass or silicon substrates are applied to nanostructures, the process significantly alters the surface of gold nanostructures, as observed by changes in the LSPR response based on transmission UV-vis spectroscopy measurements and structure morphology from scanning electron microscopy analysis. Subsequently, damaging of the nanostructures impacts the nucleation of the Al_2O_3 film and nanostructure stability.

2.4 Experimental Details

2.4.1 *Fabrication*

Nanosphere template lithography coupled with ion beam milling was used to fabricate gold nanodisks (AuNDs) and has been described elsewhere. [26-28] Briefly, using an electron-beam evaporator (Denton SJ20C Vacuum USA, Moorestown, NJ), a 35 nm gold film as measured by a quartz crystal microbalance (XPC2 Inficon, East Syracuse, NY) was deposited (1 Å/s; normal to the substrate surface) under high vacuum (1.3×10^{-7} Pa or 1.0×10^{-6} Torr) onto 1 in. x 1 in. glass slides. A 0.01 % w/v solution of 220 ± 17.6 nm polystyrene beads (Polysciences, Inc.) was spin cast (900 rpm, 35 sec) on the Au films. An argon ion milling system (PlasmaLab 80 Plus, Oxford Instruments) was used to remove the Au film at a power of 100 W and flow rate of 10 sccm. The polystyrene spheres serve as templates by shielding portions of the Au from the ion beam milling, producing nanodisks. The polystyrene beads were then removed by lift-off using transparent tape, and the samples were stored under nitrogen.

2.4.2 *Atomic Layer Deposition*

A Cambridge NanoTech Fiji F200 Plasma (Cambridge, MA) ALD reactor was used to grow an Al_2O_3 film on the AuNDs and glass substrate. TMA and water were pulsed alternately in a nitrogen carrier stream using a growth temperature of 33 °C and base pressure of 213 Pa (1.6 mTorr). The process occurred in four steps: (1) 0.06 sec pulse of water, (2) 60 second purge with nitrogen, (3) 0.06 second pulse of TMA, (4) 10 second purge with nitrogen.

2.4.3 *Cleaning Treatments*

AuNDs and alumina-coated AuNDs (Al_2O_3-AuNDs) were exposed for 10 minutes with either UVO (Jelight 342, Irvine CA) or oxygen plasma (PlasmaLab 80 Plus, Oxford Instruments) at 10 sccm, 75 W and a base pressure of 25 mTorr. The commercial UVO system produces 28 mW/cm^2 at 5 mm (operating distance from lamp) at ambient pressure. An exhaust assembly with blower attachment was used to maintain a positive flow of media through the system.

2.4.4 *Characterization*

The optical properties of the AuNDs were characterized by transmission UV-vis spectroscopy. Extinction spectra were collected with a Perkin-Elmer Lambda 750 UV/vis spectrophotometer with 100 % angular controlled s-polarized light. The λ_{max} was determined using Spectrum software and the center of gravity function with all unaltered, as-fabricated disk samples. Scanning electron microscopy (SEM) (FEI NovaNano 630 equipped with a Helix detector) was used to analyze film deposition and structural changes of bare and alumina coated AuNDs.

2.4.5 *Contact Angle Measurements*

Images of 10 μL drops of Nanopure deionized water were collected with a c525 Logitech webcam. Contact angle measurements were made with the ImageJ Contact Angle package.

2.5 Results and Discussion

We investigated the utilization of UV ozone (UVO) and oxygen plasma for surface preparation of a heterogeneous nanostructured surface comprised of gold nanodisks (AuNDs) supported on glass for ALD-based alumina film growth. Oxygen plasma for cleaning is generated by converting oxygen gas into monatomic oxygen and oxygen ions and radicals by radiofrequencies at low pressure. The ions and radicals react with hydrocarbons, either C-C or C-H bonds, to form H_2O, CO, and CO_2 which are then pumped out of the system. The high kinetic energy of the ions can lead to sputter-etching of surfaces when they collide, but this is typically considered a more minor secondary process. For UVO cleaning, atmospheric air is exposed to UV light to form reactive species. Molecular oxygen dissociates into oxygen anions at 184.9 nm and these anions can then form ozone by reacting with O_2. Ozone absorbs radiation at 253.7 nm and forms $3[O]^-$. These ions react with hydrocarbons and generate volatile molecules that subsequently desorb from the surface.

We studied the impact of UVO and oxygen plasma cleaning on the nanostructures and ALD film growth by electron microscopy analysis of the AuNDs and by monitoring the plasmonic response of the AuNDs. Two sets of AuNDs were cleaned with either UVO or oxygen plasma and these were compared to a control set that was left untreated prior to each of two Al_2O_3 depositions. The optical properties of the three sets (n=9 samples per set) of 35-nm-thick AuNDs were collected by extinction spectroscopy at three different time points: after fabrication (λ_{max}), after the initial cleaning and Al_2O_3 deposition (λ_{ALD1}), and after the second cleaning and Al_2O_3 deposition (λ_{ALD2}). Each Al_2O_3 deposition was prefaced with the designated cleaning treatment. The time between

the fabrication of the AuNDs and the initial cleaning and deposition was 24 h. The initial Al_2O_3 deposition was 200 AB cycles, which ideally would deposit an 18 nm-thick Al_2O_3 film. After optical analysis with UV/vis spectroscopy, all samples were kept in sealed storage jars for one month to model shelf storage. After the one month storage, samples were cleaned as described (untreated, oxygen plasma, or UVO) and a second Al_2O_3 deposition of 50 AB cycles was performed which would ideally deposit a 4.5 nm-thick Al_2O_3 film. This second deposition evaluates the effectiveness of the cleaning techniques to prepare an aged Al_2O_3-coated Au nanostructured surface for an additional film deposition via ALD.

2.5.1 *Hydrophobicity of Treated Films*

While the hydrophobicity of UVO and oxygen plasma treatments has been studied, we qualitatively evaluated Au films and nanostructured substrates to compare with the trends reported in literature based on the cleaning techniques used here[17]. An evaporated Au film was stored in a sealed jar for 24 h. After this time period, the film had a contact angle of 94°; after treatment with UVO (10 min.) the surface was completed wetted by a 10 μL drop of deionized water. A separate film that was fabricated at the same time, under the same conditions, was treated with an oxygen plasma (10 min.) and had a water contact angle of 10°, suggesting a slightly more hydrophobic surface than the surface treated with UVO. It is important to note that the contact angle measurement was carried out 4 h after oxygen plasma treatment.

AuND samples stored for 24 h had water contact angles of 49°, showing that the nanostructured surface became more hydrophobic during that time, though not as

significantly as the Au films. After UVO treatment, the AuNDs supported on glass were completely wetted by 10 μL drop of deionized water. After oxygen plasma exposure (4 hour delay between exposure and measurement) the contact angle was 17°. The oxygen plasma treatment on the heterogeneous AuNDs was less effective than the oxygen plasma treatment on the Au film as evidenced by the larger contact angle. This difference highlights the fact that these cleaning treatments do not necessarily lead to the same outcomes for bulk films and heterogeneous surfaces and the different physical properties of these surfaces need to be accounted for when fabricating thin films over nanostructured substrates.

2.5.2 *LSPR Characterization of Nanostructure Changes*

The LSPR response of the AuNDs depends on the local materials (Au nanostructures and Al_2O_3) and the response is used to gain an understanding of surface changes by monitoring shifts in the LSPR peak using UV/vis spectroscopy (Figure 2.1). Angstrom scale depositions of alumina can be detected by monitoring changes in the λ_{max} due to the sensitivity of the LSPR to the addition of the material on the surface of the nanostructures [29, 30]. Specifically, AuNDs are sensitive to a change in refractive index (RI). As alumina (RI = 1.63) is deposited, there is a red shift in the λ_{max} and if alumina is removed from the AuND surface, there is a blue-shift in the LSPR response. LSPR can also be used to probe changes to the underlying nanoparticle structure because the LSPR is highly dependent on metal nanostructure shape parameters (diameter, height, shape). If the structure is made smaller by etching, the LSPR response blue shifts; as a general rule, smaller particles are blue shifted with respect to larger particles of the same geometry.

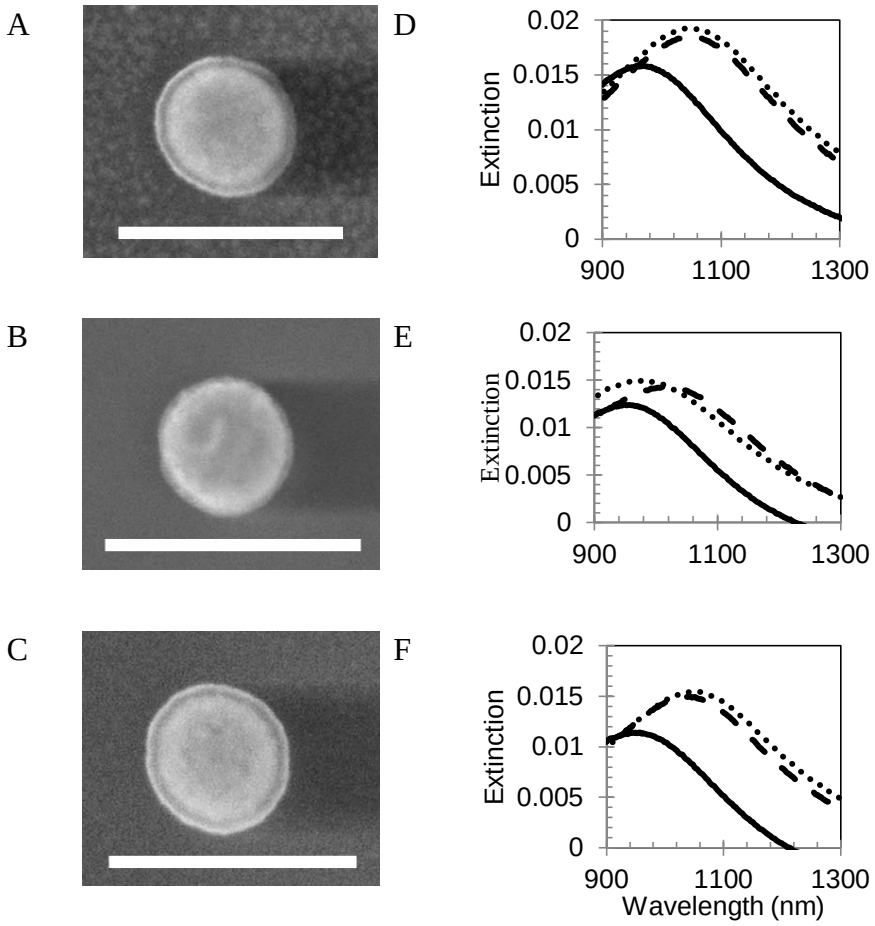

Figure 2.1 LEFT: SEM of AuNDs on SiO_2 after 250 AB cycles to create a an Al_2O_3 film; (A) untreated sample with no cleaning process before Al_2O_3 deposition; (B) oxygen plasma treated before Al_2O_3 deposition; (C) UVO treated before Al_2O_3 deposition. Scale bar is 500 nm. RIGHT: Spectra of AuNDs immediately after fabrication (solid line), after 200 AB cycles of Al_2O_3 deposition (dashed line), and after an additional 50 AB cycles of Al_2O_3 (dotted line); (D) untreated sample with no cleaning process before Al_2O_3 depositions; (E) oxygen plasma treated before each Al_2O_3 deposition; (F) UVO treated before each Al_2O_3 deposition.

Therefore, LSPR response of the AuNDs is used to probe film formation with high sensitivity as well as nanostructure fidelity. The initial λ_{max} of the unaltered AuNDs ranged from 952-980 nm. Figure 2.1 shows SEM images of the final Al_2O_3-AuNDs and spectra of representative samples immediately after fabrication (solid line), after 200 AB cycles of Al_2O_3 deposition (dashed line), and after 50 AB cycles of Al_2O_3 addition (dotted line). The average LSPR peak shift for the first 200 AB depositions is summarized in Table 2.1 as $\Delta\lambda_{ALD1\text{-}max}$ and the peak shift after the second alumina deposition of 50 AB cycles is summarized as $\Delta\lambda_{ALD2\text{-}ALD1.}$

The freshly prepared AuNDs supported formation of an alumina film. The untreated AuNDs (spectra Figure 2.1D) exhibited an average $\Delta\lambda_{ALD1\text{-}max}$ of 80.8 ± 2.4 nm for the first Al_2O_3 film deposition (Table 2.1). After the AuNDs were stored for 1 month, we attempted to form a second alumina film. After 50 AB cycles of Al_2O_3 deposition, the untreated AuNDs had an average LSPR shift of $\Delta\lambda_{ALD2\text{-}ALD1}$ of 0.3 ± 3.3 nm (n=8 samples). This suggests that the Al_2O_3 surface of the untreated samples did not maintain a clean surface capable of ideal Al_2O_3 nucleation and growth after 1 month of storage.

Oxygen plasma treated AuNDs (Figure 2.1E) had a $\Delta\lambda_{ALD1\text{-}max}$ of 59.2 ± 4.1 nm. The red shift indicates that material was deposited on the AuNDs, but less than the

Table 2.1 LSPR λ_{max} shift of all AuNDs (n = 9) after cleaning treatment and Al_2O_3 deposition, with the exception of the untreated $\Delta\lambda_{ALD2\text{-}ALD1}$ where n = 8.

	$\Delta\lambda_{ALD1-max}$ (nm)			$\Delta\lambda_{ALD2\text{-}ALD1}$ (nm)			$\Delta\lambda_{Total}$ (nm)		
Cleaning Procedure	$\bar{\lambda}$	±	σ	$\bar{\lambda}$	±	σ	$\bar{\lambda}$	±	σ
Untreated	80.8	±	2.4	0.3	±	3.3	77.5	±	12.1
Oxygen plasma	60	±	4.1	-48.6	±	8.6	10.6	±	11.9
UVO	82.0	±	2.3	11.2	±	0.7	93.2	±	2.4

untreated or UVO treated AuNDs. After one month of storage, a second cleaning process and 50 AB cycles of alumina deposition, the LSPR response blue-shifted with a $\Delta\lambda_{ALD2\text{-}ALD1}$ of -48.6 ± 8.6 nm. Based on the blue shifted LSPR response, we suspected that the Al_2O_3 surface of the oxygen treated samples did not support Al_2O_3 nucleation and Au or Al_2O_3 was likely removed during exposure to the oxygen plasma. The reason for this conclusion will be discussed in more detail below.

UVO treated AuNDs (Figure 2.1F) had a $\Delta\lambda_{ALD1\text{-}max}$ of 82.0 ± 2.3 nm after the first cleaning treatment and alumina film growth. After the one month of storage, a second cleaning treatment and 50 AB cycles of Al_2O_3 deposition, the UVO treated AuNDs exhibited a $\Delta\lambda_{ALD2\text{-}ALD1}$ of 11.2 ± 1 nm. Thus, the UVO treatment of the AuNDs led to alumina film formation after both cleaning treatments, even after storage of Al_2O_3-coated AuNDs. Compared to the untreated and oxygen-plasma cleaned AuNDs, the UVO treatment led to consistent Al_2O_3 film nucleation and consistent, reproducible growth.

The untreated laboratory stored AuNDs and the UVO cleaned AuNDs exhibited similar LSPR responses, 80.8 and 82.0 nm red shifts, respectively, after the addition of Al_2O_3 in the first deposition. The similar response for untreated (Figure 2.1A and D) and UVO treated (Figure 2.1C and F) AuNDs suggests that the difference in surface reactivity for Al_2O_3 nucleation between “fresh” AuNDs (untreated) and UVO treated AuNDs is minimal. The 60 nm LSPR shift of the AuNDs after the first oxygen plasma treatment and alumina film growth indicates that (Figure 2.1B and E) the nucleation and film growth was inhibited relative to the untreated and UVO treated AuNDs. Significantly, the aged Al_2O_3-AuNDs could only support additional Al_2O_3 film growth when treated with UVO without damaging the underlying structure. Similar to the loss of hydrophilicity that

a metal or Si film or structured surface would experience upon introduction to the atmosphere and consequential buildup up hydrocarbons and debris, the hydrophilic alumina surface becomes hydrophobic over time.[14, 18, 19, 25, 31, 32] Once the surface is hydrophobic to some extent, the deposition of alumina is impeded and is increasingly island-like and less conformal.[33] By cleaning the aged Al_2O_3-AuNDs with UVO, the debris is removed and the –OH terminated or hydrophilic properties of the Al_2O_3 film are renewed or "re-activated.

We undertook an additional study to determine the cause of the smaller initial LSPR red shift (60 nm) of the oxygen plasma treated AuNDs after the initial alumina deposition and the blue shift (-48.6 ± 8.6 nm) of the oxygen plasma treated Al_2O_3-AuNDs following the second alumina deposition. After fabrication and LSPR characterization (i.e. determination of the LSPR λ_{max}), AuNDs were treated with UVO or oxygen plasma and the LSPR peak position ($\lambda_{cleaned}$) was determined with UV/visible spectroscopy without an additional alumina deposition. In order to have the most freshly cleaned AuNDs for alumina deposition for the study described above, we did not characterize the LSPR response of those AuNDs immediately after cleaning, before alumina deposition. Table 2.2 presents a summary of the results. In this study,

Table 2.2 LSPR shift ($\Delta\lambda_{cleaned}.\lambda_{max}$) of all AuNDs (n = 9) and Al_2O_3-AuNDs (n = 9) after specified cleaning treatment.

	AuND $\Delta\lambda_{cleaned - max}$ (nm)			Al_2O_3-AuND $\Delta\lambda_{cleaned - max}$ (nm)		
Cleaning Procedure	$\bar{\lambda}$	±	σ	$\bar{\lambda}$	±	σ
Untreated	-6.1	±	3.7	2.3		
Oxygen plasma	-20.8	±	5.6	-48.2	±	7.1
UVO	1.3	±	2.1	6.3	±	6.1

measurement of the LSPR response ($\lambda_{cleaned}$) after cleaning, but before the addition of alumina, probes the effect of the cleaning treatment on the Au nanostructures. The oxygen treated AuNDs had a blue-shifted $\Delta\lambda_{cleaned.\ -\ max}$ of -20.8 ± 5.6 nm and the UVO treated AuNDs exhibited a red-shifted $\Delta\lambda_{cleaned.\ -\ max}$ of 1.3 ± 2.1 nm after the cleaning procedure. The blue shift of the LSPR response after the cleaning treatment provides evidence that the oxygen plasma etches the AuNDs. This 20 nm blue shift corresponds well to the difference between the LSPR responses measured for oxygen plasma and UVO treated AuNDs discussed above ($\Delta\lambda_{ALD1\text{-}max,}$ 59.2 ± 4.1 nm and 82.0 ± 2.3 nm, respectively). It may be that Au is removed from the surface by a secondary sputtering process during the oxygen plasma exposure, but Al_2O_3 nucleates and forms a film to the same extent as is formed on the UVO treated samples. The combination of these two processes would lead to a smaller $\Delta\lambda_{max}$ compared to AuNDs that have not been etched before alumina film growth. However, this does not explain the origin of the substantial blue shifted $\Delta\lambda_{ALD2\text{-}ALD1}$ of -48.6 ± 8.6 nm for the oxygen treated Al_2O_3-AuNDs that was observed after the second alumina deposition.

In order to probe if the oxygen plasma treatment was also etching the alumina film, we fabricated Al_2O_3-coated AuNDs and monitored the LSPR response after exposure to oxygen plasma. An alumina film was formed on AuNDs using a 50 AB cycle ALD process (~5 nm Al_2O_3) immediately after an initial oxygen plasma treatment to insure the cleanest AuNDs for Al_2O_3 deposition. After the initial LSPR (λ_{max}) of the Al_2O_3-AuNDs was determined with UV/visible spectroscopy, two sets (n=9 per set) of AuNDs were treated with either UVO or oxygen plasma and the $\lambda_{cleaned}$ was determined. The oxygen plasma treated Al_2O_3-AuNDs exhibited a LSPR shift of -48.2 ± 7.1 nm and

the UVO treated Al_2O_3-AuNDs had a LSPR shift of 6.3 ± 6.1 nm (see Table 2.2). The large blue shift for the oxygen plasma treated AuNDs indicates that both Al_2O_3 as well as possibly Au are etched during treatment. The size of the observed blue shift (-48 nm) agrees well with the shift observed in the AuND cleaning experiments discussed above. The total blue shifting of the LSPR response of -20 nm after oxygen treatment of uncoated AuNDs and -48 nm after treatment of alumina-coated AuNDs accounts for the approximately 70 nm difference between UVO and oxygen plasma treated AuNDs in the cleaning experiments (see Table 2.1) after the two treatment/ALD deposition processes.

2.5.3 *SEM Characterization of Film Formation*

The observations of the LSPR response as related to both etching and alumina deposition are supported by the SEM images shown in Figure 2.1. The individual nanodisk in each image shown is representative of the entire sample set and the high uniformity of nanodisk structures is well known.[27, 34] The diameter of UVO treated Al_2O_3-AuND (n=50 AuNDs) averaged 309 ± 15 nm, untreated (n=56 AuNDs) averaged 307 ± 14 nm, and oxygen treated (n=36 AuNDs) averaged 255 ± 18 nm. These size differences are consistent with the LSPR shifts and the standard deviations are within that of the native polystyrene template (see section 2.1). The UVO treated AuNDs supported alumina film growth during both deposition cycles ($\Delta\lambda_{total}$ of 93.2 ± 2.4 nm) and had the largest diameter. The oxygen treated AuNDs had the smallest $\Delta\lambda_{total}$ of 10.6 ± 11.9 nm and also the smallest diameter of the final Al_2O_3-AuNDs. A qualitative inspection of the SEM images shows that UVO and untreated Al_2O_3-AuNDs (Figure 2.1A and C, respectively) have similar, uniform Al_2O_3 film growth. The AuNDs are

clearly seen beneath the Al_2O_3 film, which has a smooth and sharply contrasted edge as shown by the outer ring in the SEM images. In comparison, the oxygen plasma treated Al_2O_3-AuND (Figure 2.1B) does have a coating of Al_2O_3, but the film forms a less uniform layer around the AuND. The film appears to have an almost serrated-edge outer ring that lacks the sharp contrast of the other alumina-coated AuNDs; this suggests incomplete nucleation and film growth or a roughened AuND. While literature reports that oxygen plasma does not damage gold surfaces, the oxygen plasma pretreated Al_2O_3-AuND shows signs of deterioration of the underlying AuND which is consistent with a blue-shifted LSPR response (as discussed in section 3.2). [14]

The serrated-edge structures shown in the SEM images and the size discrepancy between UVO and oxygen plasma treated samples qualitatively show that the oxygen plasma samples had less Al_2O_3 growth and the underlying AuND was etched, creating a smaller nanostructure with more surface roughness. Damage to the nanostructures highlights the importance of investigating nanostructure properties and stability compared to bulk films of the same material under the same surface preparation conditions.

There is extensive research showing that oxygen plasma and UVO both have utility in removing hydrocarbons from Au films and silicon substrates. Berman and Krim showed that oxygen plasma can be used in radio-frequency microelectromechanical system (RF-MEMS) applications to clean gold films without increasing surface roughness.[14] In a direct comparison of UVO and oxygen plasma, a monolayer of tridecafluorotris(dimethylamino)silane or FOTAS, was chemically bonded to a MEMS device and then treated with either UVO or oxygen plasma.[18] Using Time-of-Flight

secondary ion mass spectrometry (ToF-SIMS), it was determined that oxygen plasma was a more effective cleaning method for occluded areas of silicon surfaces.[18] However, the vast majority of studies comparing UVO and oxygen plasma treatments were based on investigations using bulk films. The study that is most relevant for substrates supporting micro- and nano-structures is presented by Raiber et al. The authors discuss the use of self-assembled monolayers (SAMs) as a resist in lithographic techniques to produce micrometer-sized Au-structured films. The fabrication method uses an oxygen plasma to remove the SAMs in a post-etching process. The authors did not report damage to the resulting microstructures. However, this may be because the Au films used in the fabrication were quite thick (40-200 nm) and were large in terms of their lateral dimensions (i.e., well beyond nanoscale or even microscale features). Our study indicates that the sensitivity of nanoscale structures to morphology necessitates consideration of whether or not a surface treatment process used for bulk films can be transferred without consequences to heterogeneous nanostructured surfaces, even processes as simple as surface cleaning and preparation.

Our studies also provide evidence that surface treatments can impact robust alumina coatings. We observed that oxygen plasma treatment of alumina-coated AuNDs resulted in blue-shifted LSPR responses (section 3.2) and produced nanostructures with roughened edges (Figure 2.1B), indicating the alumina coating was etched to some extent. In contrast, UVO treated AuNDs had consistent Al_2O_3 growth and UVO treatment re-activated old Al_2O_3-AuND after short-term storage (one month) without damaging the structures.

2.6 Conclusions

We have observed that oxygen plasma exposure, though a successful cleaning method for bulk Au films and silicon surfaces, has detrimental effects on heterogeneous surfaces composed of Au nanostructures supported on glass. For bare AuNDs and Al_2O_3-AuNDs on glass substrates, oxygen plasma etches both the Au and the Al_2O_3. We have also shown that an Al_2O_3-coated device can have a long shelf with the use of a simple cleaning technique, making the development of these devices practical. UVO treatment of AuNDs prior to Al_2O_3 deposition generates uniform growth and re-activates aged and "dirty" Au and Al_2O_3 surfaces. This adds to early work by King, which demonstrated that UVO treatments result in a rapid loss of surface bound hydrocarbons and oxycarbons.[16] By treating the AuNDs with UVO, the surface reactivity is more homogeneous, which leads to uniform nucleation. This is an important finding as defect-free films are a key component of nanostructure protection and fabrication optimization.

In summary, there have been conflicting reports on the impact of oxygen plasma on nanoparticles, but our findings support other observations that oxygen plasma treatments are detrimental to nanoparticles.[24, 25] Moreover, we propose the use of UVO to clean heterogeneous Au nanoparticle surfaces with the additional benefit of being a superior technique for preparation of thin film deposition when a hydrophilic surface is required, as in the case of atomic layer deposition of alumina.

Funding Sources: National Science Foundation (NSF) Integrative Graduate Education and Research Traineeship (DGE-0903715) and NSF Chemistry at the Space Time Limit Center (CCI CHE-1414466).

2.7 References

[1] K.A. Willets, R.P. Van Duyne, Localized surface plasmon resonance spectroscopy and sensing, Ann. Rev. Phys. Chem. 58 (2007) 267-297.

[2] C.E. Talley, J.B. Jackson, C. Oubre, N.K. Grady, C.W. Hollars, S.M. Lane, T.R. Huser, P. Nordlander, N.J. Halas, Surface-enhanced Raman scattering from individual au nanoparticles and nanoparticle dimer substrates, Nano Lett. 5 (2005) 1569-1574.

[3] R.F. Aroca, R.A. Alvarez-Puebla, N. Pieczonka, S. Sanchez-Cortez, J.V. Garcia-Ramos, Surface-enhanced Raman scattering on colloidal nanostructures, Adv. Colloid Interface Sci. 116 (2005) 45-61.

[4] H. Aouani, M. Rahmani, H. Šípová, V. Torres, K. Hegnerová, M. Beruete, J. Homola, M. Hong, M. Navarro-Cía, S.A. Maier, Plasmonic nanoantennas for multispectral surface-enhanced spectroscopies, J. Phys. Chem. C 117 (2013) 18620-18626.

[5] P. Johansson, H. Xu, M. Käll, Surface-enhanced Raman scattering and fluorescence near metal nanoparticles, Phys. Rev. B 72 (2005) 035427.

[6] Z. Zhang, T. Imae, Study of surface-enhanced infrared spectroscopy: 2. Large enhancement achieved through metal-molecule-metal sandwich configurations, J. Colloid Interface Sci. 233 (2001) 107-111.

[7] J. Sung, K.M. Kosuda, J. Zhao, J.W. Elam, K.G. Spears, R.P. Van Duyne, Stability of silver nanoparticles fabricated by nanosphere lithography and atomic layer deposition to femtosecond laser excitation, J. Phys. Chem. C 112 (2008) 5707-5714.

[8] J. He, C.-y. Huang, N. Dai, D.-m. Zhu, Study of surface plasmon resonance of au nanoparticles coated with dielectric layers, SPIE, 2011, pp. 81910N-81910N-81917.

[9] S.M. Mahurin, J. John, M.J. Sepaniak, S. Dai, A reusable surface-enhanced Raman scattering (sers) substrate prepared by atomic layer deposition of alumina on a multi-layer gold and silver film, Appl. Spectrosc. 65 (2011) 417-422.

[10] S.M. George, Atomic layer deposition: An overview, Chem. Rev. 110 (2010) 111-131.

[11] A.C. Dillon, A.W. Ott, J.D. Way, S.M. George, Surface chemistry of al2o3 deposition using al(ch3)3 and h2o in a binary reaction sequence, Surf. Sci. 322 (1995) 230-242.

[12] K. Devloo-Casier, K.F. Ludwig, C. Detavernier, J. Dendooven, In situ synchrotron based X-ray techniques as monitoring tools for atomic layer

deposition, J. Vac. Sci. Technol. A 32 (2014) 14.

[13] R.L. Puurunen, Surface chemistry of atomic layer deposition: A case study for the trimethylaluminum/water process, J. Appl. Phys. 97 (2005) 121301-121301-121352.

[14] D. Berman, J. Krim, Impact of oxygen and argon plasma exposure on the roughness of gold film surfaces, Thin Solid Films 520 (2012) 6201-6206.

[15] Y. Zhang, J.A. Bertrand, R. Yang, S.M. George, Y.C. Lee, Electroplating to visualize defects in al2o3 thin films grown using atomic layer deposition, Thin Solid Films 517 (2009) 3269-3272.

[16] D.E. King, Oxidation of gold by ultraviolet light and ozone at 25 °c, J. Vac. Sci. Technol. A. 13 (1995) 6.

[17] G.L. Gaines Jr, On the water wettability of gold, J. Colloid Interface Sci. 79 (1981) 295.

[18] D.A. Hook, J.A. Olhausen, J. Krim, M.T. Dugger, Evaluation of oxygen plasma and uv ozone methods for cleaning of occluded areas in mems devices, J. of Microelectromech. S. 19 (2010) 1292-1298.

[19] Y.-S. Lin, A surface analysis on oxygen plasma-cleaned gold pattern-plated substrates for wire bondability, Surf. Coat. Technol. 173 (2003) 47-57.

[20] K. Raiber, A. Terfort, C. Benndorf, N. Krings, H.-H. Strehblow, Removal of self-assembled monolayers of alkanethiolates on gold by plasma cleaning, Surf. Sci. 595 (2005) 56-63.

[21] J. Gun, D. Rizkov, O. Lev, M.H. Abouzar, A. Poghossian, M.J. Schoening, Oxygen plasma-treated gold nanoparticle-based field-effect devices as transducer structures for bio-chemical sensing, Microchim. Acta 164 (2009) 395-404.

[22] J. Llorca, A. Casanovas, M. Dominguez, I. Casanova, I. Angurell, M. Seco, O. Rossell, Plasma-activated core-shell gold nanoparticle films with enhanced catalytic properties, J. Nanopart. Res. 10 (2008) 537-542.

[23] A. Fahmi, A. D'Aleo, R.M. Williams, L. De Cola, N. Gindy, F. Voegtle, Converting self-assembled gold nanoparticle/dendrimer nanodroplets into horseshoe-like nanostructures by thermal annealing, Langmuir 23 (2007) 7831-7835.

[24] K. Winkler, T. Wojciechowski, M. Liszewska, E. Gorecka, M. Fialkowski, Morphological changes of gold nanoparticles due to adsorption onto silicon substrate and oxygen plasma treatment, RSC Adv. 4 (2014) 12729-12736.

[25] D. Hohertz, S.F. Romanuik, B.L. Gray, K.L. Kavanagh, Recycling gold nanohole

arrays, J. Vac. Sci. Technol. A 32 (2014) 031403.

[26] C.L. Haynes, R.P. Van Duyne, Nanosphere lithography: A versatile nanofabrication tool for studies of size-dependent nanoparticle optics, J. Phys. Chem. B 105 (2001) 5599-5611.

[27] Y.B. Zheng, B.K. Juluri, B. Kiraly, T.J. Huang, Ordered au nanodisk and nanohole arrays: Fabrication and applications, J. Nanotech. Eng. Med. 1 (2010) 031011-031011.

[28] P. Hanarp, M. Käll, D.S. Sutherland, Optical properties of short range ordered arrays of nanometer gold disks prepared by colloidal lithography, J. Phys. Chem. B 107 (2003) 5768-5772.

[29] A.V. Whitney, J.W. Elam, S. Zou, A.V. Zinovev, P.C. Stair, G.C. Schatz, R.P. Van Duyne, Localized surface plasmon resonance nanosensor: A high-resolution distance-dependence study using atomc layer deposition, J. Phys. Chem. 109 (2005) 20522-20528.

[30] F. Mazzotta, T.W. Johnson, A.B. Dahlin, J. Shaver, S.-H. Oh, F. Höök, Influence of the evanescent field decay length on the sensitivity of plasmonic nanodisks and nanoholes, ACS Photonics 2 (2015) 256-262.

[31] J.C. Peter, S. Naoko, J.B. Anders, F.P. Jose, Stability of reference masses: Vii. Cleaning methods in air and vacuum applied to a platinum mass standard similar to the international and national kilogram prototypes, Metrologia 50 (2013) 532.

[32] T. Smith, The hydrophilic nature of a clean gold surface, J. Colloid Interface Sci. 75 (1980) 51-55.

[33] N.P. Kobayashi, C.L. Donley, S.-Y. Wang, R.S. Williams, Atomic layer deposition of aluminum oxide on hydrophobic and hydrophilic surfaces, J. Cryst. Growth 299 (2007) 218-222.

[34] B.K. Juluri, N. Chaturvedi, Q. Hao, M. Lu, D. Velegol, L. Jensen, T.J. Huang, Scalable manufacturing of plasmonic nanodisk dimers and cusp nanostructures using salting-out quenching method and colloidal lithography, ACS nano 5 (2011) 5838-5847.

CHAPTER 3

LONG DISTANCE DECAY LENGTH STUDY OF ANISOTROPIC GOLD NANOPARTICLES IN THE INFRARED

3.1 Prelude

The following work was in collaboration with Chemistry at the Space Time Limit Center's Dr. N. Large and Dr. G. C. Schatz. Sample fabrication, and empirical data fitting were performed by me. Theoretical calculations were performed by Dr. Large.

3.2 Introduction

The use of plasmonic nanosensors has greatly increased in the past few years. The broad applications from surface enhanced spectroscopies from the UV to the IR coupled with the label-free biosensing options make plasmonic nanosensors an obvious choice for low concentration studies that rely on surface binding events without being effected by bulk conditions changes like temperature or pH.[1-16] The utility of plasmonic nanostructure sensors lies in the close proximity of the evanescent field decay lengths to the nanostructure surface due to localized surface plasmon resonance (LSPR). The decay length of the plasmonic electromagnetic (EM) field is on the order of tens of nanometers to the metal surface that allows for local binding events to be specifically sensed. Structures with sharp-tips are often used to increase sensitivity due to additional

confinement of the plasmonic EM field.[17-19] To broaden the range of sensors, anisotropic nanostructures with polarization-dependent modes can be used to interrogate different regions of the electromagnetic spectrum simultaneously. When well arrayed, the polarization dependence of the resonance modes can be induced by controlling the wavelength and polarization of the incident field.[20-25]

The high-precision of atomic layer deposition (ALD) for thin films has been used to determine the sensitivity reduction based on layer-by-layer thicknesses of nanostructures.[15, 26] ALD of alumina (Al_2O_3) is used due to the precise thickness control and high-quality film formation on high aspect ratio structures as well as its transparency in the visible and near infrared (NIR).[27-31] As a tool for fundamental properties, ALD has also been used to estimate the decay length of nanostructures in the visible.[15, 26, 32] However, monitoring the effect of insulating layers across the visible well into the IR is of utmost importance to establish the utility of the coating. Because each wavelength range is unique to different applications of plasmonic sensors, understanding the behavior of the plasmonic near-field can provide insight to the utility of Al_2O_3.

In order to show the decay length dependence and behavior of the polarization-dependent resonance modes of nanostructures over a broad spectral range, we evaluated the empirical and theoretical response of the LSPR shift of gold nanocrescents (AuNCs) ranging in template size from 250 to 580 nm. Using the decay length estimate by Jung and adapted for nanoparticle systems by Haes, we determined the empirical decay length for AuNCs.[26, 32-34] For a planar noble metal surface. the dependence of the LSPR extinction wavelength maximum, λ_{max}, on refractive index (RI) is expressed as:[32-33, 35]

$$\Delta\lambda_{max} = m\Delta n(1 - e^{-2t/l_d}). \quad (3.1)$$

In Eq 3.1, $\Delta\lambda_{max}$ is the wavelength shift, m is the bulk RI response, Δn is the change in RI of the LSPR induced by an adsorbate, t is the effective adsorbate thickness, and l_d, approximated as an exponential decay, is the characteristic EM field decay length. Notably, this expression was designed for bulk metal (SPR film) measurements although it has been applied to nanoparticle systems in various forms.[34, 36-37] To determine the interaction of the plasmonic field with Al_2O_3 coating, we used finite-difference time-domain (FDTD) theory. Typically, the saturation of the EM near-field as the film grows can be demonstrated by monitoring the red-shift of the LSPR as a function of t. We found that using this description the experiment results of the AuNCs did not behave according to expected literature results for when the aspect ratio of the structure increases.[15, 38] However, both the empirical treatment and theoretical treatment saturated as predicted. We then applied the relative LSPR shift to take into account the sensitivity of the LSPR shift with respect to the resonance wavelength. This treatment showed an excellent match between the trends observed for the experimental and theoretical models.

3.3 Materials and Methods

3.3.1 *Materials*

Gold pellets were purchased from K.J. Lesker (Clairton, PA). Glass substrates of BK7 glass microscope slides were purchased from Ted Pella, Inc. (Redding, CA).Various sizes of 2.6 % w/v polystyrene template nanospheres were purchased from Polysciences, Inc. (Warrington, PA). Absolute ethanol was purchased from Pharmco-Aaper. Concentrated H_2SO_4 and 30 wt% NaOH were purchased from EMD Chemicals. Concentrated HCl and 30% H_2O_2 were purchased from Sigma-Aldrich.

3.3.2 *Substrate Fabrication*

Nanosphere template lithography was used to fabricate the nanocrescents and has been described previously.[20, 39] Briefly, a 45 µL aliquot of diluted polystyrene nanosphere templates was used to spin-cast at 1000 rpm for 30 s. The substrates were placed on 40 ° mounts, with respect to the metal source, in an electron-beam evaporator chamber (Denton SJ20C Vacuum USA, Moorestown, NJ). Gold film was deposited (1 Å/s) as measured by a quartz crystal microbalance (XPC2 Inficon, East Syracuse, NY) under high vacuum (2.0×10^{-6} Torr). An argon ion milling system (PlasmaLab 80 Plus, Oxford Instruments) was used to remove the Au film at 100 W and 10 sccm. After milling, the polystyrene beads were removed by lift-off using transparent tape and samples were stored in nitrogen.

3.3.3 *Atomic Layer Deposition*

A Cambridge NanoTech Fiji F200 Plasma (Cambridge, MA) was used to deposit Al_2O_3 films by ALD on the nanoparticle substrates. Trimethylaluminum and water pulsed alternately in a nitrogen carrier stream using a growth temperature of 43 °C and base pressure of 1.6 mTorr. The process occurred in four steps: (1) 0.06 s pulse of water, (2) 60 s purge with nitrogen, (3) 0.06 s pulse of TMA, and (4) 10 s purge with nitrogen.

3.3.4 *Optical Characterization*

Extinction spectra were collected with a Perkin-Elmer Lambda 750 ultra-violet visible (UV/vis) spectrophotometer.

3.3.5 *Electrodynamic Calculations*

The optical source is taken as a broadband plane wave excitation (total-field scattered-field source), linearly polarized. The FDTD domain is set as a cubic region of $2\times2\times2$ μm^3 with perfectly-matched layers (PMLs) as boundary conditions to mimic an infinite medium. Along the *y*-direction, long axis of the AuNC, symmetric or anti-symmetric boundary conditions are chosen, which depend on the incident polarization. This allows for calculating only half of the simulation domain, thus decreasing the computational cost. A 1 nm conformal mesh is used to describe the nanocrescent geometry and ensure good convergence. An auto shutoff parameter of 10^{-6} was chosen as convergence parameter. The local electric field (near-field) is calculated at a distance of 1.5 nm from each metallic surface. Dielectric permittivities used in the FDTD calculations for gold are those tabulated by Johnson & Christy[40] for the spectral range up to 2 μm, and by Palik[41] for the range 2-3 μm. We use a constant refractive index of $n = 1.765$ and 1.456 for Al_2O_3 and SiO_2, respectively.

3.4 Results

The decay length (l_d) and the response to the Al_2O_3 coating of the dipolar resonance modes of the AuNCs were determined in three ways: experimentally via ALD, empirically by fitting the experimental results to Eq. 1, and theoretically using FDTD simulations.[42]

The AuNCs were prepared by nanospheres template lithography (NTL) using four polystyrene template diameters; 154, 220, 356, and 505 nm. This size range allowed us to probe the tail end of the visible range (900 nm) to well into the IR region (>2200 nm).

The diameter of the AuNCs generated from these templates were 250, 300, 425, and 589 nm, designated as $AuNC_{size}$. Al_2O_3 was deposited using ALD and Al_2O_3 growth was monitored using scanning electron microscopy (SEM, FEI NovaNano). To establish the Al_2O_3 growth per cycle (GPC) of the ALD system, the in-plane diameter of AuNCs were measured over 0-800 AB cycles of Al_2O_3. Using SEM images of $AuNC_{250}$ and $AuNC_{580}$ (Figure 3.1), the diameter of 14-20 nanoparticles per deposition was determined using ImageJ. The GPC was determined to be 0.08 Å/cycle based on the increase in radius per cycle as measured at 0, 150, 200, 400, 600, and 800 cycles. This is a conservatively low estimate due to the limits of SEM resolution along the edge of the Al_2O_3 but is in agreement with other reported Al_2O_3 growth rates.[26, 43] The linear growth demonstrates that Al_2O_3 is deposited continuously and uniformly for the size range of the study ($AuNC_{250}$ vs. $AuNC_{580}$ template).

For each nanosphere template diameter, 18 samples were prepared. From these, subsets composed of three samples (N=3) were used for statistical analysis of optical properties determined by UV-visible extinction spectroscopy. Deposition occurred in two sets of consecutive cycles, the first included 50, 100, 300, 500, or 700 AB cycles (N=3 per set). The optical properties were characterized and then the samples were cleaned with ultraviolet-ozone (UVO) to prep the surface for a second deposition of 100 AB cycles to yield totals of 150, 200, 400, 600, or 800 AB cycles. The use of UVO to prepare Au nanostructures for Al_2O_3 deposition has been shown previously.[44] A control set of samples underwent parallel analysis and cleaning procedure without the addition of Al_2O_3 (referred to as 0 AB cycles).

The initial LSPR maxima of the short axis (λ_{SA}) and long axis (λ_{LA}) resonance

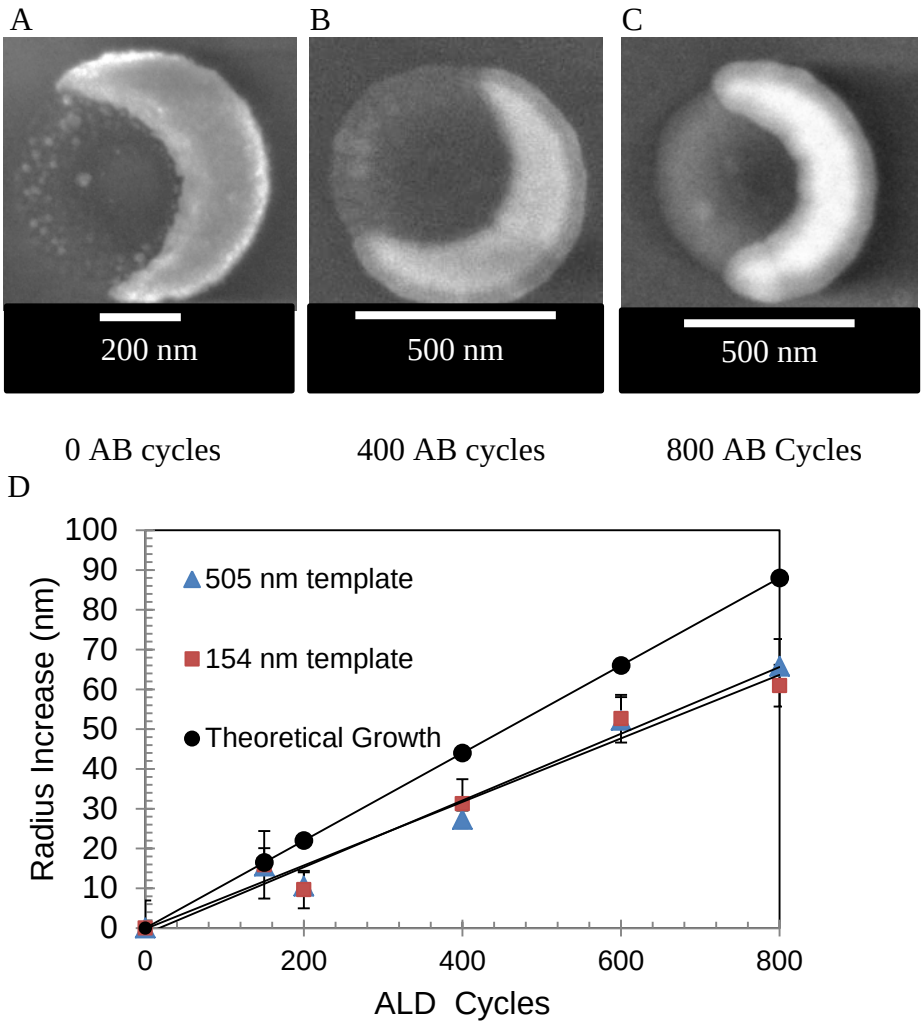

Figure 3.1 Growth rate calculations based on SEM imaging. Each nanocrescent is a representative structure for measurements made at (A) 0 (B) 400 and (C) 800 AB cycles. (D) The radius of the nanocrescent at each growth cycle compared to the theoretical growth of 0.11 Å/cycle. The linear value for the $AuNC_{580}$ template is $y = 0.084x - 1.480$. The linear value for the $AuNC_{250}$ nm template growth is $y = 0.080x - 0.210$.

modes for the $AuNC_{250}$, $AuNC_{300}$, $AuNC_{425}$, and $AuNC_{580}$ structures are shown in Table 3.1. The long axis resonance mode for the $AuNC_{580}$ structures was not characterized because the glass substrate competes with the λ_{LA} in the IR region. The NTL process is exceedingly sensitive to minor changes in angle and distance relative to the metal source. As the position varies, minor morphological parameters such as the AuNC backbone width and tip-to-tip distance will vary. As a result of the sensitivity and minor morphological changes, the absolute value of the LSPR for the complete sample set (N=18) fluctuated despite otherwise identical fabrication conditions. However, the *change* in the LSPR across these wavelengths was relatively uniform. Representative spectra for the $AuNC_{300}$ structures are shown in Figure 3.2. The diagnostic features of saturated sensing volume are that the extinction maxima stops shifting, the peak broadens, and the peak intensity decreases.[38] As the Al_2O_3 exceeds the l_d, the AuNC EM - field no longer responds to additional material deposition; ergo, the LSPR no longer red-shifts. The peak intensity increases from approximately 0 to 300 cycles of Al_2O_3 and then begins to decrease from 300 cycles on. The initial jump in the spectra from 0 to 50 ALD cycles (4-5 nm) is due to the high sensitivity of nanostructures to its local environment within the first 10 nm and would be expected to be characteristically linear within that range.[15, 26, 32]

Table 3.1 λ_o of the experimental and theoretical model

	$\lambda_{o\ (nm)}$			
	SA Exp.	SA Theo.	LA Exp.	LA Theo.
$AuNC_{250}$	890-1010	858	1270-1470	1279
$AuNC_{300}$	1140-1170	948	1560-1800	1495
$AuNC_{425}$	1280-1550	1148	2080-2200	2000

(A) Short Axis

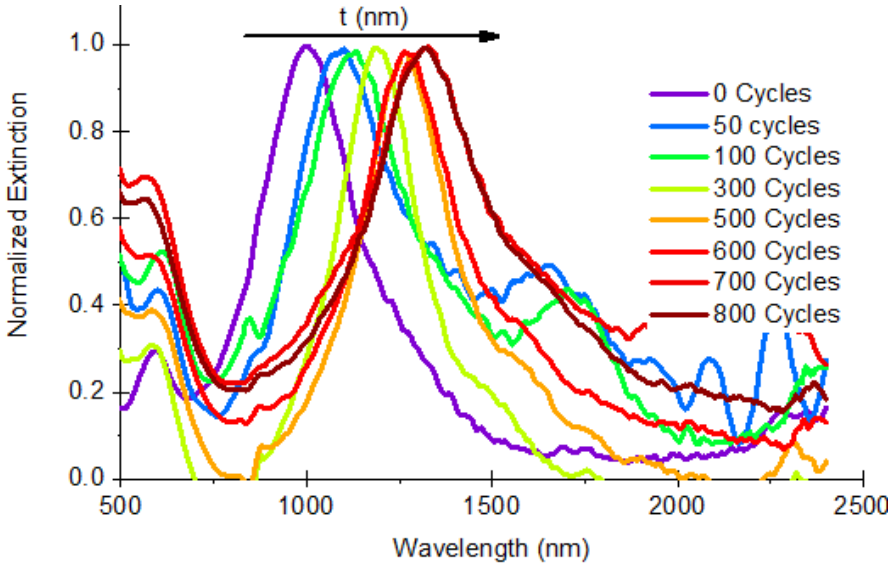

(B) Long Axis

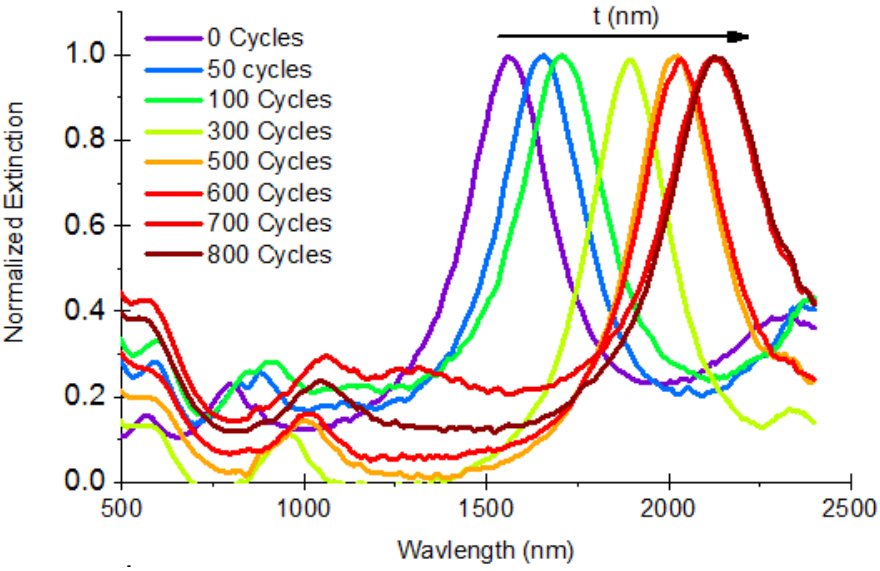

Figure 3.2 Polarization-dependent LSPR shift of $AuNC_{300}$ nm from 0 to 800 AB cycles of alumina: (A) Short axis and (B) long axis.

As the sensing volume saturates (the Al_2O_3 exceeds the distance of the plasmonic near-field) the spectral shift saturates and levels as shown in Figure 3.3. To estimate the l_d of the nanostructures, the shift (Figure 3.3) is fit to Eq. 1. The bulk refractive index sensitivity, *m*, is determined from previously published data,[20] where it has been established that 35 nm thick AuNCs have relative sensitivities of 26.8% (of eV) for 125-410 nm templated structures. By using the wavelength range for each sample set (N=18), the average *m* was determined from the relative sensitivity. The *m* of each sample was independently determined, thus the standard deviation of the calculated *m* originates from the range of the experimentally determined λ_{LA} and λ_{SA} (Table 3.1).

The l_d of the evanescent field is calculated from the peak shifts due to Al_2O_3 deposition using Eq. 1. The l_d listed in Table 3.2 were used to fit the empirical ($\Delta\lambda$ vs. *t*) model as to minimize the percent error from the experimental $\Delta\lambda$. The results of the empirical fit to $\Delta\lambda$ are overlayed with the experimental in Figure 3.3. The SA estimate for the l_d produced a particularly well-matched calculated $\Delta\lambda$ to the experimental values with less than 5% error. The $AuNC_{580}$ had a SA l_d = 120 nm, but the high degree of error from the empirically calculated and experimental suggests that another effect may be dominating the refractive index response of the nanoparticles. In terms of long-distance decay, the error of the fit for the SA and LA of the $AuNC_{250}$, $AuNC_{300}$, and $AuNC_{425}$ drops to 10 and 6.4%, 9.7 and 5.1%, and 1.6 and 9.8%, respectively. This suggests that the empirical model describes the *long-distance* plasmonic decay characteristics of the AuNCs more closely.

In addition to the empirical comparison, finite-difference time-domain (FDTD) electrodynamic calculations were performed to predict and interpret the $\Delta\lambda$ of the

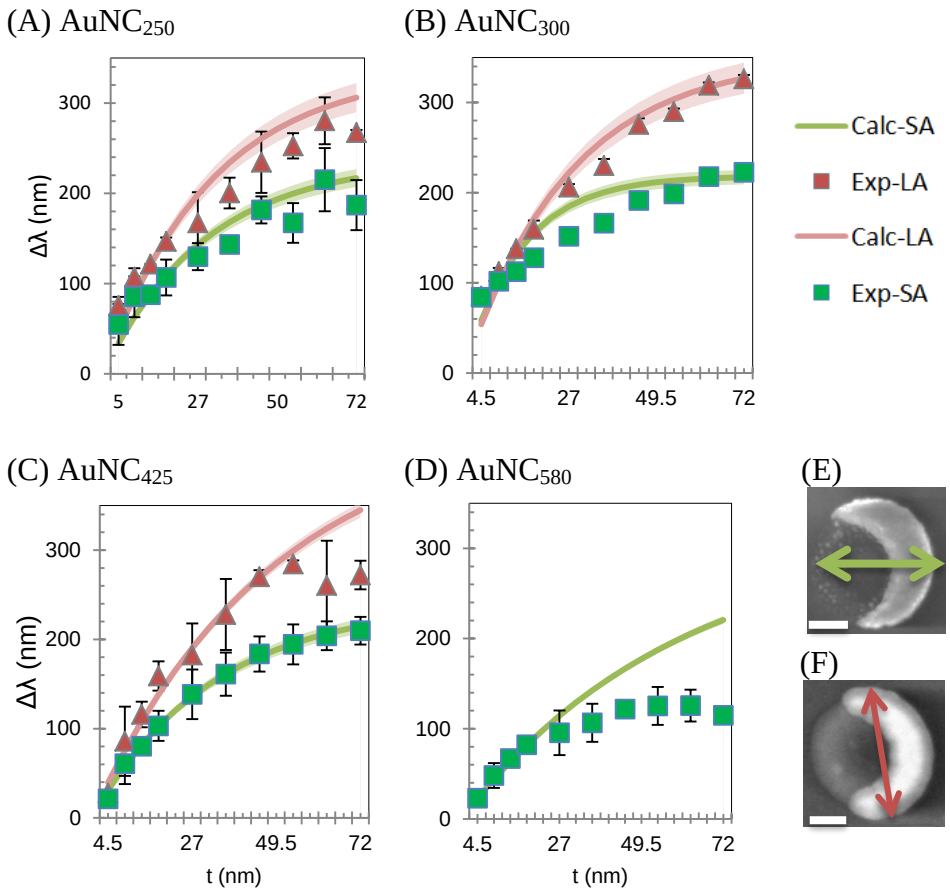

Figure 3.3 LSPR Δλ of long (red) and short (green) axis dipole resonance modes after deposition of Al_2O_3 on (A) $AuNC_{250}$, (B) $AuNC_{300}$, (C) $AuNC_{425}$, and (D) $AuNC_{580}$. SEM images of single $AuNC_{580}$ with arrows denoting polarization (E) No Al_2O_3 and long axis and (F) 800 AB cycles and short axis (SA). Scale bars are 200 nm.

Table 3.2 Calculated values for m and l_d

	Short Axis Dipole					Long Axis Dipole				
Template	m (nm/RIU)		σ	l_d (nm)	% Error	m (nm/RIU)		σ	l_d (nm)	% Error
$AuNC_{250}$	308.1	±	14.1	58	12.7	439.0	±	23.2	61	11.3
$AuNC_{300}$	336.5	±	12.3	53	13.1	540.5	±	28.6	76	10.5
$AuNC_{425}$	370.8	±	7.1	82	4.6	686.2	±	17.1	125	11.8
$AuNC_{580}$	485.7	±	9.5	120	20.4	-	-	-	-	-

$AuNC_{250}$, $AuNC_{300}$, and $AuNC_{425}$ structures. As the Al_2O_3 thickness increased, the average near-field intensity spatial distribution at the dipolar LSPR changes (Appendix A3.1-3.3). At t=40 nm, the AuNC is completely embedded in Al_2O_3. For thin Al_2O_3 layers, the local electric field tends to be localized at the Al_2O_3 surface. When the Al_2O_3 layer reaches a critical thickness t, the electric field re-localizes at the metal-dielectric interface. This trend has already been observed in other nanostructures such as Cu_2O-coated Ag nanoparticles.[45] The LSPR shift of the theoretical simulations was compared against the experimental shift as a function of t (Figure 3.4). In all three cases, the theoretical results over-estimate the $\Delta\lambda$ when compared to the experimental $\Delta\lambda$ as a function of t.

3.5 Discussion

The theoretical and empirical models follow the expected result: an overall size increase leads to an increase in the saturation thickness (t_{sat}). The trend with Al_2O_3 thickness is clear in all FDTD cases: The plasmonic near-field at the metal surface recedes when introducing the Al_2O_3 layer, which is expected due to the drastic change in refractive index of the environment. The near-field then continues decreasing for Al_2O_3 layer up to 40 nm, indicating the near-field tends to be pushed away to the Al_2O_3 surface. Finally, when the Al_2O_3 layer becomes thicker, the near-field at the metal surface increases again and saturates, in agreement with previously published work.[45]

It has been proposed that the best comparison tool for nanoparticle sensing is the aspect ratio (AR); as AR increases, the sensing volume increases.[15, 32, 46] Generally, if the height is maintained, an increase in the length of a nanostructure would therefore increase

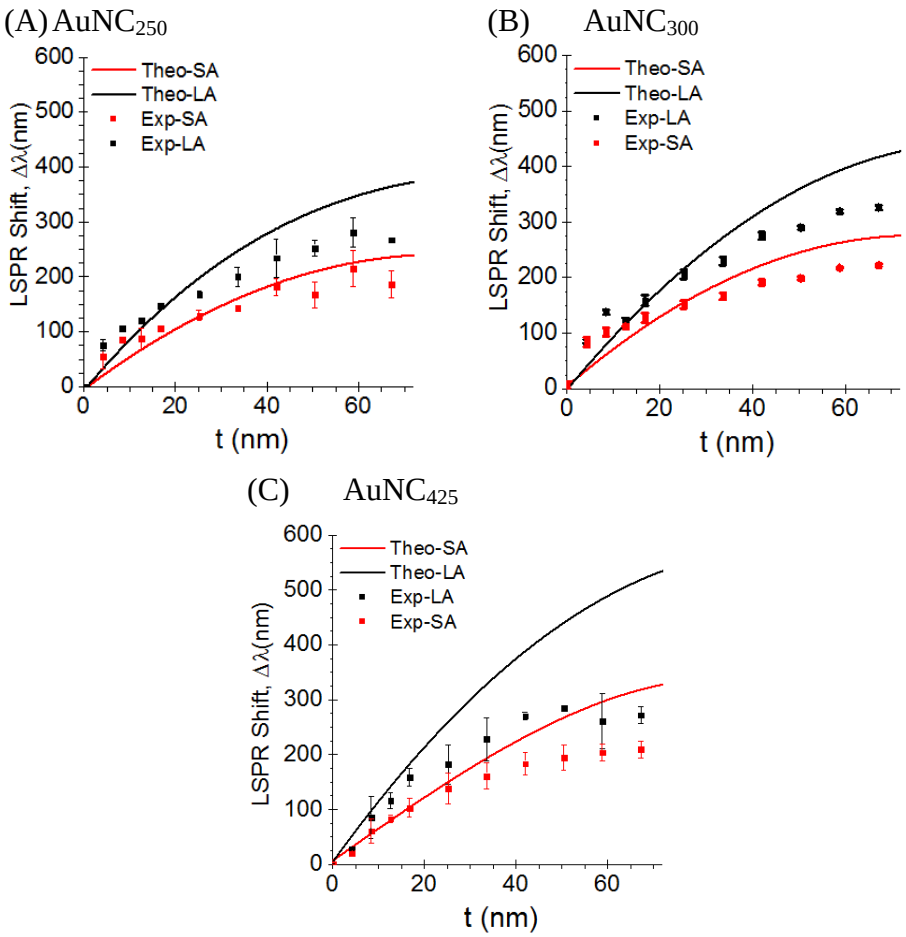

Figure 3.4 Theoretical (FDTD, solid lines) versus experimental (markers) Δλ shifts for three AuNC samples: (A) $AuNC_{250}$, (B) $AuNC_{300}$, and (C) $AuNC_{425}$. In each case, both the SA and LA configurations are shown.

the saturation thickness and increased the maximum LSPR wavelength.[26, 32, 38, 47] The AuNC system has three potential aspect ratios for comparison: the in-plane length to backbone width (*L* and *W*, respectively), in-plane length to height (*L*:*H*), and backbone width to height (*W*:*H*) (summarized in Appendix A.4).

The aspect ratio comparing *L*:*W* ($AR_{L:W}$) of the AuNCs from smallest to largest structure is 2.5, 3.0, 3.4, and 2.9. The two most similar structures, $AuNC_{300}$ ($AR_{L:W}$ = 3.0) and $AuNC_{580}$ ($AR_{L:W}$ = 2.9), have dissimilar saturation and maximum shift for experimental trends. The saturation thickness (t_{sat}) was estimated by difference between two Δλ data points. As the slope of the Δλ approaches zero, the signal saturates. The amount of Al_2O_3 deposited at this point is estimated as the t_{sat}. This estimate allows for the comparison across structure sizes. The empirical method shows the t_{sat} increases with AR, with the exception of the $AuNC_{580}$ (Appendix A.4.A).

The $AR_{L:H}$ increases from $AuNC_{250}$ to the $AuNC_{580}$ linearly, which is expected to cause the values for both t_{sat} and λ_{max} to increase.[15, 32, 46] This trend was not observed for the experimental results but the trend is shown in the empirical fit (Figure 3.3) and the theoretical model (Figure 3.4). Current literature examples of sensing volume with respect to AR are based on moderately simple structures, but also within the confines of the visible spectrum and near IR. For example, silver nanotriangles with 60% decrease in $AR_{L:H}$ yield decreased λ_{max} of 53-86 %.[38] Using Au nanoholes and nanodisk substrates, Mazzotta et al. showed that the sensitivity of structures is determined by the AR of the nanostructures whereas the l_d depends on the type of structure.[15] Using 110:20 (length:height), ($AR_{L:H}$ = 5) compared to 150:30 ($AR_{L:H}$ = 5.5) nanodisks, a 90% decrease in AR has a 75 % decrease in $\Delta\lambda_{max}$. The AuNCs represent the tail-end of the

visible well into the IR region whereas the two examples of silver nanotriangles and gold nanodisks are within the visible (600-800 nm for both structures). To the authors' knowledge, this is the first experimental l_d study on similar structures in such a broad range of the EM spectrum. The behavior of the AuNC going into the mid and far IR could contribute to the behavior of the λ_{max} and t_{sat}

To determine the sensitivity or relative shift as a result of Al_2O_3 deposition when AR remains constant but structure parameters (size) vary greatly, the fractional shift, $\Delta\lambda/\lambda_o$, is used. The $\Delta\lambda/\lambda_0$ of the theoretical model and the experimental results are shown in two formats, by structure size (Figure 3.5) and by resonance mode (Figure 3.6), allowing for different observations.

From Figure 3.5, it can be shown that the $\Delta\lambda/\lambda_0$ of the LA and SA for either experimental or theoretical $\Delta\lambda/\lambda_0$ of any given substrate are closely associated. Specifically, in both $AuNC_{250}$ sets (experimental and theoretical $\Delta\lambda/\lambda_0$), the LA more closely tracks with the SA than in either of the larger structures. The experimental $AuNC_{250}$ $\Delta\lambda/\lambda_0$ is the only to overlap consistently throughout *t*, strengthening that this response is very similar to the theoretical $\Delta\lambda/\lambda_0$. The $AuNC_{300}$ (Figure 3.5B) and The $AuNC_{425}$ (Figure 3.5C) show the SA tracking with a slightly higher $\Delta\lambda/\lambda_0$ than the LA in both experimental and theoretical $\Delta\lambda/\lambda_0$. However, for the theoretical $AuNC_{425,}$ the SA and LA diverge after 40 nm, corresponding to a similar divergence in the experimental $\Delta\lambda/\lambda_0$.

The behavior of the SA $\Delta\lambda/\lambda_0$ and LA $\Delta\lambda/\lambda_0$ can be evaluated independently using Figure 3.6. In both the SA and LA, the smaller structures are very closely related to each other. Despite the much larger t_{sat} and λ_{max}, the $AuNC_{425}$ have the smallest $\Delta\lambda/\lambda_0$

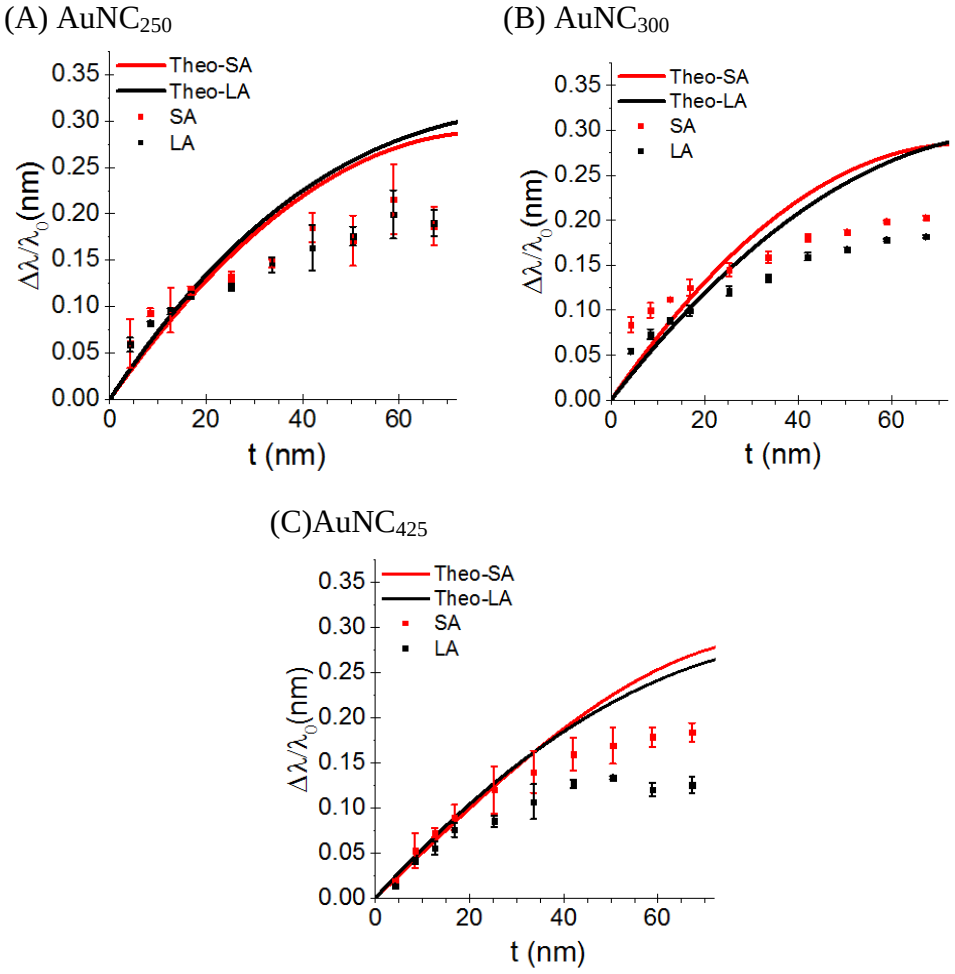

Figure 3.5 Fractional shifts of theoretical (solid lines) and experimental (data points) λ_{max}: (A) $AuNC_{250}$, (B) $AuNC_{300}$, and (C) $AuNC_{425}$.

(A)

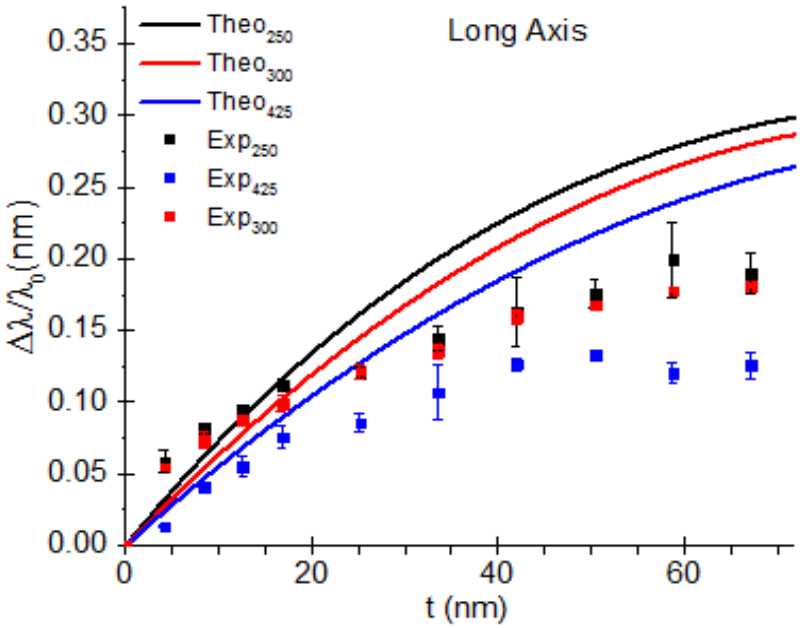

(B)

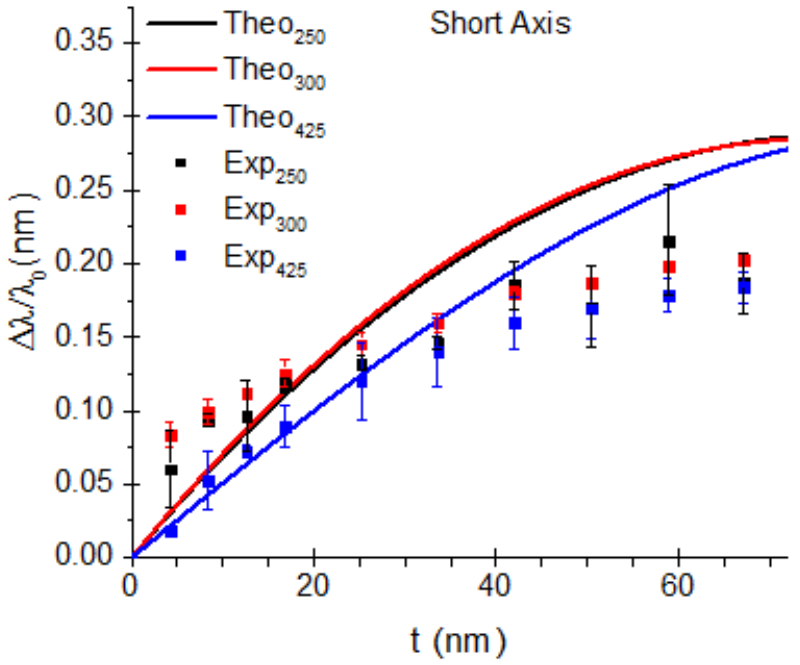

Figure 3.6 Fractional shifts of theoretical (solid lines) and experimental shifts (data points) of the (A) long axis and (B) short axis.

regardless of experimental or theoretical $\Delta\lambda/\lambda_0$. The SA_{250} has the highest $\Delta\lambda/\lambda_o$ for much of the range in both theoretical and experimental comparisons.

3.6 Conclusion

Unlike the work done with nanotriangles, nanohole, or nanodisk arrays, the absolute shift compared to any single physical variable does not change the apparent saturation thickness or the maximum LSPR shift of the experimental AuNC system. However, when the fractional shift is used, the AuNC systems fall in line with literature. Current work to address the theoretical and experimental mismatch includes developing a more realistic geometry of the AuNCs, such as rounded tips. This is expected to decrease the sensitivity of the theoretical model and blue-shift of the spectra.

The behavior of the largest nanocrescent, the $AuNC_{589}$, has yet to be explained. The severe drop-off of the t_{sat} and shift compared to smaller structures suggest that the large AuNC is less efficient or has an unexpected, short l_d. Au is a lossy resonator in the mid-IR, owing to high electron concentration and inter-intraband transitions,[40] which may explain some of the inefficiency. The effect of grain boundaries on the plasmonic response should also be investigated.[48]

3.7 References

1. Soares, L.; Csaki, A.; Jatschka, J.; Fritzsche, W.; Flores, O.; Franco, R.; Pereira, E. Localized Surface Plasmon Resonance (Lspr) Biosensing Using Gold Nanotriangles: Detection of DNA Hybridization Events at Room Temperature. *Analyst* **2014,** *139* (19), 4964-4973.

2. Doria, G.; Conde, J.; Veigas, B.; Giestas, L.; Almeida, C.; Assunção, M.; Rosa, J.; Baptista, P. V. Noble Metal Nanoparticles for Biosensing Applications. *Sensors* **2012,** *12* (2), 1657.

3. Raphael, M. P.; Christodoulides, J. A.; Mulvaney, S. P.; Miller, M. M.; Long, J. P.; Byers, J. M. A New Methodology for Quantitative Lspr Biosensing and Imaging. *Anal. Chem.* **2011,** *84* (3), 1367-1373.

4. He, X.; Wang, K.; Cheng, Z. In Vivo near-Infrared Fluorescence Imaging of Cancer with Nanoparticle-Based Probes. *Wiley Interdiscip. Rev. Nanomed. Nanobiotechnol.* **2010,** *2* (4), 349-366.

5. Aizpurua, J.; Hanarp, P.; Sutherland, D. S.; Käll, M.; Bryant, G. W.; García de Abajo, F. J. Optical Properties of Gold Nanorings. *Phys. Rev. Lett.* **2003,** *90* (5), 057401.

6. Hanarp, P.; Käll, M.; Sutherland, D. S. Optical Properties of Short Range Ordered Arrays of Nanometer Gold Disks Prepared by Colloidal Lithography. *J. Phys. Chem. B* **2003,** *107* (24), 5768-5772.

7. Neddersen, J.; Chumanov, G.; Cotton, T. M. Laser Ablation of Metals: A New Method for Preparing Sers Active Colloids. *Appl. Spectrosc.* **1993,** *47* (12), 1959-1964.

8. Kahl, M.; Voges, E.; Kostrewa, S.; Viets, C.; Hill, W. Periodically Structured Metallic Substrates for Sers. *Sens. Actuators, B* **1998,** *51* (1–3), 285-291.

9. Kennedy, B. J.; Spaeth, S.; Dickey, M.; Carron, K. T. Determination of the Distance Dependence and Experimental Effects for Modified Sers Substrates Based on Self-Assembled Monolayers Formed Using Alkanethiols. *J. Phys. Chem. B* **1999,** *103* (18), 3640-3646.

10. Sánchez-Cortés, S.; Domingo, C.; García-Ramos, J. V.; Aznárez, J. A. Surface-Enhanced Vibrational Study (Seir and Sers) of Dithiocarbamate Pesticides on Gold Films. *Langmuir* **2001,** *17* (4), 1157-1162.

11. Le, F.; Brandl, D. W.; Urzhumov, Y. A.; Wang, H.; Kundu, J.; Halas, N. J.; Aizpurua, J.; Nordlander, P. Metallic Nanoparticle Arrays: A Common Substrate for Both Surface-Enhanced Raman Scattering and Surface-Enhanced Infrared Absorption. *ACS Nano* **2008,** *2* (4), 707-718.

12. Küstner, B.; Gellner, M.; Schütz, M.; Schöppler, F.; Marx, A.; Ströbel, P.; Adam, P.; Schmuck, C.; Schlücker, S. Sers Labels for Red Laser Excitation: Silica-Encapsulated Sams on Tunable Gold/Silver Nanoshells. *Angew. Chem. Int. Ed.* **2009,** *48* (11), 1950-1953.

13. Bantz, K. C.; Meyer, A. F.; Wittenberg, N. J.; Im, H.; Kurtulus, O.; Lee, S. H.; Lindquist, N. C.; Oh, S.-H.; Haynes, C. L. Recent Progress in Sers Biosensing. *PCCP* **2011,** *13* (24), 11551-11567.

14. Mahurin, S. M.; John, J.; Sepaniak, M. J.; Dai, S. A Reusable Surface-Enhanced Raman Scattering (Sers) Substrate Prepared by Atomic Layer Deposition of

Alumina on a Multi-Layer Gold and Silver Film. *Appl. Spectrosc.* **2011,** *65* (4), 417-422.

15. Mazzotta, F.; Johnson, T. W.; Dahlin, A. B.; Shaver, J.; Oh, S.-H.; Höök, F. Influence of the Evanescent Field Decay Length on the Sensitivity of Plasmonic Nanodisks and Nanoholes. *ACS Photonics* **2015,** *2* (2), 256-262.

16. Anker, J. N.; Hall, W. P.; Lyandres, O.; Shah, N. C.; Zhao, J.; Van Duyne, R. P. Biosensing with Plasmonic Nanosensors. *Nat. Mater.* **2008,** *7* (6), 442-453.

17. Khoury, C. G.; Vo-Dinh, T. Gold Nanostars for Surface-Enhanced Raman Scattering: Synthesis, Characterization and Optimization. *J. Phys. Chem. C* **2008,** *112* (48), 18849-18859.

18. Langille, M. R.; Personick, M. L.; Zhang, J.; Mirkin, C. A. Defining Rules for the Shape Evolution of Gold Nanoparticles. *J. Am. Chem. Soc.* **2012,** *134* (35), 14542-14554.

19. Siddiquee, A. M.; Taylor, A. B.; Syed, S.; Lim, G.-H.; Lim, B.; Chon, J. W. M. Measurement of Plasmon-Mediated Two-Photon Luminescence Action Cross Sections of Single Gold Bipyramids, Dumbbells, and Hemispherically Capped Cylindrical Nanorods. *J. Phys. Chem. C* **2015,** *119* (51), 28536-28543.

20. Bukasov, R.; Shumaker-Parry, J. S. Highly-Tunable Infrared Extinction Properties of Gold Nanocrescents. *Nano Lett.* **2007,** *7*, 1113-1118.

21. Bukasov, R.; Shumaker-Parry, J. S. Siver Nanocrescents with Infrared Plasmonic Properties as Tunable Substrates for Surface Enhanced Infrared Absorption Spectrscopy. *Anal. Chem.* **2009,** *81* (4531-4535).

22. Bukasov, R.; Ali, T. A.; Nordlander, P.; Shumaker-Parry, J. S. Probing the Plasmonic near-Field of Gold Nanocrescent Antennas. *ACS Nano* **2010,** *4* (11), 6639-6650.

23. Cooper, C. T.; Rodriguez, M.; Blair, S.; Shumaker-Parry, J. S. Polarization Anisotropy of Multiple Localized Plasmon Resonance Modes in Noble Metal Nanocrescents. *J. Phys. Chem. C* **2014,** *118* (2), 1167–1173.

24. Cooper, C. T.; Rodriguez, M.; Blair, S.; Shumaker-Parry, J. S. Mid-Infrared Localized Plasmons through Structural Control of Gold and Silver Nanocrescents. *J. Phys. Chem. C* **2015,** *119* (21), 11826–11832.

25. Swartz, M.; Rodriguez, M.; Quast, A. D.; Cooper, C. T.; Blair, S.; Shumaker-Parry, J. S. Aluminum Nanocrescent Plasmonic Antennas Fabricated by Copper Mask Nanosphere Template Lithography. *J. Phys. Chem. C* **2016**.

26. Whitney, A. V.; Elam, J. W.; Zou, S.; Zinovev, A. V.; Stair, P. C.; Schatz, G. C.; Van Duyne, R. P. Localized Surface Plasmon Resonance Nanosensor: A High-

Resolution Distance-Dependence Study Using Atomc Layer Deposition. *J. Phys. Chem.* **2005,** *109*, 20522-20528.

27. Zhang, Y.; Bertrand, J. A.; Yang, R.; George, S. M.; Lee, Y. C. Electroplating to Visualize Defects in Al2o3 Thin Films Grown Using Atomic Layer Deposition. *Thin Solid Films* **2009,** *517* (11), 3269-3272.

28. Zhang, Y.; Seghete, D.; Abdulagatov, A.; Gibbs, Z.; Cavanagh, A.; Yang, R.; George, S.; Lee, Y.-C. Investigation of the Defect Density in Ultra-Thin Al2o3 Films Grown Using Atomic Layer Deposition. *Surf. Coat. Technol.* **2011,** *205* (10), 3334-3339.

29. Groner, M. D.; Fabreguette, F. H.; Elam, J. W.; George, S. M. Low-Temperature Al2o3 Atomic Layer Deposition. *Chem. Mater.* **2004,** *16* (4), 639-645.

30. George, S. M. Atomic Layer Deposition: An Overview. *Chem. Rev.* **2010,** *110* (1), 111-131.

31. Kischkat, J.; Peters, S.; Gruska, B.; Semtsiv, M.; Chashnikova, M.; Klinkmüller, M.; Fedosenko, O.; Machulik, S.; Aleksandrova, A.; Monastyrskyi, G.; Flores, Y.; Ted Masselink, W. Mid-Infrared Optical Properties of Thin Films of Aluminum Oxide, Titanium Dioxide, Silicon Dioxide, Aluminum Nitride, and Silicon Nitride. *Appl. Opt.* **2012,** *51* (28), 6789-6798.

32. Haes, A. J.; Zou, S.; Schatz, G. C.; Van Duyne, R. P. Nanoscale Optical Biosensor: Short Range Distance Dependence of the Localized Surface Plasmon Resonance of Noble Metal Nanoparticles. *J. Phys. Chem. B* **2004,** *108* (22), 6961-6968.

33. Jung, L. S.; Campbell, C. T.; Chinowsky, T. M.; Mar, M. N.; Yee, S. S. Quantitative Interpretation of the Response of Surface Plasmon Resonance Sensors to Adsorbed Films. *Langmuir* **1998,** *14* (19), 5636-5648.

34. Haes, A. J.; Van Duyne, R. P. A Nanoscale Optical Biosensor: Sensitivity and Selectivity of an Approach Based on the Localized Surface Plasmon Resonance Spectroscopy of Triangular Silver Nanoparticles. *J. Am. Chem. Soc.* **2002,** *124* (35), 10596-10604.

35. Jung, L. S.; Campbell, C. T.; Chinowsky, T. M.; Mar, M. N.; Yee, S. S. Quantitative Interpretation of the Response of Surface Plasmon Resonance Sensors to Adsorbed Films. *Langmuir* **1998,** *14*, 5636-56487.

36. Malinsky, M. D.; Kelly, K. L.; Schatz, G. C.; Van Duyne, R. P. Nanosphere Lithography: Effect of Substrate on the Localized Surfac Plasmon Resonance Spectrum of Silver Nanoparticles. *J. Phys. Chem. B* **2001,** *105*, 2343-2350.

37. Kedem, O.; Tesler, A. B.; Vaskevich, A.; Rubinstein, I. Sensitivity and Optimization of Localized Surface Plasmon Resonance Transducers. *ACS Nano*

2011, *5* (2), 748-760.

38. Haes, A. J.; Zou, S.; Schatz, G. C.; Van Duyne, R. P. A Nanoscale Optical Biosensor: The Long Range Distance Dependence of the Localized Surface Plasmon Resonance of Noble Metal Nanoparticles. *J. Phys. Chem. B* **2004,** *108* (1), 109-116.

39. Shumaker-Parry, J. S.; Rochholz, H.; Kreiter, M. Fabrication of Crescent-Shaped Optical Antennas. *Adv. Mater.* **2005,** (17), 2131-2134.

40. Johnson, P. B.; Christy, R. W. Optical Constants of the Noble Metals. *Phys. Rev. B* **1972,** *6* (12), 4370-4379.

41. Palik, E. D., Chapter 1 - Introductory Remarks. In *Handbook of Optical Constants of Solids*, Academic Press: Burlington, 1997; pp 3-12.

42. Lumerical Solutions, Inc. http://www.lumerical.com/tcad-products/fdtd/

43. Masango, S. S.; Hackler, R. A.; Large, N.; Henry, A.-I.; McAnally, M. O.; Schatz, G. C.; Stair, P. C.; Van Duyne, R. P. High-Resolution Distance Dependence Study of Surface-Enhanced Raman Scattering Enabled by Atomic Layer Deposition. *Nano Lett.* **2016,** *16* (7), 4251-4259.

44. Lancaster, C. A.; Shumaker-Parry, J. S. Surface Preparation of Gold Nanostructures on Glass by Ultraviolet Ozone and Oxygen Plasma for Thermal Atomic Layer Deposition of Al2o3. *Thin Solid Films* **2016,** *612*, 141-146.

45. Jing, H.; Large, N.; Zhang, Q.; Wang, H. Epitaxial Growth of Cu2o on Ag Allows for Fine Control over Particle Geometries and Optical Properties of Ag–Cu2o Core–Shell Nanoparticles. *J. Phys. Chem. C* **2014,** *118* (34), 19948-19963.

46. Zeman, E. J.; Schatz, G. C. An Accurate Electromagnetic Theory Study of Surface Enhancement Factors for Slver, Gold, Copper, Lithium, Sodium, Aluminum, Gallium, Indium, Zinc, and Cadmium. *J. Phys. Chem.* **1987,** *91* (3), 634-643.

47. Im, H.; Lindquist, N. C.; Lesuffleur, A.; Oh, S.-H. Atomic Layer Deposition of Dielectric Overlayers for Enhancing the Optical Properties and Chemical Stability of Plasmonic Nanoholes. *ACS Nano* **2010,** *4* (2), 947-954.

48. Zhou, C.; Yu, J.; Qin, Y.; Zheng, J. Grain Size Effects in Polycrystalline Gold Nanoparticles. *Nanoscale* **2012,** *4* (14), 4228-4233.

CHAPTER 4

PARASITIC SYNTHESIS: USING TOP-DOWN FABRICATION TO GENERATE HOST NANOSTRUCTURES FOR BOTTOM-UP SYNTHESIS OF BRANCHED NANOPARTICLES

4.1 Introduction

Surface-enhanced spectroscopy (SES) substrates take advantage of the localized surface plasmon resonance (LSPR) of nanoparticles. LSPR refers to the coherent oscillation of conduction band electrons on metal surfaces in response to the electric field of incident light. The electron oscillation can be confined into structural regions of the nanostructure, such as sharp tips, generating a local electromagnetic (EM) field that gives rise to enhancement of the vibrational signals of attached or nearby molecules.[1] Additionally, the plasmonic near-field generated by the nanostructures is sensitive to changes in the local refractive index and is used in biosensing.[2] In this chapter, a novel substrate for increased surface enhancement for spectroscopy and refractive index sensing is proposed that combines synthetic (bottom-up) and fabrication (top-down) strategies to combine the benefits of both: high sensitivity without risk of aggregation.

In early SES substrate designs, nanoparticle aggregates and roughened metal surfaces were used to achieve SERS enhancement values of ~10^5.[1] However, the use of

these substrates lacked reproducibility due to aggregation and uncontrolled surface morphology.[2] The development of synthetic routines that utilized capping agents to direct nanoparticle growth introduced a broad range of substrate designs with improved sensitivity. Of the modern synthetic designs, structures with branches ending in sharp-tips, called nanostars, have been particularly appealing due to their high-enhancement for SES.[3-9]

4.1.1 *Synthetic Strategies*

Plasmonic nanoparticles can be synthesized via several routes including co-precipitation, chemical reduction, photochemical reduction, and thermal decomposition.[10-18] Each of these techniques includes two subsets of reactions: seed-mediated and non-seed strategies. The use of traditional seed methodology relies on the passivation of crystalline facets of seed nanoparticles to reduce the gold (Au) precursor in a specific orientation. Facet passivation by a capping agent has been well studied and many geometries have been developed in addition to nanostars, including nanorods, dumbbells, and dog bones.[19-21] Non-seed strategies, or "one-pot" syntheses, offer similar geometric flexibility while utilizing fewer reactants to simplify purification and protocol. In both cases, nanoparticle synthesis is incredibly sensitive to changes in the chemical environment, allowing for particle customization. For example, branching in nanostars can be controlled by pH, temperature, the choice and concentration of reducing agent.[22-23]

Nanostars have several synthetic pathways that have been used to tailor the branch lengths and overall size. Minati et al.[24] reported a simple, three-reactant (hydroxylamine, $HAuCl_4$, and NaOH), one-pot synthesis to produce nanostars with a core

diameter of 42.5 nm (± 5 nm) and branch length of 8 nm (± 3 nm) at a pH of 11. By manipulating the pH, the authors demonstrated control over seed-mediated and one-pot syntheses using the same three components. The nanostars from Minati showed a higher SERS enhancement of about one order of magnitude compared to spherical nanoparticles of the same seize. Wang et al. produced nanostars under acidic conditions (pH of 5), but required DNA-coated Au spheres as seed particles. The authors reported a SERS activity 15 times larger than spherical structures. Interestingly, the use of different DNA sequences to direct Au reduction enabled highly controllable nanostar geometry. Vo-Dinh et al.[25] developed a hybrid silver(Ag)-coated Au nanostar synthesis using $AgNO_3$ as one of the facet passivation layers. $AgNO_3$ offered control of the branch density and length. The authors' reported SERS brightness in lieu of enhancement with an 11-times increase in signal intensity. While the amount of silver was not reported, the core size, branch length, and number of original Au nanostars dictate the amount of Ag needed for ideal coating. One drawback to this method is impracticality of using Ag for biological application, although SiO_2 coating was introduced to address this issue. However, other nanostars have been synthesized using $AgNO_3$ for facet passivation without depositing Ag metal.[26-27]

While these synthetic approaches generate nanostars with increased enhancement over spherical particles by an order of magnitude, synthetic nanoparticles have drawbacks leading to instability and functionalization challenges. The surfactants used in some syntheses, like cetyltrimethylammonium bromide (CTAB)[28] or polyvinylpyrrolidone (PVP),[29] can inhibit further functionalization. Surfactant-free synthesis improves functionalization but increases the aging rate as shown by the LSPR spectra, limiting

structures to a 5 to 10 h window of use.[24, 30] This is a problem for SERS and biosensing where particle instability leads to aggregation and, ultimately, signal fluctuation and poor reproducibility.[2] An additional concern for many of these syntheses is the low yield.[8] To address these issues, several methods have been developed to generate more robust or insulated nanoparticle sensing systems for complex solution matrices. One approach uses silica capping shells around the synthetic nanoparticle to trap the target analytes and prevent aggregation.[5, 31-32] Another strategy to isolate individual nanoparticles is to completely eliminate aggregation via top-down fabrication. Patterning SERS substrates using top-down fabrication has been the most successful methods to control nanoparticle aggregation, increase nanoparticle yield, and increase reproducibility in spectroscopy applications.[23, 33]

4.1.2 *Top-Down Directed Substrates*

Top-down fabrication designs have been developed with several geometries for arrayed, or "rationally designed," nanostructure surfaces. Though some of these advances are incredibly versatile, the cost is often prohibitive. For example, electron beam lithography has been used to generate stars, bowties, and easily manipulated nanogaps.[10, 34] More economical and, therefore, scalable methods include nanosphere template lithography (NSL). While synthetic strategies are confined to the visible and near IR because large nanoparticles fall out of solution,[24] top-down fabrication can tune the LSPR of nanostructures from the UV to IR.[7, 9, 33, 35-36] Introducing a broad LSPR range makes several additional applications of the plasmonic substrates available, such as sum-frequency generation (SHG) and surface-enhanced infrared absorption (SEIRA) among

others.[33, 37-41] Although top-down fabricated methodologies address problems with defined structure position and reproducibility, nanofabricated structures lack the increased sensitivity that can be attained with synthetic nanoparticles for spectroscopy and sensing.

The push for uniting top-down and bottom-up has been called the "conquest of middle-earth."[42] Designs that bridge the top-down and bottom-up processes to develop novel nanostructure arrays are sought after to reproducibly achieve highly sensitive, aggregation-free substrates for biosensing and SES. The strategies used to develop these hybrid materials fall into two main categories: (i) template driven self-assembly of high-sensitivity synthetic nanoparticles onto patterned features and (ii) nanoparticle positioning by electrostatic or soft-template self-assembly.[42] The electrostatic positioning techniques use chemical modifications on the surface to promote specific adhesion while the soft-template (sacrificial layer) is used to prevent nonspecific binding of nanoparticles.

Several of the electrostatic techniques physically or chemically tether a synthetic nanoparticle to a fabricated nanostructure array. This takes advantage of the coupling between nanoparticle systems to enhance signals for SES via nanogaps or dimerization. Dimerization confines the electric field between two particles, increasing the strength of the optical near-field as compared to a single nanoparticle.[43-44] Nguyen et al. developed a substrate that uses the enhancement created by coupling synthetic nanorods with a fabricated nanotriangle array to impact SERS signal.[45] A thermo-responsive polymer impregnated with synthetic nanorods would expand or shrink characteristically, bringing the nanorods closer to or further from the nanotriangle surface, thus increasing and

decreasing the SERS signal via nanoparticle dimerization. The drawback of this technique is related to lack of reproducibility as the signal varied from substrate to substrate depending on the ratio of nanorod dimers. In another nanoparticle coupling scheme, a hybrid material was constructed by coupling Au nanostars with SERS probes and then introducing the combo to a nanohole array.[46] Using complementary DNA tethers, the nanostars couple to the nanohole generating enhancements up to 4.5×10^6. However, the enhancement from the nanohole array was equivalent to that of a Au film when the nanostars were not ideally placed.

Several creative template driven assemblies use top-down fabrication to isolate nanoparticles. For example, Yang et al. demonstrated the use of a two-step top-down approach to generate nanoparticles in a trench that can be chemically controlled.[40] While not a spectroscopy application, Choi et al. developed an interesting Si-nanowire substrate for semiconductor applications by treating the fabricated nanostructures as seeds for a synthesis.[47] Top-down fabrication was used to etch inverted pyramids in a Si wafer and Au was then deposited over a sacrificial layer and annealed. Annealing the Au allows the nanoparticles to take on a crystalline structure that can serve as faceted seed nanoparticles for Si nanowire growth. Many of these substrates are capable of high-enhancement with interesting geometries but require expensive or several fabrication steps with additional coupling required to adhere the nanoparticle to the macro substrate.

4.1.3 *Overview*

The goal of the research presented here was to develop a hybrid surface-enhanced spectroscopy substrate that uses affordable and simple methods from both top-down and

bottom-up techniques. To avoid using expensive electron-beam lithography or other traditional, time-intensive lithographic techniques, we employed nanosphere lithography (NSL), a simple two-step process of polystyrene nanosphere template deposition and Au evaporation, to generate a well-patterned array of nanotriangles.[48] Using a one-pot synthesis, the nanostructure array acted as the seed, or "host," for a nanostar-based synthesis that does not require any additional purification beyond rinsing the solid substrate. The combination of these two techniques generates fixed substrates with branched decorations, or "nanomites."

The synthetic, branched decorations are referred to as "nanomites" due to the biological parallel to the growth response of leaves to various mites and insects. When leaves are bitten by a mite, the damage causes the leaf to produce hormones leading to localized growth of a gall (excess leaf tissue) that encloses the mite (Figure 4.1). Much like a tree mite, the synthetic nanomite does not change the underlying structure or impact the host negatively. Nanomites can be synthesized regardless of host nanostructure shape or optical properties, as will be shown in the Chapter 5.

Figure 4.1 Gall growth on a leaf in response to mite damage.

4.2 Materials and Methods

4.2.1 *Materials*

Gold pellets were purchased from K.J. Lesker (Clairton, PA). Glass substrates of BK7 glass microscope slides were purchased from Ted Pella, Inc. (Redding, CA). Various sizes of Aldehyde/Sulfate Latex Beads, 4% w/v, were purchased from Life Sciences Solutions, Inc. (Grand Island, NY). Absolute ethanol was purchased from Pharmco-Aaper. Concentrated H_2SO_4 and 30 wt % NaOH were purchased from EMD Chemicals. Concentrated HCl, and 30% H_2O_2, ethanolamine ($\geq$ 98%), and $HAuCl_4$ were purchased from Sigma-Aldrich. $AgNO_3$ was purchased from Fischer Chemical. 4-(2-hydroxyethyl)-1-piperazineethanesulfonic acid) (HEPES) buffer was purchased from Gold Biotechnology company. Nanopure water (18 mΩ) (Barnstead NANOpure Diamond) was used to prep all solutions and glassware.

4.2.2 *Substrate Preparation*

Glass microscope slides were cut into 1” x 1” sections and cleaned by immersion in piranha acid (3:1 volumetric ratio of H_2SO_4:30 % H_2O_2) for 45 min. (Caution: piranha acid is a strong oxidizer and has been known to detonate upon contact with organic material.) The substrates were rinsed three times with nanopure water and transferred to a 60 °C detergent bath (5:1:1 volumetric ratio of H_2O, NH_4OH: 30 % H_2O_2) for 60 min under sonication. Slides were rinsed three times with nanopure water, rinsed with isopropanol, dried with N_2 and used within one week.

4.2.3 *Nanotriangle Fabrication*

Nanosphere lithography was used to fabricate the nanotriangles and has been described previously.[36, 49-50] Sulfate/aldehyde functionalized polystyrene nanospheres were closed-packed onto the glass slides using a similar method to Weiss et al.[51] To close-pack, the substrates were submerged in nanopure water and a 50/50 solution of nanosphere:ethanol was introduced to the air-water interface via a syringe pump (0.150 mL/min) until a monolayer formed. The water was then removed by pump (0.30 mL/min), allowing the template monolayer to deposit on to the substrate. To fabricate nanotriangles, the nanosphere templated substrates were mounted normal with respect to the source in an electron-beam evaporator chamber (Denton SJ20C Vacuum USA, Moorestown, NJ). A 3 nm chromium adhesion layer was deposited (1 Å/s) followed by 30 nm Au film (1 Å/s), as measured by a quartz crystal microbalance (XPC2 Inficon, East Syracuse, NY) under high vacuum (2.0×10^{-6} Torr). Refer to Figure 1.3A for a schematic representation of nanotriangle fabrication. The polystyrene templates were removed by lift-off using transparent tape and samples were stored under nitrogen.

4.2.4 *Nanomite Synthesis*

Fabricated Au nanotriangles (AuNT) substrates were cut into 2.5 cm x 0.8 cm (1/3 slide), treated with 5 min of ultraviolet-ozone (Jelight 342, Irvine CA), and placed into individual 20 mL beakers. To generate nanomit+e decorations on the host AuNT substrate, 3.4mL of 1.20 mM HAuCl4, 0.020 mL of 1M HCl, and 1.0 ml of 100 mM 4-(2-hydroxyethyl)-1-piperazineethanesulfonic acid) (HEPES) (pH adjusted to 6.9) were combined with the host substrate and placed on an orbital shaker table (SK-D1087-S

Digital 3D Gyratory Rocker Scilogex, City, State) at 10 RPM. Next, 0.220 mL of a 1.5 M $AgNO_3$ and 0.110 mL of ethanolamine, were simultaneously added to the solution. After 10 s on the orbital shaker, the solution was placed in an ice bath (5 °C) for 1 h (nucleation phase) and brought to 20 °C for 1 h (growth phase). Next, the solid substrate was rinsed with DI water and ethanol, before being dried with N_2. Solutions were stored at 4 °C to ensure that low temperature nucleation conditions were uniform.

4.2.5 *Instrumentation*

The optical properties of the NM@NT were characterized by transmission ultraviolet (UV)/visible spectroscopy. Extinction spectra were collected with a Perkin-Elmer Lambda 750 UV/vis spectrophotometer. The λ_{max} was determined using Spectrum

The nanomite synthesis uses a slow nucleation phase followed by a room temperature growth phase (

software and the center of gravity function. Scanning electron microscopy (SEM) (FEI NovaNano 630 equipped with a Helix detector) was used to the structure of the AuNTs before and after synthesis.

4.3 Results and Discussion

Scheme 4.1). The host nanostructure is fabricated using nanosphere lithography and the synthetic routine is a simple one-pot synthesis carried out at 4 ºC for 1 h to allow the Au (III) solution to nucleate onto the fabricated Au surface. Once ample time has been allowed for nucleation, the solution is brought to room temperature and the structures grow in length via the further reduction of Au (III)

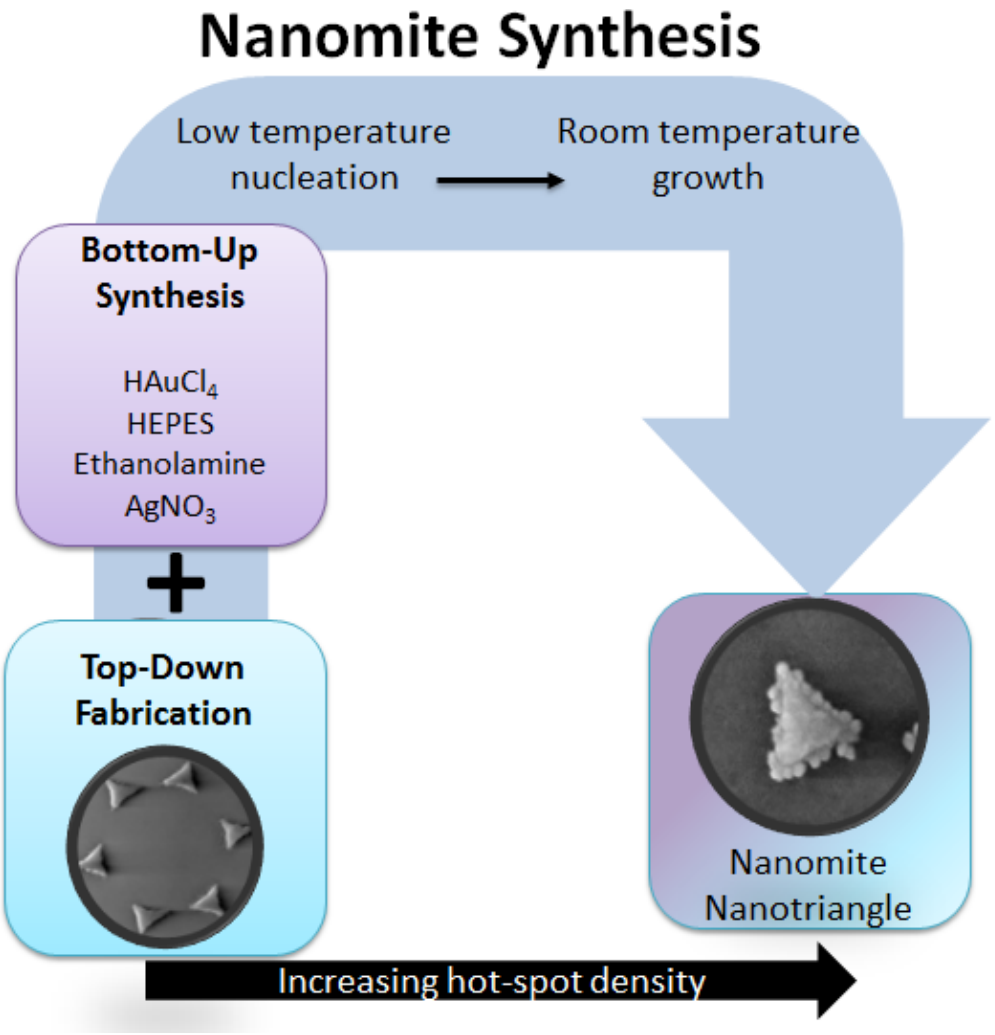

Scheme 4.1 Overview of nanomite synthesis using a low temperature nucleation and room temperature growth phases to decorate fabricated nanostructures with synthetic nanomite decorations.

on the now established facets of the decorations. The generated structure is a nanotriangle (NT) with nanomite (NM) decorations (NM@NT). Decoration refers to the growth of any material on the host nanoparticle whereas nanomite refers to some degree of branching. Initial methodology used a variety of colloidal lithography techniques to fabricate host structures. To align with the project goal of scalability, AuNTs were chosen as the principal host. AuNT are the least time-intensive structure to fabricate and plasmon resonances in the visible and near-infrared (NIR) for SERS and LSPR biosensing are easily attained.

The first hurdle in using top-down fabricated nanostructures as hosts for synthesis is the lack of inherent crystal orientation of the metal to produce specific sites to chemically direct growth of the nanomite branches. The AuNTs fabricated via NSL use electron beam (e-beam) evaporation to deposit a Au film over the nanospheres. With e-beam evaporation of Au, the crystal boundaries are typically small, heterogeneous with no clear crystal orientation or large domains.[52] Using high-resolution transmission electron microscopy (HRTEM), the facet heterogeneity of the AuNT structure is shown (Figure 4.2). The lack of crystallinity complicates the use of the evaporated metal as a seed for nanoparticle growth because the growth of a nanoparticle in a synthetic routine is governed by facet passivation, and large crystalline facets are not the typical result of tens of nanometer thick electron-beam deposition. One way to introduce crystallinity to evaporated metals is by annealing under high temperature and cooling the metal slowly, as shown by Choi et al. with the nanowire synthesis.[48, 53-54] In the case of NSL, the nanostructures have defined positions and shapes that would be compromised by high heat. Therefore, the growth of nanoparticles on the fabricated nanostructures must be

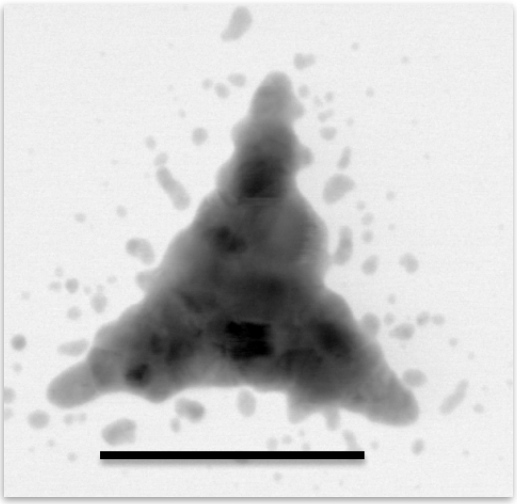

Figure 4.2 HRTEM image of AuNT. Scale bar is 100 nm. Imaging by Arthur Quast.

driven by surface chemistry and not by some physical means like annealing.

Initially, the strategy for the nanomite synthesis was based on a method developed by Vo Dinh for nanostars.[45] The synthesis used chloroauric acid ($HAuCl_4$) as a source for Au, ascorbic acid to reduce the Au(III) and act as a capping agent, and silver nitrate ($AgNO_3$) to control the branch density and length. It has been proposed that the Ag ion-induced nanostar growth can be attributed to the underpotential deposition and increasing the concentration of silver ion in the solution stabilizes more open surface facets.[10, 55-56] Initial experiments using these three reactants ($HAuCl_4$, $AgNO_3$, and ascorbic acid) on nanorings lacked reproducibility and any given synthesis would produce 10-100% decoration, based on SEM imaging, in a variety of shapes (Figure 4.3).

It was then determined that the ascorbic acid did little to affect the initial "nucleation" of the decorations. Citrate, another reducing agent, was incorporated, but also lacked reproducibility (data not shown). In fact, the decorations generated for syntheses with and without citrate or ascorbic acid were nearly identical and, as a result,

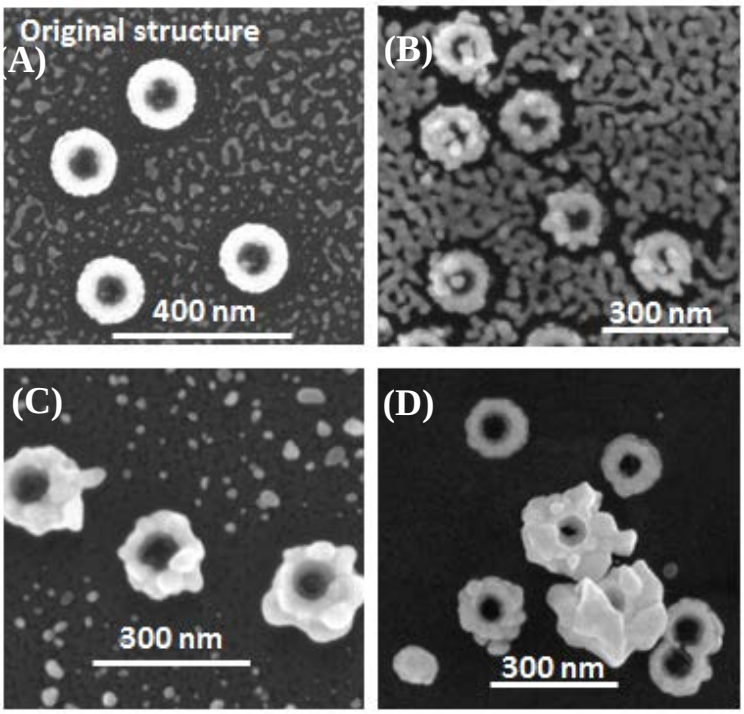

Figure 4.3 Initial nanomite structures using nanorings as the host for the reduction of Au with 1.9 mM $HAuCl_4$, 3 mM $AgNO_3$, 100 mM ascorbic acid: (A) original host structure; (B) doubled volume of $HAuCl_4$; (C) and (D) are duplicate experiments using 5 mL $HAuCl_4$, 100 μL $AgNO_3$, and 50 μL ascorbic acid. Reactions were limited to 10 min.

these capping agents were removed from the synthesis protocol.

A more aggressive capping agent was then introduced, as the surface of the host nanoparticles were thought to be too stable. Ethanolamine and other complex amine molecules have been established as successful reducing/capping agents for branched nanoparticles, although the mechanism of formation remains unknown.[1] By introducing hydroxylamine and ethanolamine reducing and capping agents iteratively, the decorations produced from the nanomite synthesis became more reproducible, though not highly branched. The addition of ethanolamine produced structures that exhibited large, uniform growth but lacked branching or roughening of the surface (data not shown). However, the uniformity and increased absolute growth of the nanostructures with the new nanomite

synthetic scheme using ethanolamine was promising. The increase in nanostructure size strongly indicated that the ethanolamine had sufficient affinity for the host Au nanoparticles to induce reduction of Au (III) onto the host structure. The focus then turned to encouraging facet passivation so that the nanoparticle growth could be directed into the branched shape.

To encourage branching of the Au structures, another reducing agent was introduced simultaneous to the ethanolamine. It has been previously shown that the piperazine ring in 4-(2-hydroxyethyl)-1-piperazineethanesulfonic acid) (HEPES) buffer can generate nitrogen-centered free radicals capable of reducing Au ions.[57] Further work by Xie et al. introduced a seedless, branched nanoparticle synthesis based on HEPES buffer.[58] In the nanomite synthesis, introduction of HEPES dramatically increased the branching of the Au growth on the fabricated nanocrescents (Figure 4.4). It has been reported that the piperazine ring preferentially binds on the different Au facets but most weakly on the (111) planes, thereby Au grows along the (111) direction.[59-60] By achieving reproducible decorations with HEPES buffer, the nanomite synthesis could be

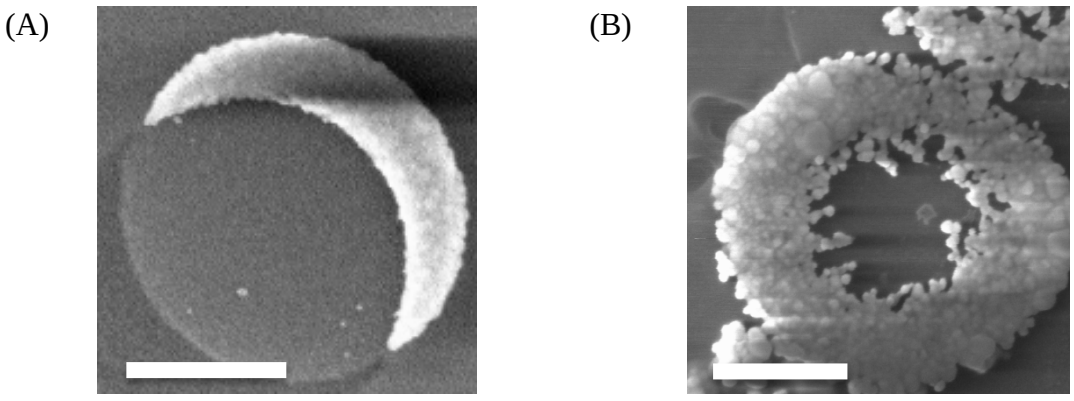

Figure 4.4 Room temperature reaction of a NM@NC synthesis (A) without HEPES and (B) with HEPES buffer (1 mM at pH 7.5). Reactants include $HAuCl_4$, NaI, HCl, $AgNO_3$, and ethanolamine. Scale bar is 500 nm.

further optimized by controlling a variety of parameters. Nanomite syntheses, like the solution based nanostars, are strongly controlled by the local dielectric environment and small changes in temperature, pH, or reactant ratios can have significant effects on reproducibility and branch growth. The following experiments demonstrate the optimization of branched nanoparticles with fabricated arrays of AuNTs.

4.3.1 *Growth Characterization: Temperature*

Temperature is used to control the nucleation and growth kinetics of nanoparticles. Generally, lower temperatures encourage nucleation and increase LSPR reproducibility and higher temperatures encourage rapid growth but decrease LSPR reproducibility.[61-62] In compromise of LSPR reproducibility and synthesis time, a low temperature nucleation period was introduced followed by a room temperature growth period. Figure 4.5 shows the structural changes of NM@NTs over the course of a 1 h nucleation phase at low temperature (4 °C) and a 1 h growth phase at room temperature

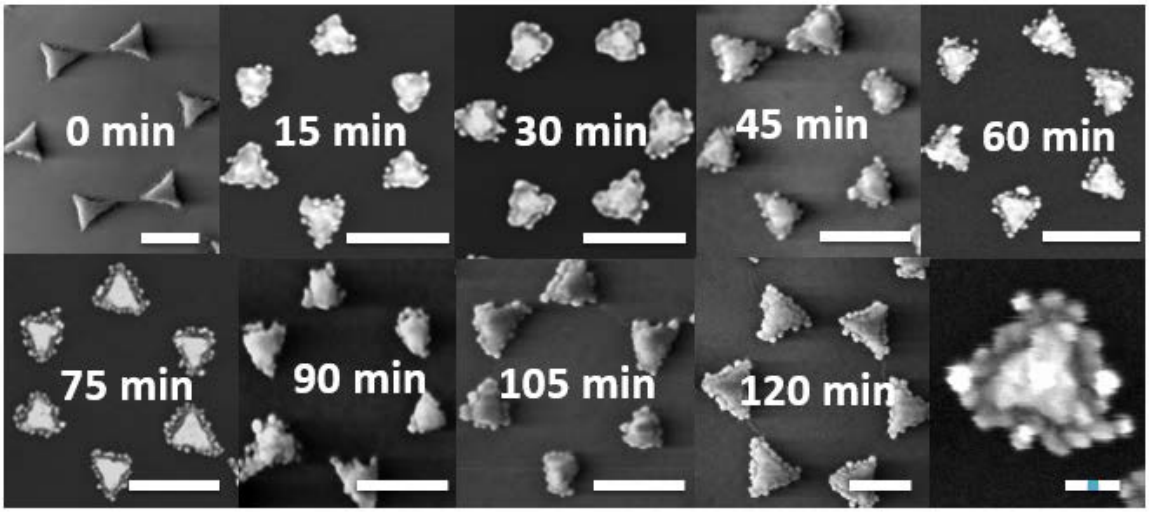

Figure 4.5 SEM of NM@NT over (TOP) the first hour of nucleation (4 °C) and (BOTTOM) second hour of growth (20 °C). Scale bars are 200 nm for time trials and 50 nm for the close up (bottom-right) with 10 nm subscale bar in blue.

(20 °C). Figure 4.6A shows the spectra of the NM@NT over the same nucleation and growth period collected during the synthesis. The inset of Figure 4.6A shows the spectra of the reaction solution and NM@NT after 120 min. By identifying the LSPR peak of the substrate and the LSPR peak of the solution independently after synthesis (inset Figure 4.6A), the two predominant peaks at ~590 nm and 750 nm are attributed to the solution (λ_{soln}) and the solid substrate ($\lambda_{NM@NT}$), respectively. Tracking the relative LSPR shift of the two main peaks (Figure 4.6 B) allows the growth rates for the solution and the substrate to be extracted independently.

During the nucleation phase, the substrate does not experience a large amount of growth as evidenced by the near 0 nm/min LSPR shift; however, the nucleation of Au is clear in SEM images (Figure 4.5, top row). There are several situations that could explain the deposition of Au in the SEM images without the clear LSPR shift that would be expected for adsorption of material on the AuNT surface. The bulk solution at the start of the synethesis has a high concentration of all reactants, so adsorption of directly attached $AgNO_3$, HEPES, or ethanolamine could be masked in the bulk, high refractive index of the solution. Alternatively, the nucleation is not generating sharp tips or branched structures, so the sensitivity of the structures for changes is not uniquely high. The third option relies on evidence from preceding experiments at room temperature in the absence of HEPES. Previously, etching of the host nanostructure would occur as evidenced by SEM images *without* deposition of decorations. It is possible that the synthesis is “etching” or dissolving some components of the host structure and redeposition is occurring simultaneously.

(A)

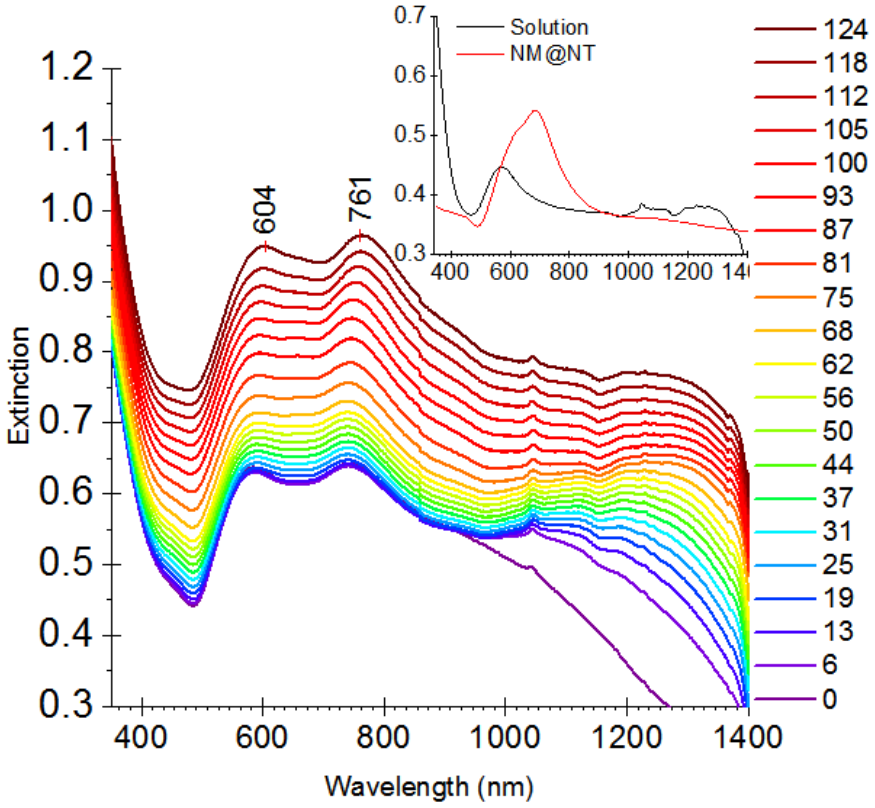

(B)

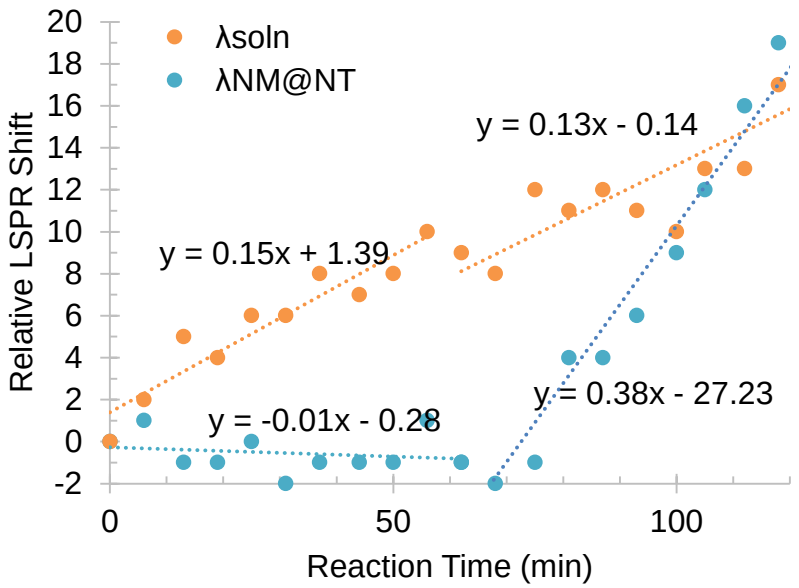

Figure 4.6 (A) Extinction spectra of 330 nm template NM@NT from 0 to 120 min collected in 6 min intervals. At 60 min, the samples are switched from 4 °C nucleation to 20 °C growth by removal from an ice bath. Inset spectra are from the NM@NT substrate after synthesis and the reaction solution. (B) Relative LSPR shift of the peaks centered at 590 and 750 nm for 330 nm template NM@NT. Trend lines correspond to the separate nucleation (0-60 min at 4 °C) and growth (60-120 min at 20 °C) phases of the nanoparticle synthesis.

During the room temperature growth phase, the rate of growth increases (as marked by the rate of $\lambda_{NM@NT}$ shift) from ~0 nm /min to 0.38 nm/min. The SEM images of 60 min to 75 min NM@NT are similar with fine decorations, likely due to the solution not yet coming to room temperature. Between 90 min and 120 min, the NM@NT increase in size with separation of branch features as shown in the close-up (Figure 4.5, bottom right). The structures at 120 min are more uniform in appearance around each AuNT as compared to that of the 15 min NM@NT, which have more sporadic decoration. Over the same temperature range, the λ_{soln} of the extraneous nanoparticles in solution shift at a rate of 0.13 nm/min (4 °C) to a rate of 0.15 nm/min (20 °C), indicating that the growth of the suspended nanoparticles is not changing. This could be due to increased competition of reactants by the NM@NT substrate (discussed below).

The separation of nucleation and growth is in sharp contrast to that of NM@NT prepared in room temperature (25 °C) and at elevated temperature (60 °C) (Figure 4.7). At 25 °C, neither λ_{soln} nor the $\lambda_{NM@NT}$ demonstrated linear growth (Figure 4.7C). The $\lambda_{NM@NT}$ for the 25 °C slowly blue-shifted before red-shifting at about 90 min (Figure 4.7C), possibly due to tip rounding and/or dissolution of the AuNT host. A similar shifting pattern is demonstrated by the λ_{soln}. The λ_{soln} peak becomes stronger throughout the synthesis, starting as a shoulder off of the ~700 nm peak until 50 min were the LSPR peak for the solution becomes strong enough for wavelength assignment. The red-shift of the $\lambda_{NM@NT}$ at 90 min could be due to the increase in size of the NM@NT or a response to the refractive index change generated by the growth of nanoparticles in solution. The refractive index change is supported by the $\Delta\lambda_{soln}$, which did not grow into the spectra until 50 min. The morphology of the nanoparticles varied in two replicate

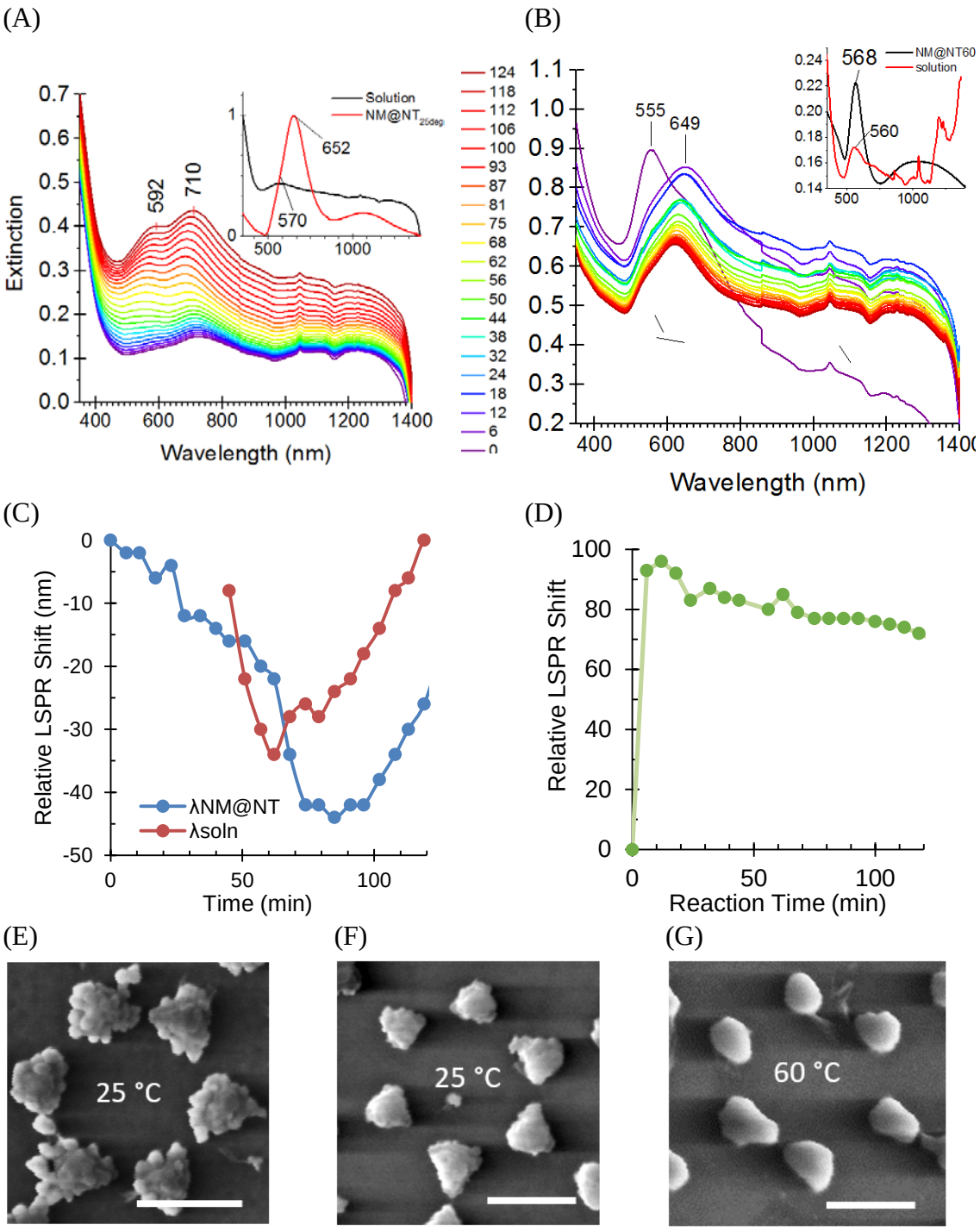

Figure 4.7 Extinction spectra taken every 6 min during the NM@NT synthesis at (A) 25 °C and (B) 60 °C. The relative LSPR shift of the (C) λ_{soln} and $\lambda_{NM@NT}$ for 25 °C nucleation/growth (D) $\lambda_{NM@NT}$ for 60 °C nucleation/growth. SEM images of NM@NT variations at (E and F) 25 °C and (G) 60 °C. Scale bars are 200 nm.

syntheses (Figure 4.7 E and F). It is likely that the increased temperature makes minor differences in timing less forgiving. Because the kinetics of reaction are occurring at a faster rate at higher temperatures, the timing of reactant introduction impacts the structure morphology. In some cases, this generates overgrowth of the NM decorations with branches ranging in diameter from 30-40 nm (Figure 4.7E). In other cases, there is very little branching (Figure 4.7F).

The 60 °C synthesis generates structures with no branching (Figure 4.7G). The spectrum of the synthesis at 60 ºC shows that there is a large initial growth within the first 6 min of the synthesis, as shown by the peak shift from 547 nm to 640 nm followed by a small blue-shifting throughout the 2 h window (Figure 4.7D). The asymmetric peak at 649 nm is composed of the substrate (the dominate peak) and a shoulder from the solution. Due to the overlap, the $\Delta\lambda_{soln}$ could not be independently tracked. The preferential growth of branches at room temperature has been reported by others and Burrows et al. has shown that by using low-temperature synthesis (5 °C), the LSPR reproducibility of the structures increases dramatically.[60, 63]

The heterogeneous growth (growth using an existing interface such as the fabricated host nanostructure) is determined by long-range atomic diffusion and the growth is thermally activated in an Arrhenius relationship.[62] For this reason, the solution is brought to room temperature after the initial nucleation phase. The nucleation phase is necessary to compensate for the competition between the NM synthesis and the solution synthesis (byproduct). Because the fabricated host structures have variable-size physical boundaries from step edges, grain sizes, surface roughness and so forth, lowering the temperature of the reaction allows for nucleation at a larger population of these

boundaries. Nucleation theory states that as the temperature of a solution decreases, the volume free energy of nucleation becomes more negative, allowing the formation of a stable nucleus at a smaller radius as well as making the growth more favorable.[61]

The number of stable nuclei, nuclei that are greater in size than the critical radius required for nucleation, is also a function of temperature. As temperature is lowered, the number of stable nuclei increases. In short, by lowering the temperature of the solution, the host nanostructures are more accessible for nucleation. Once the nucleation occurs, the substrate can compete more effectively for reactants to generate the larger decorated structures. This proves an effective format given that the $\lambda_{NM@NT}$ shifts at double the rate of the solution, suggesting two possibilities: (1) the NM@NT substrate is more sensitive to the increase in size making the shift greater in magnitude, and/or (2) the NM@NT substrate is growing at a greater rate than the particles in solution.

4.3.2 *Elemental Composition*

$AgNO_3$ is used to control branching of Au decorations but is also a component in Ag deposition on Au nanoparticles. Vo-Dinh et al. demonstrated that in the absence of $HAuCl_4$, $AgNO_3$ is reduced by ascorbic acid in basic conditions to deposit a Ag shell around Au nanoparticles.[25] While the authors did not report the pH of this reaction, the nanomite synthesis could possibly induce Ag metal deposition due to the basic conditions (pH 10) and potential excess of reagents.

To confirm that the branches formed in the nanomite synthesis are Au and *not* Ag, electron dispersive spectroscopy (EDS) was used to confirm the elemental composition of the substrates using full frame scans that cover 25 μm^2 as well as spot scans at the

center and the edge of NM@NT. A representative EDS spectrum is shown in Figure 4.8 with the positions for Au and Ag are highlighted. The large peak at 1.74 keV corresponds to the Si wafer substrate and the peak at 2.12 KeV denotes Au. The spectrum lacks the 2.98 keV peak which would signify Ag. Both full frame scans and spot scans on NM@NT structures supported the use of Au as the only component in the decoration growth. However, with excess $AgNO_3$ or absence of $HAuCl_4$, the possibility of Ag deposition Au is possible.[25, 50] The role of Ag ions will be discussed in more detail in Section 4.3.4.

4.3.3 *Effect of pH on Two Reducing Agents*

The structures of the two reducing agents are shown in Figure 4.9. HEPES buffer has two pka points; $pK_{a1} = 3$ and $pK_{a2} = 7.5$. Ethanolamine has a $pK_a = 9.5$. When the pH of the reaction solution is below the pK_a, the amine group will be protonated. At pH

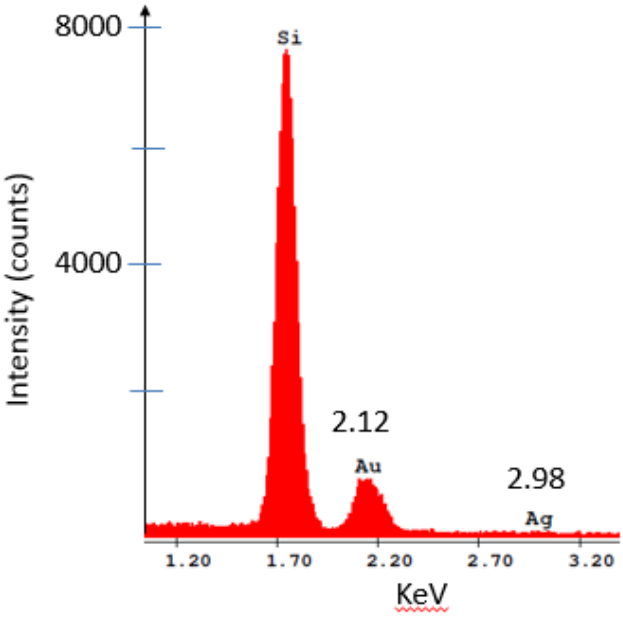

Figure 4.8 EDS spectrum of NM@NT.

(A) (B)

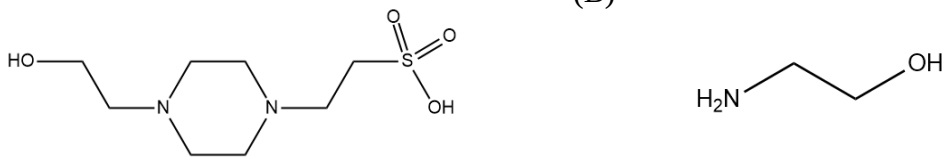

Figure 4.9 Reducing/capping agents: (A) HEPES buffer and (B) ethanolamine.

above the pK_a, the amine group will be deprotonated. The standard nanomite synthesis has a pH of 10.5, which is close to the range that Minati found metallic Au was required for the autocatalytic growth of nanostars.[64] However, in the absence of ethanolamine and HCl, the nanomite reaction solution takes a blue color indicative of nanostar growth in solution at a pH of 6.4.[65] In addition to the nucleation on the host structures (bottom-left inset Figure 4.10A), nanostars form in the solution (top-right inset Figure 4.10A).

The NM@NT structures that formed under these conditions (pH 6.5), are distinctly different than those formed under the standard conditions (pH 10.5) as described in the synthesis protocol (Figure 4.10B and C). The nanostars synthesized as a byproduct in the NM reaction are large (100+ nm) with up to 40 nm long branches that range in width from 5-10 nm and have an LSPR of 680 nm. While not the target structure, these nanostars are much larger than those produced by others, while also being stable in solution for 3 weeks, unlike some synthesized nanostars that are stable for up to 10 h.[24, 30] Further studies into the effect of pH in the absence and presence of ethanolamine and host nanoparticles will be required to determine the mechanism of HEPES reduction as well as the role of ethanolamine. This will be discussed in Chapter 6.

(A)

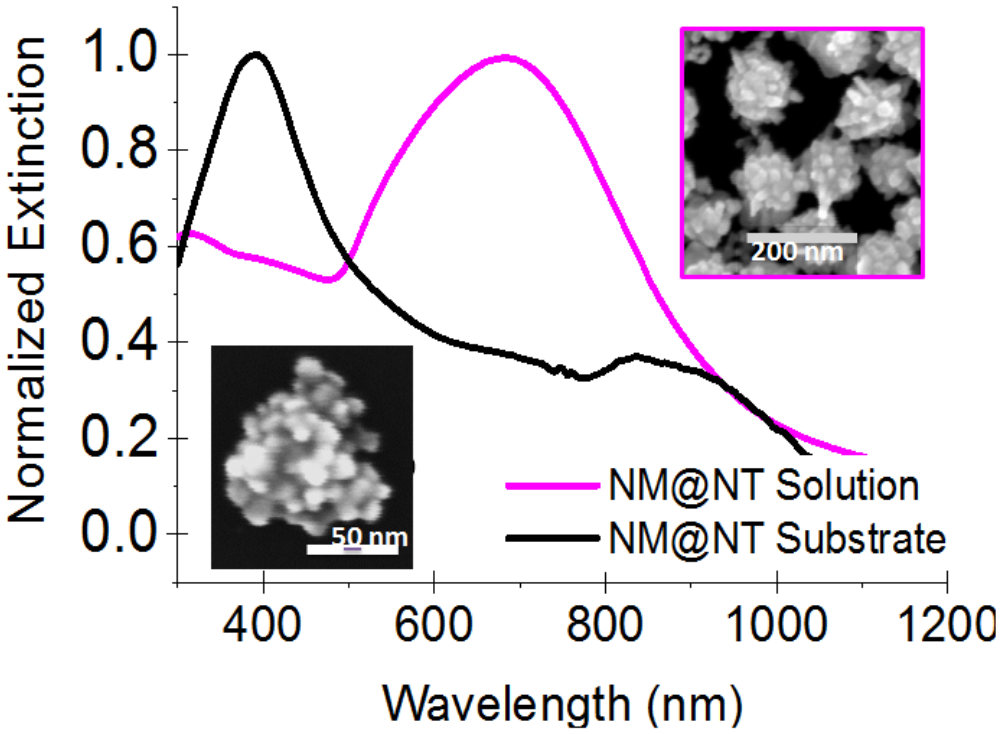

(B)

(C)

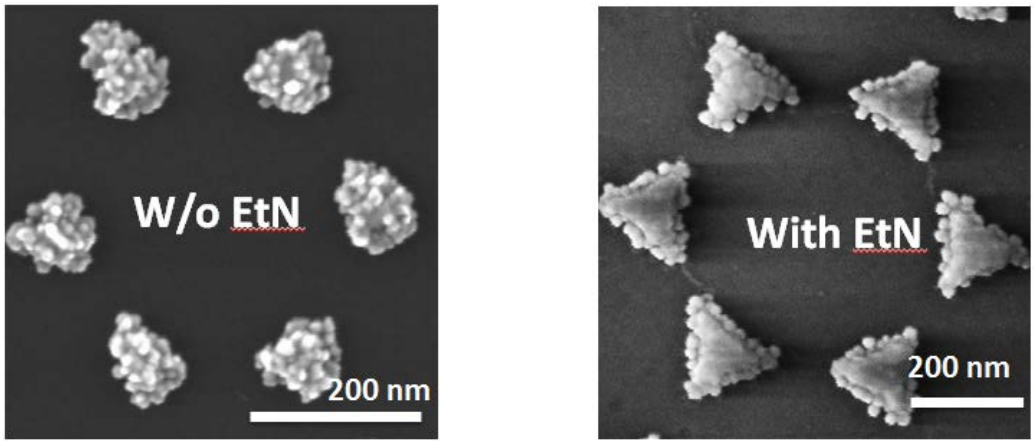

Figure 4.10 (A) Extinction spectra of nanostar solution (pink) and NM@NT under reaction conditions (pH = 6.5) that exclude ethanolamine and HCl. The rop right inset are nanostars formed in solution and the bottom left inset are the NM@NT structures. Scale bar is 200 nm for the nanostars and 50 nm for the NM@NT. Side by side comparison of the impact of (B) no ethanolamine or (pH= 6.5) and (C) with ethanolamine (pH=10) on the structure of the NM decorations. Scale bars are 200 nm.

4.3.4 *Silver Underpotential Deposition Control*

The controlled used of halides and silver ions has been used to generate a wide-variety of structures via the manipulation of the Ag^+ underpotential deposition (Ag_{UPD}) on Au via the reduction of a submonolayer of Ag^+ on the Au surface. While the introduction of salts into typical nanostar synthesis causes the nanostars to aggregate and crash out of solution,[66] the stationary host nanoparticles prevent such aggregation issues making the introduction of halides a nonissue. As a result, the impact of iodide can be investigated relative to the $AgNO_3$.

Bromide and iodide induce a destabilization of the Ag_{UPD} layer with iodide being the stronger destabilizer. In small concentrations, the presence of these ions slows the rate of Au reduction, but in large volumes potentially increases the rate of reduction.[26] Figure 4.11A shows the spectra of two NM@NT syntheses with and without high molar amounts of iodide. The blue-shifted max LSPR peak (λ_{max}) of the NM@NT in the

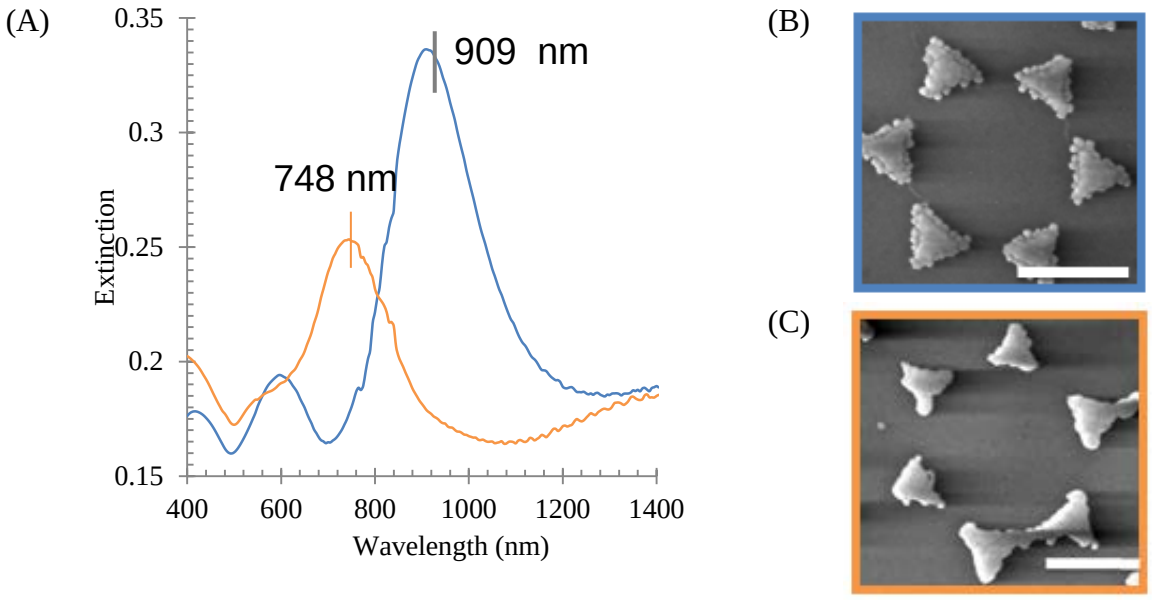

Figure 4.11 Comparison of the presence of iodide as a control for silver underpotential: (A) Extinction spectra of NM@NT in the presence of 1.20 ml of 10 mM NaI (orange) and without NaI (blue); (B) SEM image of NM@NT with no iodide; (C) NM@NT in the presence of iodide. Scale bars are 300 nm.

presence of iodide indicates that the reaction rate was slowed or strongly inhibited. Figure 4.11B and C compare the physical structures of the NM@NT and it is clear that iodide produces amorphous and inconsistent decorations.

The destabilization caused by the concentrated halides increases the mobility of the Ag_{UPD} and Mirkin et al.[67] showed that the Ag_{UPD} layer mobility increases in the presence of trace levels of iodide, stabilizing the high-index surface. When using very high concentrations of iodide, these can lead to extremely stellated features (no clear facets). This is caused by preferential binding of iodide to the Au surface which displaces and destabilizes the Ag_{UPD}.

Another method to direct Au growth on specific facets is to manipulate the Ag_{UPD} is based on concentration. For NM@NT, doubling the Ag^+ concentration drastically increased the overall size and branching of the nanoparticles (Figure 4.12). Personick and Mirkin et al.[63] showed how the use of varying Ag^+ concentrations can stabilize the (110), (310), and (720) of Au to form octahedral with (111) facets, rhombic

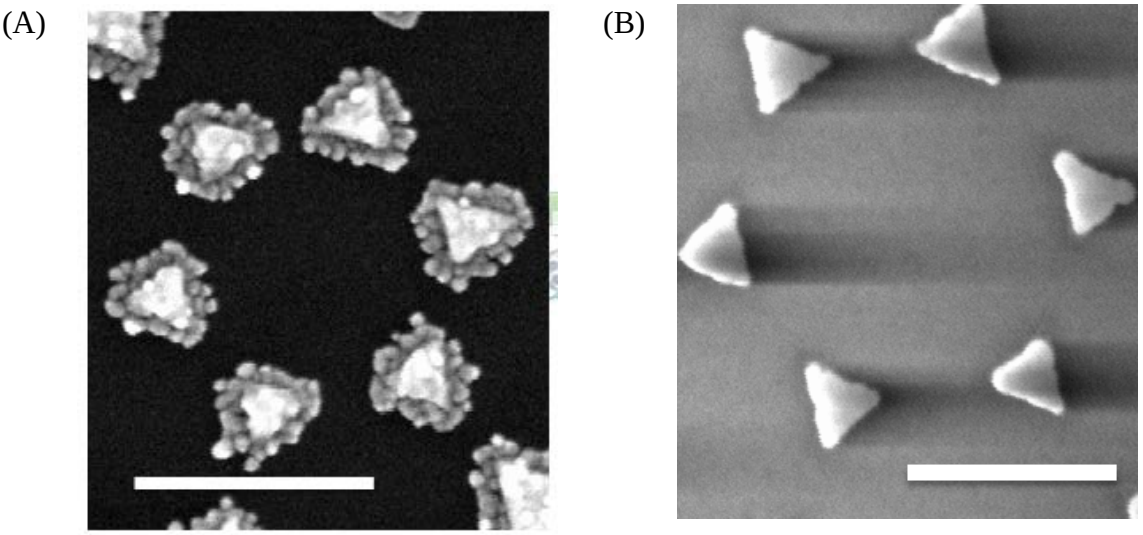

Figure 4.12 $AgNO_3$ concentration dependence on NM@NT morphology: (A) 0.220 mL of 1.5 M $AgNO_3$; (B) 0.110 mL of 1.5 M $AgNO_3$. Scale bars are 300 nm.

dodecahedra with (110) facets, truncated ditetragonal prisms with (310) facets, and concave cubes with (720) facets. The authors use Ag^{+}/Au^{3+} ratio of 1:500 to 1:5 to selectively hinder the deposition of Au on to a selected facet; higher Ag_{UPD} coverage is necessary to stabilize a higher energy surface facet that is more reactive to Au deposition. This translates to a more open and higher-index surface being stabilized. On the NM@NT, the effect of increasing Ag^{+} to stabilize high energy facets is closely related to the random facets on the surface of the fabricated nanostructure. As discussed earlier, the Au is evaporated onto the substrate by e-beam evaporation, resulting in the a combination of heterogeneous facets, some of which may have high energy. Therefore, increased Ag^{+} provides access to these facets for growth.

4.4 Conclusion

Using two simple methods from top-down fabrication and one-pot synthesis, we demonstrate the formation of branched decorations, or nanomites, on fabricated structures. By lowering the temperature and changing the Ag_{UPD}, we create reaction conditions that allow for the reduction of Au (III) onto noncrystalline host nanoparticles. This synthetic strategy can be applied to different fabricated structures, as will be discussed next chapter, increasing the hot spot density and thereby increasing the structure sensitivity to refractive index changes and providing enhancement for SERS signals.

4.5 References

1. Moskovits, M. Surface-Enhanced Spectroscopy. *Rev. Mod. Phys.* **1985,** *57* (3), 783-826.

2. Bantz, K. C.; Meyer, A. F.; Wittenberg, N. J.; Im, H.; Kurtulus, O.; Lee, S. H.; Lindquist, N. C.; Oh, S.-H.; Haynes, C. L. Recent Progress in Sers Biosensing. *PCCP* **2011,** *13* (24), 11551-11567.

3. Khoury, C. G.; Vo-Dinh, T. Gold Nanostars for Surface-Enhanced Raman Scattering: Synthesis, Characterization and Optimization. *J. Phys. Chem. C* **2008,** *112* (48), 18849-18859.

4. Hsiangkuo, Y.; Christopher, G. K.; Hanjun, H.; Christy, M. W.; Gerald, A. G.; Tuan, V.-D. Gold Nanostars: Surfactant-Free Snthesis, 3d Modelling, and Two-Photon Photoluminescence Imaging. *Nanotechnology* **2012,** *23* (7), 075102.

5. Ming, L.; Scott, K. C.; Jianming, Z.; Jessica, L.; Zoraida, P. A.; Dongling, M.; Nianqiang, W. Shape-Dependent Surface-Enhanced Raman Scattering in Gold–Raman-Probe–Silica Sandwiched Nanoparticles for Biocompatible Applications. *Nanotechnology* **2012,** *23* (11), 115501.

6. Pallavicini, P.; Dona, A.; Taglietti, A.; Minzioni, P.; Patrini, M.; Dacarro, G.; Chirico, G.; Sironi, L.; Bloise, N.; Visai, L.; Scarabelli, L. Self-Assembled Monolayers of Gold Nanostars: A Convenient Tool for near-Ir Photothermal Biofilm Eradication. *Chem. Commun.* **2014,** *50* (16), 1969-1971.

7. Fales, A. M.; Yuan, H.; Vo-Dinh, T. Development of Hybrid Silver-Coated Gold Nanostars for Nonaggregated Surface-Enhanced Raman Scattering. *J. Phys. Chem. C* **2014,** *118* (7), 3708-3715.

8. Indrasekara, A. S. D. S.; Meyers, S.; Shubeita, S.; Feldman, L. C.; Gustafsson, T.; Fabris, L. Gold Nanostar Substrates for Sers-Based Chemical Sensing in the Femtomolar Regime. *Nanoscale* **2014**.

9. Fales, A. M.; Vo-Dinh, T. Silver Embedded Nanostars for Sers with Internal Reference (Sensir). *J. Mater. Chem. C* **2015,** *3* (28), 7319-7324.

10. Soares, L.; Csaki, A.; Jatschka, J.; Fritzsche, W.; Flores, O.; Franco, R.; Pereira, E. Localized Surface Plasmon Resonance (Lspr) Biosensing Using Gold Nanotriangles: Detection of DNA Hybridization Events at Room Temperature. *Analyst* **2014,** *139* (19), 4964-4973.

11. Doria, G.; Conde, J.; Veigas, B.; Giestas, L.; Almeida, C.; Assunção, M.; Rosa, J.; Baptista, P. V. Noble Metal Nanoparticles for Biosensing Applications. *Sensors* **2012,** *12* (2), 1657.

12. Raphael, M. P.; Christodoulides, J. A.; Mulvaney, S. P.; Miller, M. M.; Long, J. P.; Byers, J. M. A New Methodology for Quantitative Lspr Biosensing and Imaging. *Anal. Chem.* **2011,** *84* (3), 1367-1373.

13. He, X.; Wang, K.; Cheng, Z. In Vivo near-Infrared Fluorescence Imaging of Cancer with Nanoparticle-Based Probes. *Wiley Interdiscip. Rev. Nanomed.*

Nanobiotechnol. **2010,** *2* (4), 349-366.

14. Aizpurua, J.; Hanarp, P.; Sutherland, D. S.; Käll, M.; Bryant, G. W.; García de Abajo, F. J. Optical Properties of Gold Nanorings. *Phys. Rev. Lett.* **2003,** *90* (5), 057401.

15. Hanarp, P.; Käll, M.; Sutherland, D. S. Optical Properties of Short Range Ordered Arrays of Nanometer Gold Disks Prepared by Colloidal Lithography. *J. Phys. Chem. B* **2003,** *107* (24), 5768-5772.

16. Fahmi, A.; D'Aleo, A.; Williams, R. M.; De Cola, L.; Gindy, N.; Voegtle, F. Converting Self-Assembled Gold Nanoparticle/Dendrimer Nanodroplets into Horseshoe-Like Nanostructures by Thermal Annealing. *Langmuir* **2007,** *23* (14), 7831-7835.

17. Kahl, M.; Voges, E.; Kostrewa, S.; Viets, C.; Hill, W. Periodically Structured Metallic Substrates for Sers. *Sensor. Actuat. B: Chem.* **1998,** *51* (1–3), 285-291.

18. Kennedy, B. J.; Spaeth, S.; Dickey, M.; Carron, K. T. Determination of the Distance Dependence and Experimental Effects for Modified Sers Substrates Based on Self-Assembled Monolayers Formed Using Alkanethiols. *J. Phys. Chem. B* **1999,** *103* (18), 3640-3646.

19. Jana, N. R.; Gearheart, L.; Murphy, C. J. Wet Chemical Synthesis of High Aspect Ratio Cylindrical Gold Nanorods. *J. Phys. Chem. B* **2001,** *105* (19), 4065-4067.

20. Dutta, S.; Ray, C.; Sasmal, A. K.; Negishi, Y.; Pal, T. Fabrication of Dog-Bone Shaped Au Nrcore-Pt/Pdshell Trimetallic Nanoparticle-Decorated Reduced Graphene Oxide Nanosheets for Excellent Electrocatalysis. *J. Mater. Chem. A* **2016,** *4* (10), 3765-3776.

21. Wang, X.; Zhu, M.; Fu, W.; Huang, C.; Gu, Q.; Zeng, T. H.; Dai, Y.; Sun, Y. Au Nano Dumbbells Catalyzed the Cutting of Graphene Oxide Sheets Upon Plasmon-Enhanced Reduction. *RSC Adv.* **2016,** *6* (52), 46218-46225.

22. Sánchez-Cortés, S.; Domingo, C.; García-Ramos, J. V.; Aznárez, J. A. Surface-Enhanced Vibrational Study (Seir and Sers) of Dithiocarbamate Pesticides on Gold Films. *Langmuir* **2001,** *17* (4), 1157-1162.

23. Le, F.; Brandl, D. W.; Urzhumov, Y. A.; Wang, H.; Kundu, J.; Halas, N. J.; Aizpurua, J.; Nordlander, P. Metallic Nanoparticle Arrays: A Common Substrate for Both Surface-Enhanced Raman Scattering and Surface-Enhanced Infrared Absorption. *ACS Nano* **2008,** *2* (4), 707-718.

24. Minati, L.; Benetti, F.; Chiappini, A.; Speranza, G. One-Step Synthesis of Star-Shaped Gold Nanoparticles. *Colloids Surf., A* **2014,** *441* (0), 623-628.

25. Küstner, B.; Gellner, M.; Schütz, M.; Schöppler, F.; Marx, A.; Ströbel, P.; Adam,

P.; Schmuck, C.; Schlücker, S. Sers Labels for Red Laser Excitation: Silica-Encapsulated Sams on Tunable Gold/Silver Nanoshells. *Angew. Chem. Int. Ed.* **2009,** *48* (11), 1950-1953.

26. Personick, M. L.; Langille, M. R.; Zhang, J.; Mirkin, C. A. Shape Control of Gold Nanoparticles by Silver Underpotential Deposition. *Nano Lett.* **2011,** *11* (8), 3394-3398.

27. Langille, M. R.; Personick, M. L.; Zhang, J.; Mirkin, C. A. Defining Rules for the Shape Evolution of Gold Nanoparticles. *J. Am. Chem. Soc.* **2012,** *134* (35), 14542-14554.

28. Rodriguez-Lorenzo, L.; Romo-Herrera, J. M.; Perez-Juste, J.; Alvarez-Puebla, R. A.; Liz-Marzan, L. M. Reshaping and Lspr Tuning of Au Nanostars in the Presence of Ctab. *J. Mater. Chem.* **2011,** *21* (31), 11544-11549.

29. Pandian Senthil, K.; Isabel, P.-S.; Benito, R.-G.; Abajo, F. J. G. d.; Luis, M. L.-M. High-Yield Synthesis and Optical Response of Gold Nanostars. *Nanotechnology* **2008,** *19* (1), 015606.

30. Yuan, H.; Khoury, C. G.; Hwang, H.; Wilson, C. M.; Grant, G. A.; Vo-Dinh, T. Gold Nanostars: Surfactant-Free Synthesis, 3d Modelling, and Two-Photon Photoluminescence Imaging. *Nanotechnology* **2012,** *23* (7), 075102.

31. Mahurin, S. M.; John, J.; Sepaniak, M. J.; Dai, S. A Reusable Surface-Enhanced Raman Scattering (Sers) Substrate Prepared by Atomic Layer Deposition of Alumina on a Multi-Layer Gold and Silver Film. *Appl. Spectrosc.* **2011,** *65* (4), 417-422.

32. Xia, X.; Li, W.; Zhang, Y.; Xia, Y. Silica-Coated Dimers of Silver Nanospheres as Surface-Enhanced Raman Scattering Tags for Imaging Cancer Cells. *Interface Focus* **2013,** *3* (3).

33. Bukasov, R.; Shumaker-Parry, J. S. Siver Nanocrescents with Infrared Plasmonic Properties as Tunable Substrates for Surface Enhanced Infrared Absorption Spectrscopy. *Anal. Chem.* **2009,** *81* (4531-4535).

34. Chirumamilla, M.; Toma, A.; Gopalakrishnan, A.; Das, G.; Zaccaria, R. P.; Krahne, R.; Rondanina, E.; Leoncini, M.; Liberale, C.; De Angelis, F.; Di Fabrizio, E. 3d Nanostar Dimers with a Sub-10-Nm Gap for Single-/Few-Molecule Surface-Enhanced Raman Scattering. *Adv. Mater.* **2014,** *26* (15), 2353-2358.

35. Olejnik, M.; Agarwal, A.; Zaleszczyk, W.; Kotov, N. A.; Mackowski, S. Gold Nanoparticles with Elongated Shapes: Synthesis and Optical Properties. *Acta Phys. Pol., A* **2012,** *122* (2), 346-349.

36. Bukasov, R.; Shumaker-Parry, J. S. Highly-Tunable Infrared Extinction

Properties of Gold Nanocrescents. *Nano Lett.* **2007,** *7*, 1113-1118.

37. Jahng, J.; Brocious, J.; Fishman, D. A.; Huang, F.; Li, X.; Tamma, V. A.; Wickramasinghe, H. K.; Potma, E. O. Gradient and Scattering Forces in Photoinduced Force Microscopy. *Phys. Rev. B* **2014,** *90* (15), 155417.

38. Song, S. W.; Jeong, Y.; Kwon, S. Photocurable Polymer Nanocomposites for Magnetic, Optical, and Biological Applications. *IEEE J. Sel. Quantum Electron.* **2015,** *21* (4), 324-335.

39. Czaplicki, R.; Mäkitalo, J.; Siikanen, R.; Husu, H.; Lehtolahti, J.; Kuittinen, M.; Kauranen, M. Second-Harmonic Generation from Metal Nanoparticles: Resonance Enhancement Versus Particle Geometry. *Nano Lett.* **2015,** *15* (1), 530-534.

40. Dong, Z.; Asbahi, M.; Lin, J.; Zhu, D.; Wang, Y. M.; Hippalgaonkar, K.; Chu, H.-S.; Goh, W. P.; Wang, F.; Huang, Z.; Yang, J. K. W. Second-Harmonic Generation from Sub-5 Nm Gaps by Directed Self-Assembly of Nanoparticles onto Template-Stripped Gold Substrates. *Nano Lett.* **2015,** *15* (9), 5976-5981.

41. Pan, D.; Pramanik, M.; Senpan, A.; Ghosh, S.; Wickline, S. A.; Wang, L. V.; Lanza, G. M. Near Infrared Photoacoustic Detection of Sentinel Lymph Nodes with Gold Nanobeacons. *Biomaterials* **2010,** *31* (14), 4088-4093.

42. Diaz Fernandez, Y. A.; Gschneidtner, T. A.; Wadell, C.; Fornander, L. H.; Lara Avila, S.; Langhammer, C.; Westerlund, F.; Moth-Poulsen, K. The Conquest of Middle-Earth: Combining Top-Down and Bottom-up Nanofabrication for Constructing Nanoparticle Based Devices. *Nanoscale* **2014,** *6* (24), 14605-14616.

43. Zohar, N.; Chuntonov, L.; Haran, G. The Simplest Plasmonic Molecules: Metal Nanoparticle Dimers and Trimers. *J. Photochem. Photobiol. C* **2014,** *21*, 26-39.

44. Nordlander, P.; Oubre, C.; Prodan, E.; Li, K.; Stockman, M. I. Plasmon Hybridization in Nanoparticle Dimers. *Nano Lett.* **2004,** *4* (5), 899-903.

45. Novotny, L.; Bian, R. X.; Xie, X. S. Theory of Nanometric Optical Tweezers. *Phys. Rev. Lett.* **1997,** *79* (4), 645-648.

46. Jensen, T. R.; Duval, M. L.; Kelly, K. L.; Lazarides, A. A.; Schatz, G. C.; Van Duyne, R. P. Nanosphere Lithography: Effect of the External Dielectric Medium on the Surface Plasmon Resonance Spectrum of a Periodic Array of Silver Nanoparticles. *J. Phys. Chem. B* **1999,** *103* (45), 9846-9853.

47. Cennamo, N.; D'Agostino, G.; Donà, A.; Dacarro, G.; Pallavicini, P.; Pesavento, M.; Zeni, L. Localized Surface Plasmon Resonance with Five-Branched Gold Nanostars in a Plastic Optical Fiber for Bio-Chemical Sensor Implementation. *Sensors (Basel, Switzerland)* **2013,** *13* (11), 14676-14686.

48. Chen, H.; Kou, X.; Yang, Z.; Ni, W.; Wang, J. Shape- and Size-Dependent Refractive Index Sensitivity of Gold Nanoparticles. *Langmuir* **2008,** *24* (10), 5233-5237.

49. Shumaker-Parry, J. S.; Rochholz, H.; Kreiter, M. Fabrication of Crescent-Shaped Optical Antennas. *Adv. Mater.* **2005,** (17), 2131-2134.

50. Haynes, C. L.; Van Duyne, R. P. Nanosphere Lithography: A Versatile Nanofabrication Tool for Studies of Size-Dependent Nanoparticle Optics. *J. Phys. Chem. B* **2001,** *105* (24), 5599-5611.

51. Vogel, N.; Goerres, S.; Landfester, K.; Weiss, C. K. A Convenient Method to Produce Close- and Non-Close-Packed Monolayers Using Direct Assembly at the Air–Water Interface and Subsequent Plasma-Induced Size Reduction. *Macromol. Chem. Phys.* **2011,** *212* (16), 1719-1734.

52. Bosman, M.; Zhang, L.; Duan, H.; Tan, S. F.; Nijhuis, C. A.; Qiu, C. W.; Yang, J. K. W. Encapsulated Annealing: Enhancing the Plasmon Quality Factor in Lithographically–Defined Nanostructures. *Sci. Rep.* **2014,** *4*, 5537.

53. Jung, L. S.; Campbell, C. T.; Chinowsky, T. M.; Mar, M. N.; Yee, S. S. Quantitative Interpretation of the Response of Surface Plasmon Resonance Sensors to Adsorbed Films. *Langmuir* **1998,** *14*, 5636-56487.

54. Willets, K. A.; Van Duyne, R. P. Localized Surface Plasmon Resonance Spectroscopy and Sensing. *Ann. Rev. Phys. Chem.* **2007,** *58* (1), 267-297.

55. Loudon, R. The Raman Effect in Crystals. *Adv. Phys.* **1964,** *13* (52), 423-482.

56. Fontana, M. D.; Ben Mabrouk, K.; Kauffmann, T. H., Raman Spectroscopic Sensors for Inorganic Salts. In *Spectroscopic Properties of Inorganic and Organometallic Compounds: Techniques, Materials and Applications*, The Royal Society of Chemistry: 2013; Vol. 44, pp 40-67.

57. Habib, A.; Tabata, M.; Wu, Y. G. Formation of Gold Nanoparticles by Good's Buffers. *Bull. Chem. Soc. Jpn.* **2005,** *78* (2), 262-269.

58. Moskovits, M. Surface-Enhanced Raman Spectroscopy: A Brief Retrospective. *J. Raman Spectrosc.* **2005,** *36* (6-7), 485-496.

59. Liu, X.-L.; Wang, J.-H.; Liang, S.; Yang, D.-J.; Nan, F.; Ding, S.-J.; Zhou, L.; Hao, Z.-H.; Wang, Q.-Q. Tuning Plasmon Resonance of Gold Nanostars for Enhancements of Nonlinear Optical Response and Raman Scattering. *J. Phys. Chem. C* **2014,** *118* (18), 9659-9664.

60. Xie, J.; Lee, J. Y.; Wang, D. I. C. Seedless, Surfactantless, High-Yield Synthesis of Branched Gold Nanocrystals in Hepes Buffer Solution. *Chem. Mater.* **2007,** *19* (11), 2823-2830.

61. William D. Callister, J., Phase Transformations in Metals. In *Materials Science and Engineering. An Introduction*, 7th ed.; John Wiley & Sons, Inc.: 2007; pp 311-324.

62. Ramsey, J. D.; Zhou, L.; Kyle Almlie, C.; Lange, J. D.; Burrows, S. M. Achieving Plasmon Reproducibility from Surfactant Free Gold Nanostar Synthesis. *New J. Chem.* **2015,** *39* (12), 9098-9108.

63. Le Ru, E. C.; Blackie, E.; Meyer, M.; Etchegoin, P. G. Surface Enhanced Raman Scattering Enhancement Factors: A Comprehensive Study. *J. Phys. Chem. C* **2007,** *111* (37), 13794-13803.

64. Griffiths, P. R., Surface-Enhanced Infrared Absorption Spectroscopy: Principles and Applications. In *Spectroscopic Properties of Inorganic and Organometallic Compounds: Techniques, Materials and Applications*, The Royal Society of Chemistry: 2013; Vol. 44, pp 95-122.

65. Su, Z.-F.; Sun, S.-G.; Wu, C.-X.; Cai, Z.-P. Study of Anomalous Infrared Properties of Nanomaterials through Effective Medium Theory. *J. Chem. Phys.* **2008,** *129* (4), 044707.

66. Ross, D.; Aroca, R. Effective Medium Theories in Surface Enhanced Infrared Spectroscopy: The Pentacene Example. *J. Chem. Phys.* **2002,** *117* (17), 8095-8103.

67. Dieringer, J. A.; McFarland, A. D.; Shah, N. C.; Stuart, D. A.; Whitney, A. V.; Yonzon, C. R.; Young, M. A.; Zhang, X.; Van Duyne, R. P. Introductory Lecture Surface Enhanced Raman Spectroscopy: New Materials, Concepts, Characterization Tools, and Applications. *Faraday Discuss.* **2006,** *132* (0), 9-26.

CHAPTER 5

SPECTROSCOPIC APPLICATIONS OF PLASMONIC NANOMITE-COATED STRUCTURES

5.1 Introduction

When light couples to nanoparticles, the coherent oscillation of electrons from the metal-dielectric interface compresses into localized areas generating regions of high-electron density, or "hot spots." This unique optical property is called localized surface plasmon resonance (LSPR). The LSPR wavelength of the nanostructures is sensitive to changes in the local refractive index (RI). The electron-dense hot spots generate an electromagnetic (EM) field that can amplify signals in vibrational spectroscopy. The signal enhancement is utilized in a variety of sensing applications such as surface enhanced Raman spectroscopy (SERS), surface enhanced infrared absorption (SEIRA) spectroscopy, and in ex vivo and in vivo label-free biosensing.[1-14] The signal enhancement and high sensitivity of the hotpots to changes in the local environment is intensified when the EM field is confined into sharp-tips of nanoparticles such as nanostars, nanocrescents, nanorods, and nanotriangles.[1, 11, 15-23] In Chapter 4, a synthetic modification for preparing sharp-tipped gold (Au) nanoparticles on fabricated Au structures was introduced that combines top-down fabrication with bottom-up synthesis.

The nanomite synthesis uses fabricated nanostructures as seeds or "hosts" for the reduction of Au (III) to Au^0 leading to the formation of Au branches. The branching increases hot spot density and, due to the nm-scale radius of curvature of the branches, there is potential to increase sensitivity of the LSPR response. By using arrayed host structures, a large, higher-density substrate is fabricated that can be used for refractive index sensing and surface-enhanced spectroscopies. Compared to synthesized nanoparticles, fabricated nanostructures with fixed substrate positions prevent aggregation and minimize signal fluctuation. The nanomite decorations also maintain the host nanostructures' properties such as polarization-dependent LSPR response.

5.1.1 *Bulk Refractive Index Sensitivity*

Many biosensing applications make use of the refractive index sensitivity (RIS) of plasmonic nanoparticles. The shape of a nanoparticle improves refractive index sensitivity via antenna effects: sharp-tipped nanostructures, like nanomites, confine the electric field to a smaller volume that leads to larger localized field enhancements and higher sensitivity to changes in the near-field.[23] As shown in Table 5.1, structures with sharp tips are more sensitive to changes in the bulk refractive index of the near-field for both fabricated nanoparticles (nanotriangles compared to nanoholes) and synthetic nanoparticles (branches compared to nanospheres).

Bulk RIS is used to infer the substrate's ability to sense a shift in the LSPR due to the local change in the dielectric environme. For a noble metal surface, the dependence of the LSPR wavelength maximum (λ_{max}) on refractive index is expressed as:[24]

$$\Delta\lambda_{max} = m\Delta n(1 - e^{-2d/l_d}) \tag{5.1}$$

Table 5.1 Bulk refractive index sensitivity of different nanoparticles

Structure	Method	RIS* (nm RIU^{-1})	LSPR λ_{max} (nm)
Ag nanotriangles[25]	Top-Down	200	600
Au Nanohole[26]	Top-Down	159	675
Au Nanosphere[27]	Synthesis	44	527
Au 5-armed Nanostar[28]	Synthesis	175	640
		580	1220
Au Branches[27]	Synthesis	703	1141
Au Bipyramids[27]	Synthesis	540	1096

*refractive index sensitivity; Ag = silver

In this equation, $\Delta\lambda_{max}$ is the LSPR wavelength shift, *m* is the bulk refractive index response, *n* is the change in refractive index induced by an adsorbate, *d* is the effective adsorbate thickness, and l_d, approximated as an exponential decay, is the characteristic EM field decay length. This equation shows that as *m* increases, the LSPR absorption maximum (λ_{max}) will red-shift. Substrates that are more sensitive to changes in RI will demonstrate a larger magnitude of red-shifting of the LSPR. The λ_{max} shift as the result of an adsorbate binding (increase in RI) is the principle of biosensing experiments and it is critical to design substrates that offer large refractive index responses (*m*) to improve limit of detection and resolution.[29]

5.1.2 *Surface-Enhanced Raman Spectroscopy*

Vibrational spectroscopy techniques, such as Raman spectroscopy, use surface-enhanced substrates to improve signal. The signal enhancement from nanostructures relies on similar nanoparticle design as those discussed for RI sensing. Confinement of the EM near-field at the tips of structures, as in nanostars and branched nanoparticles, generates larger signal enhancements compared to spheres or planar surfaces.

SERS is used to determine the vibrational modes of surface-bound molecules by detecting the scattered light from laser-illuminated samples. SERS is active when the polarizability of the molecule is anisotropic; the polarizability in SERS relates to a dipole moment *induced* by the external electric field. The majority of the scattered light is the result of elastic scattering, known as Rayleigh scattering, and is the same frequency as the excitation source. Raman scattering occurs due to the inelastic interaction between a molecule and the EM field of the source.[30] Generally, a photon of the incident light excites the ground vibrational or rotational state into a virtual energy state.[31] From the virtual state, an inelastically scattered photon is emitted shifted at a higher (anti-Stokes) or lower (Stokes) energy than the source photon. The frequency of the shift is characteristic of specific molecular vibrations. Because Raman scattering only occurs in one in a million photons, the molecule of interest needs to be present at high concentrations or the Raman signal needs to be enhanced.

Metal nanoparticles provide surface enhancement for Raman spectroscopy in two ways: EM enhancement and chemical enhancement.[32-33] EM enhancement results from two mechanisms. When the laser source has the same resonance frequency as the LSPR of the nanoparticle, the resonant polarization of electrons enhances the incident EM field (E_0) and enhances the scattered field. Both processes contribute $|E|^2$ increases in Raman intensity.[33] Chemical enhancement accounts for one or two orders of magnitude enhancement and is due to charge transfer or coupling of the metal and the molecules.[33-34]

The enhancement factor (EF) of the substrates is determined using the peak intensity relative to the number of molecules probed as determined by the nanoparticle surface area. For Raman EF, the ratio of the Raman substrate intensity (I_{SERS}) and the

Raman intensity from a Au film (I_{Bulk}) is used with corrections for the surface area of the SERS substrate (SA_{SERS}) and the SA of the Au film (SA_{BULK}) (Eq. 5.2).[35-36]

$$EF = \frac{I_{SERS}}{I_{BULK}} x \frac{SA_{BULK}}{SA_{SERS}} \quad (5.2)$$

There are several versions of Eq. 5.2 that inflate the EF by several orders of magnitude.[36] However, the simplistic version of EF in Eq. 5.2 takes into account the surface area limitations of the fabrication process. In the case of colloidal lithography, nanosphere templates are hexagonally close-packed to form arrays. The size of the template directs the size of the nanoparticle, which determines the wavelength of the plasmon resonance mode. Therefore, structures fabricated by colloidal lithography cannot be more closely packed than the array while maintaining the desired plasmon resonance (because the resonance is size specific). Thus, the maximum nanoparticle density on the substrate is absolute; however, nanoparticle density can be decreased for some colloidal lithography techniques to generate disperse nanoparticle substrates. Any manipulations of Eq. 5.2 that adjust for the specific hot spot area neglect that the substrates' nanostructure-density and footprint surface area are fixed at a given LSPR and geometry. Therefore, to increase the sensitivity of the substrate without aggregation, the nanoparticles have to be optimized for enhancement rather than more densely packed (because the structures cannot be more densely packed). Optimization can use LSPR coupling via nanogaps to increase the strength of the hot spots or by introducing sharp tips as discussed previously.

To increase refractive index sensitivity and enhancement for SERS, the nanomite synthesis combines a simple top-down fabrication technique with bottom-up synthesis to generate highly decorated, well-arrayed nanostructures. The primary benefits are 2-fold: using fabricated nanostructures as the host prevents aggregation thereby increasing signal

stability and it allows for an increase in hot spot density on the nanostructures. Increasing hot spot density generates stronger SERS signals by decorating the host with branched features.

We show that the synthesis can be applied to gold nanotriangle (AuNT) and gold nanocrescent (AuNC) geometries, which suggests that any fabricated nanoparticle can be used as a host for the synthesis of branched nanoparticles, or "nanomites." Because the host nanoparticle retains its unique optical properties, host structures with polarization-dependent resonance modes and resonances extending into the IR, like the AuNCs, maintain these properties after synthesis. AuNCs were fabricated with resonances in the IR to evaluate polarization dependence. The synthetic nanomite decoration of these AuNCs is denoted as NM@NC. The AuNT host structures ranged in template size from 120, 190, and 330 nm ($NM@NT_{size}$ or $Au@NT_{size}$).

5.2 Materials and Methods

5.2.1 *Materials*

Gold pellets were purchased from K.J. Lesker (Clairton, PA). Glass substrates of BK7 glass microscope slides were purchased from Ted Pella, Inc. (Redding, CA).Various sizes of Aldehyde/Sulfate Latex Beads, 4% w/v, were purchased from Life Sciences Solutions, Inc. (Grand Island, NY). Absolute ethanol was purchased from Pharmco-Aaper. Concentrated H_2SO_4 and 30 wt % NaOH were purchased from EMD Chemicals. Concentrated HCl, and 30% H_2O_2, ethanolamine (>98%), and $HAuCl_4$ were purchased from Sigma-Aldrich. $AgNO_3$ was purchased from Fischer Chemical. 4-(2-hydroxyethyl)-1-piperazineethanesulfonic acid) (HEPES) buffer was purchased from Gold

Biotechnology company. 4-Aminothiophenol (97 %) was purchased from Alfa-Aesar. Nanopure water (18 mΩ) (Barstead NANOpure Diamond) was used to prepare all solutions and rinse glassware after cleaning.

5.2.2 *Substrate Preparation*

Glass microscope slides were cut into 1" x 1" sections and cleaned by immersion in piranha acid (3:1 volumetric ratio of H_2SO_4:30 % H_2O_2) for 45 min. (Caution: piranha acid is a strong oxidizer and has been known to detonate upon contact with organic material.) The substrates were rinsed three times with nanopure water and transferred to a 60 °C detergent bath (5:1:1 volumetric ratio of H_2O, NH_4OH: 30 % H_2O_2) for 60 min under sonication. Slides were rinsed three times with nanopure water, rinsed with isopropanol, dried with N_2 and used within one week. CaF_2 and silicon wafers were rinsed with nanopure water, isopropanol, and then dried with N_2. The substrates were then treated with ultra-violet ozone cleaning for 10 min (Jelight 342, Irvine CA) and used promptly for fabrication.

5.2.3 *Colloidal Lithography*

Nanosphere lithography (NSL) and nanosphere template lithography (NTL) were used to fabricate the AuNTs and AuNCs, respectively, and have been described previously.[37-39] Refer to Figure 1.3A and B for schematic representations of fabrication. For all host nanostructures, sulfate/aldehyde functionalized polystyrene nanospheres were closed-packed onto the desired substrate (glass slides, silicon wafer, or CaF_2) using a similar method to Weiss et al.[40] Nanotriangle fabrication has been detailed in

Section 4.2.3.

Nanosphere template lithography was used to fabricate nanocrescents. Sulfate/aldehyde functionalized polystyrene nanospheres (1.4 μm diameter) were closed-packed onto the desired substrate (glass slides or silicon wafer). After template deposition, the substrates were etched with an oxygen plasma (PlasmaLab 80 Plus, Oxford Instruments) for 8 min at 75 W and flow rate of 15 sccms. The substrates were placed on 40° mounts and chromium (Cr) and Au were deposited. A 3 nm Cr adhesion layer was deposited (1 Å/s) followed by 30 nm Au film (1 Å/s), as measured by a quartz crystal microbalance (XPC2 Inficon, East Syracuse, NY) under high vacuum (2.0×10^{-6} Torr). An argon ion milling system (PlasmaLab 80 Plus, Oxford Instruments) was used to remove the Au film at a power of 100 W and flow rate of 10 sccm. The polystyrene templates were removed by lift-off using transparent tape and samples were stored under nitrogen.

5.2.4 *Synthesis*

Fabricated AuNT and AuNC substrates were cut into 2.5 cm x 0.8 cm portions for the nanomite synthesis. The synthesis protocol is detailed in Section 4.2.4.

5.2.5 *Instrumentation*

The optical properties of the NM@NT on glass substrates were characterized by transmission UV-vis spectroscopy or transmission Fourier-transform infrared (FTIR) spectroscopy. Extinction spectra were collected with a Perkin-Elmer Lambda 750 UV/vis spectrophotometer. The λ_{max} was determined using Spectrum software and the center of

gravity function. FT-IR spectra of NM@NT and AuNT on CaF_2 substrates were acquired using a Spectrum 100 FTIR (Perkin Elmer) and polarization data were collected with a MID-IR polarizer (SPECAC, Oprington, Kent, England). Raman spectra from samples prepared on silicon wafers were collected with a 785 nm PI-200 Laboratory Raman Analyzer (Process Instruments, Salt Lake City, UT) at 100 mW. Scanning electron microscopy (SEM) (FEI NovaNano 630 equipped with a Helix detector) was used image structures.

5.2.6 *Functionalization*

Ultraviolet ozone cleaning (10 min) was used to prepare nanoparticle substrates for chemical functionalization. To functionalize SERS substrates, samples were immersed in 10 mM 4-aminothiophenol (4-ATP) in ethanol for 14 h and rinsed 3 times with ethanol and 3 times with nanopure water.

5.3 Results and Discussion

The decoration of the fabricated host nanoparticles via the nanomite synthesis is detailed in Chapter 4. The synthetic routine uses fabricated AuNT and AuNC as host nanostructures for a synthetic protocol based on nanostar syntheses.[22, 41-42] AuNTs are fabricated using nanosphere lithography (NSL).[39] Close-packed polystyrene nanospheres are deposited on planar substrates and then metal is deposited normal to the surface. AuNCs are fabricated in a similar fashion with NTL, but use oxygen plasma etching to reduce the size of the polystyrene templates and samples are placed on 40° mounts. Metal is then deposited to under-fill the template and Ar^+ reactive ion etching is used to remove

unprotected material.[37-38] Both AuNTs and AuNCs use a Cr adhesion layer prior to Au deposition. Following template removal, the nanoparticles are prepared for synthesis with UVO cleaning. The nanomite synthesis is carried out at low temperature (4 °C) to promote nucleation of the Au. After the 1 h nucleation phase, the solution is brought to room temperature allowing the nanoparticle decorations to grow in size (Figure 5.1B). To explore the potential applications of the nanomite-AuNTs (NM@NT) and nanomite-AuNCs (NM@NC), structures were evaluated for refractive index sensitivity, SERS activity, and polarization dependence of the optical response.

5.3.1 *Polarization-Dependent Plasmon Resonance*

Anisotropic nanoparticles with an axis of symmetry are known to have polarization-dependent resonance modes. These modes can be used to selectively induce the LSPR resonance by controlling the polarization of incident light. AuNCs were chosen as host nanostructures due to the wavelength tunable polarization-dependent longitudinal and transverse resonance modes.[43] When the longitudinal dipolar resonance (long axis) is selected by polarizing the electric field parallel to the long axis, electrons

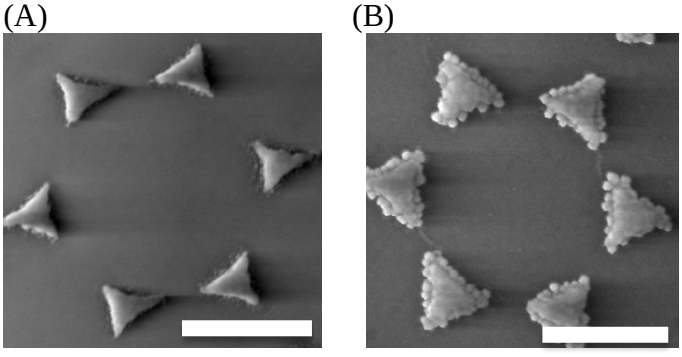

Figure 5.1 SEM images of (A) $AuNT_{330}$ and (B) $NM@NT_{330}$. Scale bars are 300 nm.

oscillate from tip to tip leading to confinement of the electron density in those regions (Figure 5.2A). The transverse resonance mode (short axis) is selected by polarizing light 90° relative to the long axis, confining the oscillating electrons between the tip and backbone (Figure 5.2B).

To explore the polarizability of the host nanostructures with the addition of nanomite decorations, host AuNCs were fabricated with 1.4 μm templates. NM@NC with a short axis LSPR (λ_{SA}) at 2220 nm (4500 cm^{-1}) and long axis LSPR (λ_{LA}) at 4160 nm (2400 cm^{-1}) (Figure 5.3A) were compared to AuNC with λ_{SA} of 2564 nm (3900 cm^{-1}) and λ_{LA} of 5130 nm (1950cm^{-1}) (Figure 5.3B). There are vibrational peaks centered at 3000 cm^{-1} present on the NM@NC and the AuNC spectra due to functionalization with dodecanethiol (DDT). While the results of the functionalization with DDT are interesting, the polarization-dependent plasmon modes will be the focus of this section. The long axis and short axis resonance modes were selectively induced by rotating the polarization of light in 10º increments with respect to the structure. The NM@NC spectra show the independent excitation of the λ_{LA} and λ_{SA} resonance modes (Figure 5.3C). At 40º of

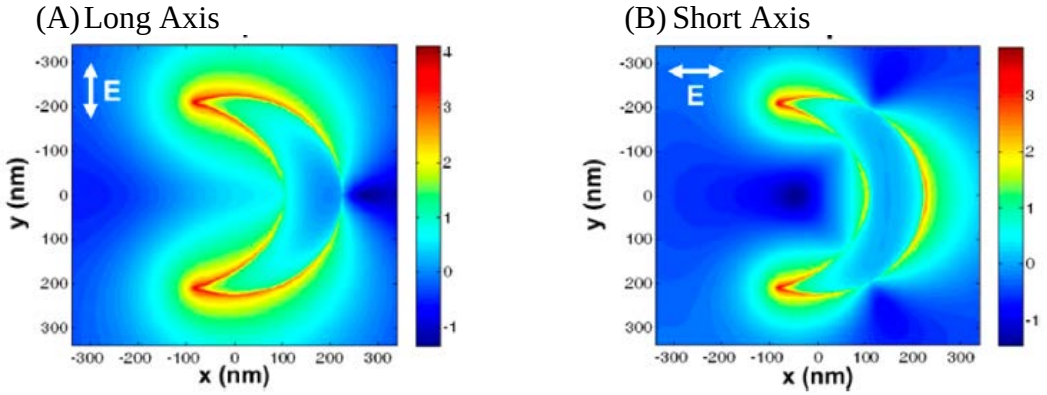

Figure 5.2 Near-field enhancement of the electric field of AuNCs. Reprinted with permission from Cooper, C. T.; Rodriguez, M.; Blair, S.; Shumaker-Parry, J. S., Polarization Anisotropy of Multiple Localized Plasmon Resonance Modes in Noble Metal Nanocrescents. J. Phys. Chem. C 2014, 118 (2), 1167–1173, Figure 3.

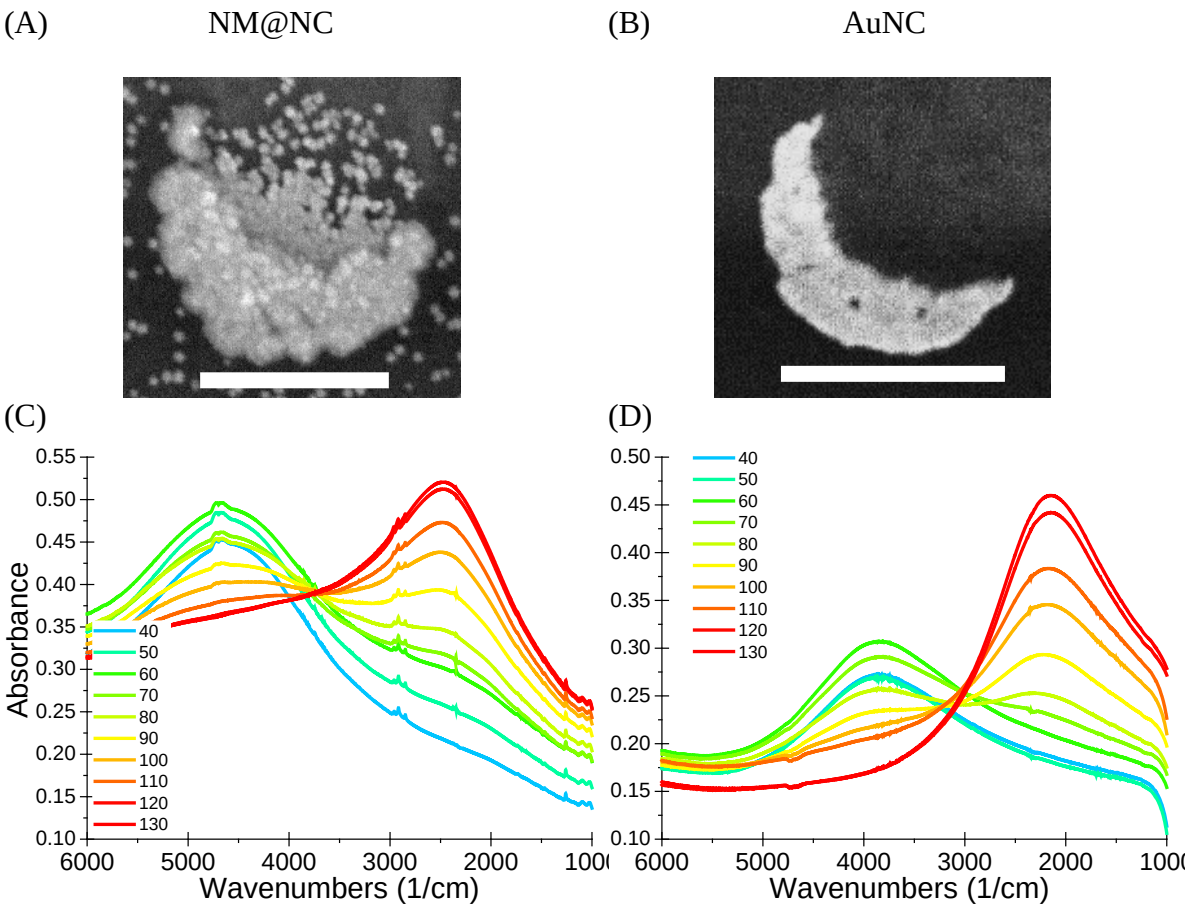

Figure 5.3 SEM images of (A) NM@NC and (B) AuNC. Scale bars are 500 nm. FT-IR spectra of (C) NM@NC and (D) AuNC.

rotation with respect to the substrate, the short axis (SA) resonance mode is active o5 “on” and the long axis resonance mode is “off.” By rotating the polarized light an additional 90º to 130º, the long axis (LA) resonance mode is induced. Between 40º and 130º, the LA and SA LSPR modes are simultaneously induced as demonstrated by the presence of both LA and SA resonance peaks.

The characteristic polarization-dependent induction of the LA and SA resonance modes was also observed for the AuNC (Figure 5.3D). This demonstrates that the NM@NC maintained the same polarization-dependent resonance behavior as the host AuNC. The difference in absorbance intensity between the LA and SA when comparing the AuNC to the NM@NC is likely related to structural differences.

The SEM image of the AuNC (Figure 5.3B) shows pitting in the nanostructure that could be caused by over-etching or incomplete film formation during Au deposition. The SEM image of the NM@NC (Figure 5.3A) shows interesting details that are not seen on the smaller AuNT substrates (Figure 5.1) including background Au structures and irregular deposition of Au decorations on the inner rim of the AuNC. The presence of background Au particles *not* associated to the host structure could be due to small islands of Au that are not removed during the etching process and serve as host structures. To determine if these irregularities influence the amplitude of the LSPR response, future work will include sonication experiments to determine if the extraneous background Au is attached to the surface. In summary, the nanomite synthesis does not impact the polarization-dependent resonance modes of host nanostructures. However, the relative amplitude of the LA and SA resonance modes could be affected by the nanomite decorations.

5.3.2 *Refractive Index Sensitivity of Nanomite-Decorated Nanotriangles*

To investigate the refractive index sensitivity of nanomite decorations, AuNT with a 330 nm nanosphere template were fabricated with NSL (Figure 5.1). Refractive index sensitivity is determined by placing samples in solutions of increasing RI, and measuring the shift of the LSPR λ_{max} (nm) versus the refractive index units (RIU) of the solutions. AuNT and NM@NT substrates were placed in cuvettes and the peak shift ($\Delta\lambda_{max}$) was measured in air (RI = 1.00), nanopure water (RI=1.33), ethanol (RI=1.361) and CS_2 (RI=1.63). Figure 5.4A and B show the extinction spectra of $AuNT_{330}$ and $NM@NT_{330}$, respectively, in the presence of the different refractive index solutions. Figure 5.4C and D show the RI vs LSPR shift of each LSPR peak with the sensitivity (*m*) determined using linear regression. Substrates show the presence of two LSPR peaks, one at ~600 nm and a very broad peak at ~1000 nm.

The summary of the peak shifts in response to the change in RI are shown in Table 5.2. Decorated structures are more sensitive to the absolute shifts in refractive index, as indicated by the larger *m* for both the ~600 nm and ~1000 nm LSPR peaks (Figure 5.4B). For the 600 nm peak, the starting LSPR wavelength (λ_{start}) has a range between 620 and 670 nm. The NM@NT has the highest sensitivity with m_{600} = 375 nm RIU^{-1} compared to the AuNT with *m* = 57 nm RIU^{-1}, which is a 7-fold increase in RI sensitivity. After 11 days, the NM@NT m_{600} dropped 70 % from 375 to ~110 nm RIU^{-1}.

Other fabricated nanostructure in the 600-700 nm range include Au nanohole arrays with an *m* of 159 nm RIU^{-1} and Ag nanotriangles (AgNT) with an *m* of 200 nm RIU^{-1}.[25-26] NM@NT surpass both of these substrates in sensitivity measurements. At the

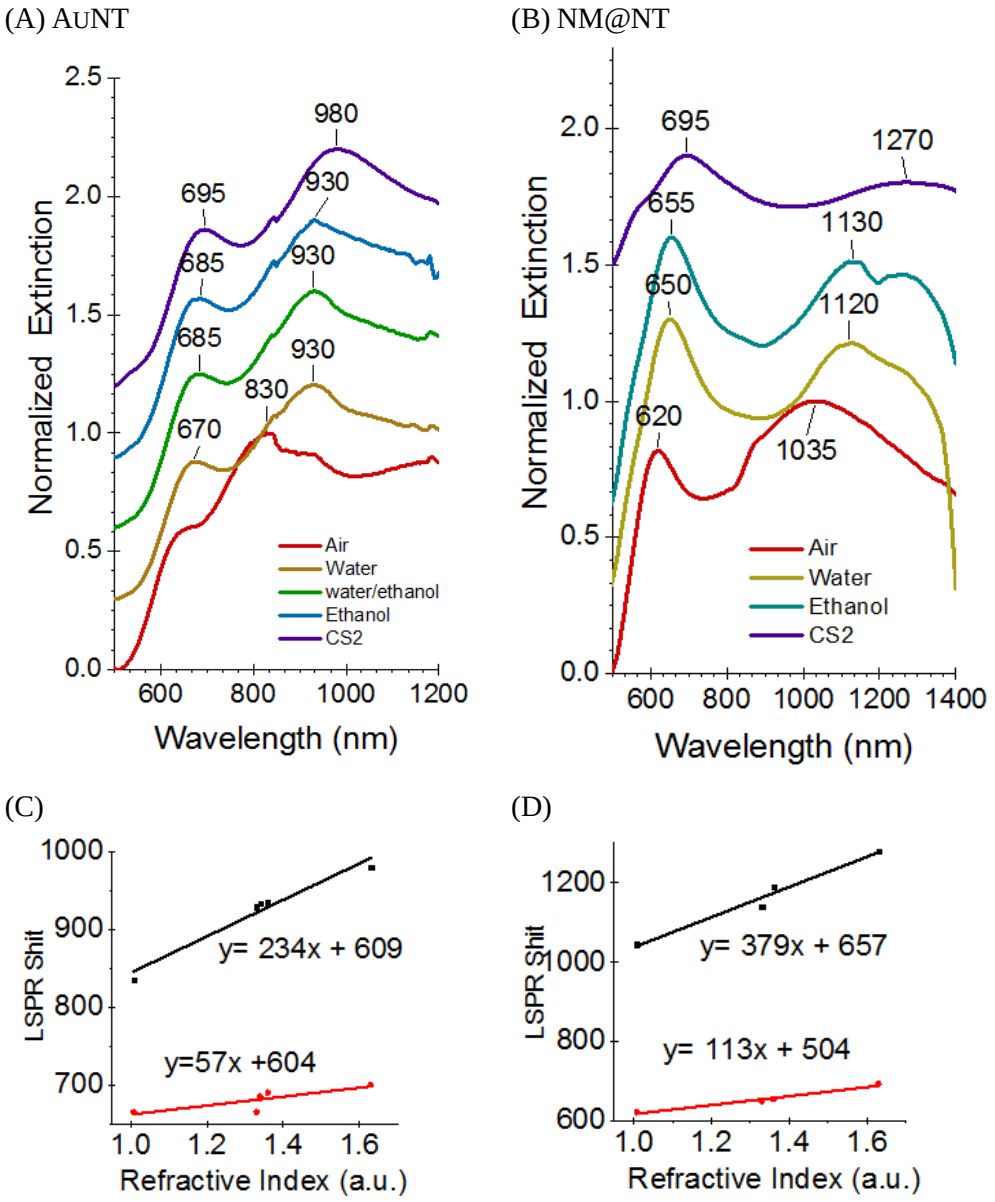

Figure 5.4 Extinction spectra of (A) AuNT and (B) NM@NT in air, water, ethanol, and CS2. (C) AuNT and (D) NM@NT show the refractive index sensitivity determination by linear regression of the refractive index vs LSPR shift for ~1000 nm LSPR peak (black) and 700 nm LSPR peak (red).

Table 5.2 Bulk refractive index sensitivity of NM@NT_{330} and $AuNT_{330}$. N =1 per row.

Substrate	λ_{max} (nm)	m_{600} (nm RIU^{-1})	λ_{max} (nm)	m_{1000} (nm RIU^{-1})	Days between synthesis and measurements
NM@NT	625	375	1100	505	1
NM@NT	620	104	1023	407	11
NM@NT	622	119	1045	379	11
AuNT	665	57	835	234	1

λmax is the starting peak position in air (RI = 1.00)

600-700 nm LSPR range, Ag is known to have a higher sensitivity than Au for similar structures, so the larger sensitivity of the Au NM@NT compared to AgNT at the same wavelength shows that the NM@NT are a significant improvement over undecorated AuNT.[20, 44]

The amplitude ratio of the 600 and 1000 nm peaks of the NM@NT changed between the air and CS_2 measurements. Unlike the AuNT which maintained a relatively similar amplitude ratio, the amplitude of the 1000 nm LSPR peak of the NM@NT decreased relative to the 600 nm LSPR peak amplitude. The apparent broadening of the peak could be partially attributed to the more significant shift (240 nm) of the resonance into the near-IR. However, the 600 nm peak also shows broadening for the CS_2 spectrum. The broadening of these peaks suggest that structural changes are occurring that decrease the sharpness of the nanomite decorations. Potential causes include ligand re-organization or instability of the ligands to CS_2 resulting in structural degradation (i.e. rounding).

The NM@NT had a 2-fold increase in m_{1000} compared to the AuNT, although this value is convoluted by the λ_{max} positions of 1000 nm and 835 nm, respectively. By being further in the near-IR, the NM@NT would be expected to have a higher sensitivity than

the AuNT based on relative wavelength position. After 11 days of dry storage, the NM@NT m_{1000} decreased by 22 %. Both AuNT and NM@NT systems show broadening for the ~1000 nm peak along with some peak deformation caused by ethanol interference. Due to dephasing and increased radiative damping, broadening of the peaks in the near-IR and mid-IR is typical for nanoparticles systems and results in a resolution reduction. Because of this broadening, others have determined that the best balance between sensitivity and resolution for LSPR-based biosensing is between 700 and 900 nm.[45-46]

The variation in *m* for the NM@NT at 1 day and at 11 days after synthesis suggests that the dry storage of the substrates impacts sensitivity. Gold nanoparticle solutions are typically stored in some form of buffer or nanopure water in the dark at 4 ºC whereas the dry storage at room temperature of the NM@NT may impact the sensitivity via structural degradation.[22, 28, 47-49] Limited light and cold storage of nanoparticles in solution is preferred to prevent aggregation; once the nanoparticles are dried it can be very difficult to redisperse the structures.[50] While the host fabricated nanoparticles do not risk aggregation, the branched structures are maintained by the ligand shell formed during synthesis and these ligands can reorganize over time.[51] Lacava et al. established that Au nanoparticles stored dry at room temperature experience significant changes in physical and optical properties, possibly due to ligand loss.[49] Therefore, it is possible that ligand reorganization could lead to decreased *m* as high energy facets are no longer favored on the nanomite decorations. By storing the NM@NT in a buffer with facet-passivating ligands, it may be possible to prolong high-energy facet passivation. Further work regarding the ideal storage conditions and time lengths is necessary. Regardless, the

conservative estimate of a 7-fold increase (57 to 375 nm RIU^{-1}) in sensitivity demonstrates an encouraging step forward that could be improved with finer control of the decorations' branch length and width.

5.3.3 *SERS of 4-Aminothiophenol*

The same properties of shape control for near-field confinement that make plasmonic substrates useful for biosensing, are also beneficial for SERS.[52-53] The nanomite decorated structures offer aggregation-free substrates that have a high-density of branched features. By removing the risk for aggregation, issues with signal fluctuation are reduced. To probe the SERS application of the NM@NT, substrates generated from three different template sizes ($NM@NT_{size}$ or $AuNT_{size}$) were functionalized with 4-aminothiophenol (4-ATP) and probed with a 785 nm laser. The area of the substrates was determined before and after synthesis by processing SEM images (Figure 5.1) with ImageJ to calculate the percent coverage of the total Au structures. This percent is the *footprint* surface area because it does not take into account the 3-dimensional growth of the structures. Future work will require AFM data to approximate the structure height and topography to provide 3-dimensional surface area.

The extinction spectra of NM@NT and AuNT are shown in Figure 5.5. Both the $AuNT_{120}$ and $AuNT_{190}$ exhibit strong absorption at 350 nm with a shoulder between 400-500 nm. Going into the UV, the glass substrates begin to absorb, obscuring the LSPR of the structures below 350 nm. After synthesis, the substrates generate a peak at 535 nm ($AuNT_{190}$) and at 550 nm ($AuNT_{120}$). These peaks are the result of red-shifting of the LSPR from the obscured region in the 350-500 nm region. The resonance frequency

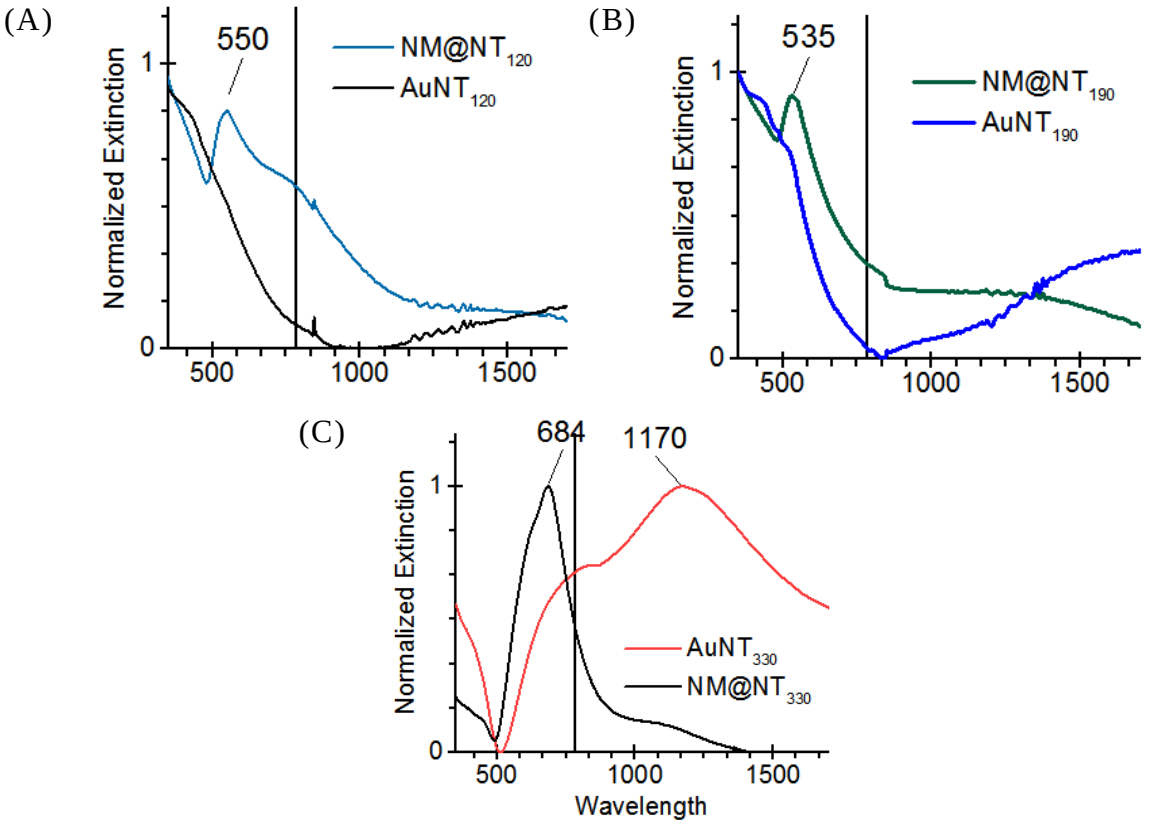

Figure 5.5 Extinction spectra comparing AuNT and NM@NT of the (A) 120 nm (B) 190 nm and (C) 330 nm templates AuNT before synthesis and after synthesis. The black line indicates the wavelength of the Raman laser source (785 nm).

changes with the addition of nanomite branching because the electron oscillation has to accommodate for the difference in EM phase between one end of the particle and the other. As the structure increases in size, the electrons oscillate over a longer distance, shifting the LSPR resonance. As a result, it would be expected that the $AuNT_{120}$ would be further blue-shifted than the $AuNT_{190}$ due to the 190 nm templates generating larger structures in general. The LSPR peak mismatch of template size and LSPR wavelength between the smaller $AuNT_{120}$ (λ_{max} = 550 nm) and the $AuNT_{190}$ (λ_{max} = 535 nm) could be due to poor packing of the smaller nanosphere templates.

Poor packing can lead to the formation of “dimer” nanotriangles and islands as

shown in Figure 5.6. The presence of these larger structures shifts the LSPR peaks of the AuNTs due to overlap of the resonance wavelength with the NTs, and if the there is a larger contribution of the dimers and islands, then the wavelength associated to these structures will dominate the spectrum. It should also be noted that structures fabricated with very small nanosphere templates tend to have a decrease in structural "fidelity." As template sizes go decrease in size, the film deposition does not fill the interstitial spaces between nanosphere templates as effectively. Unique to the NM@NT_{120} is the presence of a shoulder off of the 550 nm peak, likely attributed to dimers formed from during packing.

The $AuNT_{330}$ (red line in Figure 5.5C) spectrum shows a strong peak at 1170 nm with a shoulder centered around 790 nm, although the relative overlap makes λ_{max} assignment difficult. After synthesis, the NM@NT shoes a clear formation of a peak at

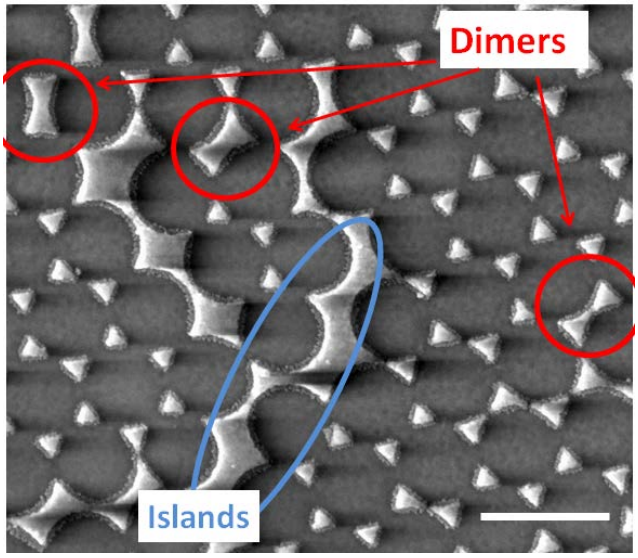

Figure 5.6 SEM image of dimers and islands formed from discrepancies in the hexagonal close-packing of nanosphere templates. Scale bar is 500 nm.

684 nm. The large peak at 1170 nm is likely due to high density of islands and dimers, although coupling between nanomite branches may also contribute. As shown in the previous spectra (Figure 5.4B), the separation of the AuNT LSPR and the island LSPR can vary. The corresponding sets (based on template size) of NM@NT and AuNT were used to probe the SERS signal of 4-ATP.

The SERS baseline-corrected spectra of 4-ATP are shown in Figure 5.7 in approximate order of peak intensity. The most prominent peaks are labelled for the $NM@NT_{120}$ and the peaks are assigned in Table 5.3. The bands can be assigned to general regions: (1) 1650-1500 cm^{-1} are C-C stretching modes with CH in-plane bending

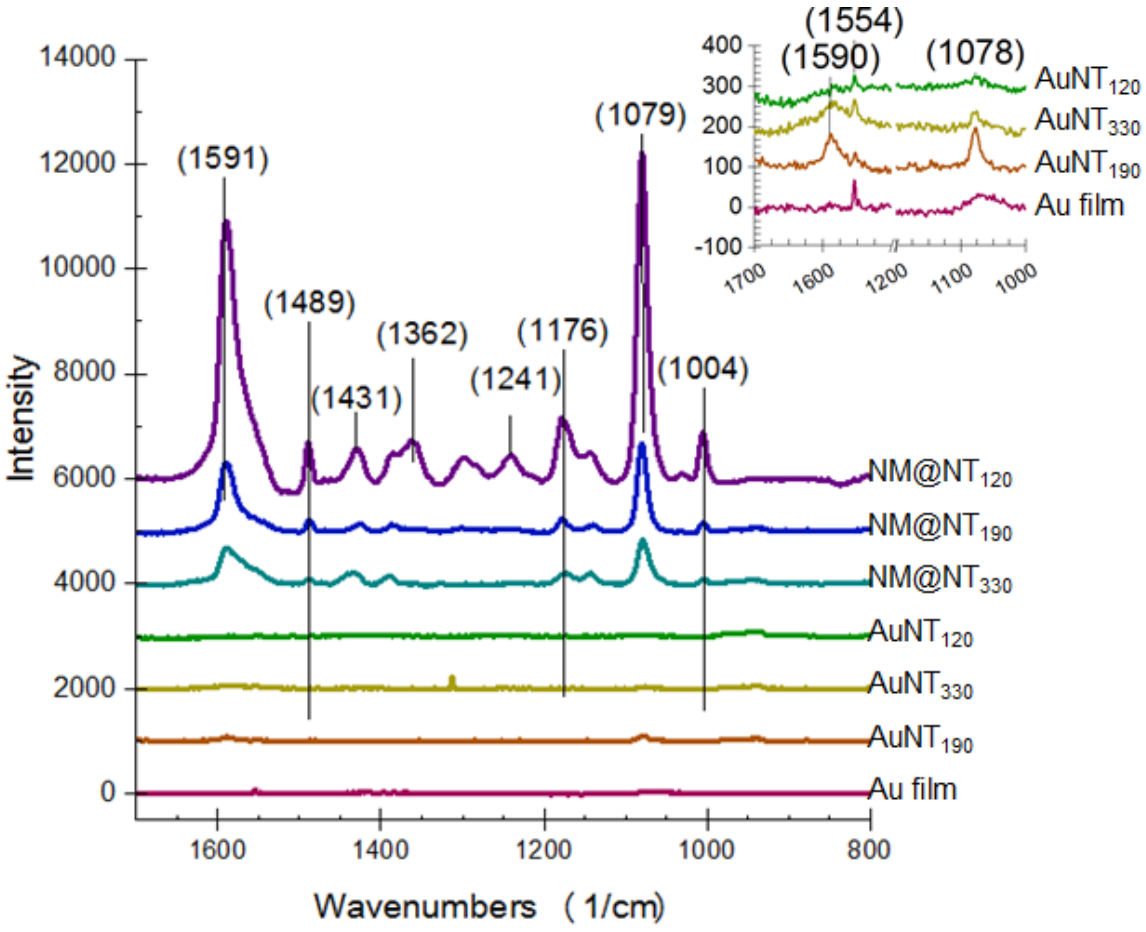

Figure 5.7 SERS spectra of 4-ATP on NM@NT and AuNT fabricated using 120, 190, and 330 nm polystyrene templates. Spectra were collected at 100 mW with a 785 nm laser source.

Table 5.3 Raman Peak Assignments[54-56]

Peak (cm^{-1})	Assignment	Peak (cm^{-1})	Assignment
1005	CC ring deformation	1362	VCC+δCH
1080	CS stretch	1431	δCH +VCC
1176	CH bend	1488	δCC + δCH
1241	δ CH in-plane	1590	C-C stretch

V = stretching, δ=bending

vibrations; (2) 1500-1350 cm^{-1} are C-C stretching with weak ring-breathing; (3) 1300-1000 cm^{-1} are CH in-plane bending vibrations.[54] The inset spectra show the intensity of the AuNTs and Au film for the 1079 cm^{-1} peak attributed to the C-S stretch of 4-ATP. The most intense peaks are from the NM@NT_{120} substrate followed by the NM@NT_{190} and NM@$NT_{330.}$ The largest 1079 cm^{-1} peak for the AuNT substrates is from the 190 nm template.

In the Raman spectra of the NM@NT, the C-C phenyl ring mode peak at 1591 cm^{-1} is asymmetric with a broadening towards 1500 cm^{-1}. By referencing the inset of AuNT, there is a defined peak at 1554 cm^{-1}. This peak has been found in many spectra and has been attributed to the NH_2 group and is likely the major contributor to the asymmetric peak at 1591 cm^{-1} for the NM@NT substrates.[57-59]

The footprint surface area of the nanoparticles and EFs are summarized in Table 5.4. Using the 1079 cm^{-1} peak, the EF and the relative EF of the decorated structure compared to the EF of the undecorated host structure was determined. The NM@NT_{120} had the largest relative enhancement over AuNT with a nearly 200-fold EF increase followed by the NM@NT_{330} and NM@NT_{190} substrates. The different intensities are

Table 5.4 Raman EF of three host template sizes: 120, 190, and 330 nm

Structure	Footprint Surface Area (%)	Peak Intensity 1079 cm^{-1}	EF	EF_{NM}/EF_{NT}
$NM@NT_{120}$	9	6214	2100	191
$AuNT_{120}$	5	18	11	-
$NM@NT_{190}$	6	1663	829	8.4
$AuNT_{190}$	3	97	98	-
$NM@NT_{330}$	16	843	419	22
$AuNT_{330}$	7	355	16	-

attributed to the resonance condition of the nanostructures, as shown in the normalized extinction spectra (Figure 5.5). The excitation wavelength is demarked on the extinction spectra by the vertical black line. Only the $NM@NT_{120}$ (Figure 5.5A) has a resonance overlap at 785 nm in the form of a shoulder off of the 550 nm peak. The $NM@NT_{190}$ (Figure 5.5B) and $NM@NT_{330}$ (Figure 5.5C) are both off resonance to the excitation wavelength (785 nm). The $NM@NT_{190}$ is blue shifted over 200 nm from the laser resonance and the $NM@NT_{330}$ is merely 100 nm from the laser resonance which corresponds well with the EFs; the $NM@NT_{330}$ EF is larger than the EF for the $NM@NT_{190}$.

The broader peak at 1000 nm for all substrates suggests that the contribution of the synthesis is also taking advantage of smaller islands and nanotriangle-dimers formed from poor close-packing of the very small nanosphere templates (Figure 5.6). This is not an intrinsically bad property; the nanomite synthesis is taking full advantage of the surface. However, this introduces a similar challenge that exists for aggregate-based SERS. Depending on the region of a substrate sampled by the probe, a greater or lesser portion of the islands may be present, which may impact reproducibility of the signal. It

would be more advantageous to use a larger template that produces particles with a dominant LSPR at 785 nm with more reliable template packing and future work will reflect this approach.

5.4 Conclusion

Refractive index sensitivity measurements and SERS show that the combination of top-down fabrication and bottom-up synthesis generates decorated nanostructures that are capable of increased sensitivity and increased enhancement. The sensitivity of the nanoparticles increased the EF one order of magnitude for SERS. However, the smallest template structures have poor packing that could lead to decreased reproducibility. This can be overcome by moving to larger templates that will have LSPR λ_{max} centered on the 785 nm. Future work will also evaluate the role of nanoparticle stability and storage.

5.5 References

1. Soares, L.; Csaki, A.; Jatschka, J.; Fritzsche, W.; Flores, O.; Franco, R.; Pereira, E. Localized Surface Plasmon Resonance (Lspr) Biosensing Using Gold Nanotriangles: Detection of DNA Hybridization Events at Room Temperature. *Analyst* **2014,** *139* (19), 4964-4973.

2. Doria, G.; Conde, J.; Veigas, B.; Giestas, L.; Almeida, C.; Assunção, M.; Rosa, J.; Baptista, P. V. Noble Metal Nanoparticles for Biosensing Applications. *Sensors* **2012,** *12* (2), 1657.

3. Raphael, M. P.; Christodoulides, J. A.; Mulvaney, S. P.; Miller, M. M.; Long, J. P.; Byers, J. M. A New Methodology for Quantitative Lspr Biosensing and Imaging. *Anal. Chem.* **2011,** *84* (3), 1367-1373.

4. He, X.; Wang, K.; Cheng, Z. In Vivo near-Infrared Fluorescence Imaging of Cancer with Nanoparticle-Based Probes. *Wiley Interdiscip. Rev. Nanomed. Nanobiotechnol.* **2010,** *2* (4), 349-366.

5. Aizpurua, J.; Hanarp, P.; Sutherland, D. S.; Käll, M.; Bryant, G. W.; García de Abajo, F. J. Optical Properties of Gold Nanorings. *Phys. Rev. Lett.* **2003,** *90* (5),

057401.

6. Hanarp, P.; Käll, M.; Sutherland, D. S. Optical Properties of Short Range Ordered Arrays of Nanometer Gold Disks Prepared by Colloidal Lithography. *J. Phys. Chem. B* **2003,** *107* (24), 5768-5772.

7. Neddersen, J.; Chumanov, G.; Cotton, T. M. Laser Ablation of Metals: A New Method for Preparing Sers Active Colloids. *Appl. Spectrosc.* **1993,** *47* (12), 1959-1964.

8. Kahl, M.; Voges, E.; Kostrewa, S.; Viets, C.; Hill, W. Periodically Structured Metallic Substrates for Sers. *Sens. Actuators, B* **1998,** *51* (1–3), 285-291.

9. Kennedy, B. J.; Spaeth, S.; Dickey, M.; Carron, K. T. Determination of the Distance Dependence and Experimental Effects for Modified Sers Substrates Based on Self-Assembled Monolayers Formed Using Alkanethiols. *J. Phys. Chem. B* **1999,** *103* (18), 3640-3646.

10. Sánchez-Cortés, S.; Domingo, C.; García-Ramos, J. V.; Aznárez, J. A. Surface-Enhanced Vibrational Study (Seir and Sers) of Dithiocarbamate Pesticides on Gold Films. *Langmuir* **2001,** *17* (4), 1157-1162.

11. Le, F.; Brandl, D. W.; Urzhumov, Y. A.; Wang, H.; Kundu, J.; Halas, N. J.; Aizpurua, J.; Nordlander, P. Metallic Nanoparticle Arrays: A Common Substrate for Both Surface-Enhanced Raman Scattering and Surface-Enhanced Infrared Absorption. *ACS Nano* **2008,** *2* (4), 707-718.

12. Küstner, B.; Gellner, M.; Schütz, M.; Schöppler, F.; Marx, A.; Ströbel, P.; Adam, P.; Schmuck, C.; Schlücker, S. Sers Labels for Red Laser Excitation: Silica-Encapsulated Sams on Tunable Gold/Silver Nanoshells. *Angew. Chem. Int.* **2009,** *48* (11), 1950-1953.

13. Bantz, K. C.; Meyer, A. F.; Wittenberg, N. J.; Im, H.; Kurtulus, O.; Lee, S. H.; Lindquist, N. C.; Oh, S.-H.; Haynes, C. L. Recent Progress in Sers Biosensing. *PCCP* **2011,** *13* (24), 11551-11567.

14. Mahurin, S. M.; John, J.; Sepaniak, M. J.; Dai, S. A Reusable Surface-Enhanced Raman Scattering (Sers) Substrate Prepared by Atomic Layer Deposition of Alumina on a Multi-Layer Gold and Silver Film. *Appl. Spectrosc.* **2011,** *65* (4), 417-422.

15. Bukasov, R.; Shumaker-Parry, J. S. Siver Nanocrescents with Infrared Plasmonic Properties as Tunable Substrates for Surface Enhanced Infrared Absorption Spectrscopy. *Anal. Chem.* **2009,** *81* (4531-4535).

16. Olejnik, M.; Agarwal, A.; Zaleszczyk, W.; Kotov, N. A.; Mackowski, S. Gold Nanoparticles with Elongated Shapes: Synthesis and Optical Properties. *Acta Phys. Pol., A* **2012,** *122* (2), 346-349.

17. Ming, L.; Scott, K. C.; Jianming, Z.; Jessica, L.; Zoraida, P. A.; Dongling, M.; Nianqiang, W. Shape-Dependent Surface-Enhanced Raman Scattering in Gold–Raman-Probe–Silica Sandwiched Nanoparticles for Biocompatible Applications. *Nanotechnology* **2012,** *23* (11), 115501.

18. Murazawa, N.; Ueno, K.; Mizeikis, V.; Juodkazis, S.; Misawa, H. Spatially Selective Nonlinear Photopolymerization Induced by the near-Field of Surface Plasmons Localized on Rectangular Gold Nanorods. *J. Phys. Chem. C* **2009,** *113* (4), 1147-1149.

19. Fales, A. M.; Vo-Dinh, T. Silver Embedded Nanostars for Sers with Internal Reference (Sensir). *J. Mater. Chem. C* **2015,** *3* (28), 7319-7324.

20. Fales, A. M.; Yuan, H.; Vo-Dinh, T. Development of Hybrid Silver-Coated Gold Nanostars for Nonaggregated Surface-Enhanced Raman Scattering. *J. Phys. Chem. C* **2014,** *118* (7), 3708-3715.

21. Indrasekara, A. S. D. S.; Meyers, S.; Shubeita, S.; Feldman, L. C.; Gustafsson, T.; Fabris, L. Gold Nanostar Substrates for Sers-Based Chemical Sensing in the Femtomolar Regime. *Nanoscale* **2014**.

22. Khoury, C. G.; Vo-Dinh, T. Gold Nanostars for Surface-Enhanced Raman Scattering: Synthesis, Characterization and Optimization. *J. Phys. Chem. C* **2008,** *112* (48), 18849-18859.

23. Novotny, L.; Bian, R. X.; Xie, X. S. Theory of Nanometric Optical Tweezers. *Phys. Rev. Lett.* **1997,** *79* (4), 645-648.

24. Jung, L. S.; Campbell, C. T.; Chinowsky, T. M.; Mar, M. N.; Yee, S. S. Quantitative Interpretation of the Response of Surface Plasmon Resonance Sensors to Adsorbed Films. *Langmuir* **1998,** *14*, 5636-56487.

25. Jensen, T. R.; Duval, M. L.; Kelly, K. L.; Lazarides, A. A.; Schatz, G. C.; Van Duyne, R. P. Nanosphere Lithography: Effect of the External Dielectric Medium on the Surface Plasmon Resonance Spectrum of a Periodic Array of Silver Nanoparticles. *J. Phys. Chem. B* **1999,** *103* (45), 9846-9853.

26. Bochenkov, V. E.; Frederiksen, M.; Sutherland, D. S. Enhanced Refractive Index Sensitivity of Elevated Short-Range Ordered Nanohole Arrays in Optically Thin Plasmonic Au Films. *Opt. Express* **2013,** *21* (12), 14763-14770.

27. Chen, H.; Kou, X.; Yang, Z.; Ni, W.; Wang, J. Shape- and Size-Dependent Refractive Index Sensitivity of Gold Nanoparticles. *Langmuir* **2008,** *24* (10), 5233-5237.

28. Cennamo, N.; D'Agostino, G.; Donà, A.; Dacarro, G.; Pallavicini, P.; Pesavento, M.; Zeni, L. Localized Surface Plasmon Resonance with Five-Branched Gold Nanostars in a Plastic Optical Fiber for Bio-Chemical Sensor Implementation.

Sensors (Basel, Switzerland) **2013,** *13* (11), 14676-14686.

29. Willets, K. A.; Van Duyne, R. P. Localized Surface Plasmon Resonance Spectroscopy and Sensing. *Ann. Rev. Phys. Chem.* **2007,** *58* (1), 267-297.

30. Loudon, R. The Raman Effect in Crystals. *Adv. Phys.* **1964,** *13* (52), 423-482.

31. Fontana, M. D.; Ben Mabrouk, K.; Kauffmann, T. H., Raman Spectroscopic Sensors for Inorganic Salts. In *Spectroscopic Properties of Inorganic and Organometallic Compounds: Techniques, Materials and Applications*, The Royal Society of Chemistry: 2013; Vol. 44, pp 40-67.

32. Moskovits, M. Surface-Enhanced Spectroscopy. *Rev. Mod. Phys.* **1985,** *57* (3), 783-826.

33. Moskovits, M. Surface-Enhanced Raman Spectroscopy: A Brief Retrospective. *J. Raman Spectrosc.* **2005,** *36* (6-7), 485-496.

34. Kneipp, K.; Kneipp, H.; Itzkan, I.; Dasari, R. R.; Feld, M. S. Ultrasensitive Chemical Analysis by Raman Spectroscopy. *Chem. Rev.* **1999,** *99* (10), 2957-2976.

35. Dieringer, J. A.; McFarland, A. D.; Shah, N. C.; Stuart, D. A.; Whitney, A. V.; Yonzon, C. R.; Young, M. A.; Zhang, X.; Van Duyne, R. P. Introductory Lecture Surface Enhanced Raman Spectroscopy: New Materials, Concepts, Characterization Tools, and Applications. *Faraday Discuss.* **2006,** *132* (0), 9-26.

36. Le Ru, E. C.; Blackie, E.; Meyer, M.; Etchegoin, P. G. Surface Enhanced Raman Scattering Enhancement Factors: A Comprehensive Study. *J. Phys. Chem. C* **2007,** *111* (37), 13794-13803.

37. Shumaker-Parry, J. S.; Rochholz, H.; Kreiter, M. Fabrication of Crescent-Shaped Optical Antennas. *Adv. Mater.* **2005,** (17), 2131-2134.

38. Bukasov, R.; Shumaker-Parry, J. S. Highly-Tunable Infrared Extinction Properties of Gold Nanocrescents. *Nano Lett.* **2007,** *7*, 1113-1118.

39. Haynes, C. L.; Van Duyne, R. P. Nanosphere Lithography: A Versatile Nanofabrication Tool for Studies of Size-Dependent Nanoparticle Optics. *J. Phys. Chem. B* **2001,** *105* (24), 5599-5611.

40. Vogel, N.; Goerres, S.; Landfester, K.; Weiss, C. K. A Convenient Method to Produce Close- and Non-Close-Packed Monolayers Using Direct Assembly at the Air–Water Interface and Subsequent Plasma-Induced Size Reduction. *Macromol. Chem. Phys.* **2011,** *212* (16), 1719-1734.

41. Xie, J.; Lee, J. Y.; Wang, D. I. C. Seedless, Surfactantless, High-Yield Synthesis of Branched Gold Nanocrystals in Hepes Buffer Solution. *Chem. Mater.* **2007,** *19*

(11), 2823-2830.

42. Ramsey, J. D.; Zhou, L.; Kyle Almlie, C.; Lange, J. D.; Burrows, S. M. Achieving Plasmon Reproducibility from Surfactant Free Gold Nanostar Synthesis. *New J. Chem.* **2015,** *39* (12), 9098-9108.

43. Cooper, C. T.; Rodriguez, M.; Blair, S.; Shumaker-Parry, J. S. Polarization Anisotropy of Multiple Localized Plasmon Resonance Modes in Noble Metal Nanocrescents. *J. Phys. Chem. C* **2014,** *118* (2), 1167–1173.

44. Lee, K.-S.; El-Sayed, M. A. Gold and Silver Nanoparticles in Sensing and Imaging: Sensitivity of Plasmon Response to Size, Shape, and Metal Composition. *J. Phys. Chem. B* **2006,** *110* (39), 19220-19225.

45. Martinsson, E.; Shahjamali, M. M.; Large, N.; Zaraee, N.; Zhou, Y.; Schatz, G. C.; Mirkin, C. A.; Aili, D. Influence of Surfactant Bilayers on the Refractive Index Sensitivity and Catalytic Properties of Anisotropic Gold Nanoparticles. *Small (Weinheim an der Bergstrasse, Germany)* **2016,** *12* (3), 330-342.

46. Otte, M. A.; Sepúlveda, B.; Ni, W.; Juste, J. P.; Liz-Marzán, L. M.; Lechuga, L. M. Identification of the Optimal Spectral Region for Plasmonic and Nanoplasmonic Sensing. *ACS Nano* **2010,** *4* (1), 349-357.

47. Minati, L.; Benetti, F.; Chiappini, A.; Speranza, G. One-Step Synthesis of Star-Shaped Gold Nanoparticles. *Colloids Surf., A* **2014,** *441* (0), 623-628.

48. Balasubramanian, S. K.; Yang, L.; Yung, L.-Y. L.; Ong, C.-N.; Ong, W.-Y.; Yu, L. E. Characterization, Purification, and Stability of Gold Nanoparticles. *Biomaterials* **2010,** *31* (34), 9023-9030.

49. Lacava, J.; Weber, A.; Kraus, T. Ageing of Alkylthiol-Stabilized Gold Nanoparticles. *Part. Part. Syst. Char.* **2015,** *32* (4), 458-466.

50. Gold Nanoparticles: Optical Properties. http://nanocomposix.com/pages/gold-nanoparticles-optical-properties (accessed Nov. 11, 2016).

51. Chechik, V. Reduced Reactivity of Aged Au Nanoparticles in Ligand Exchange Reactions. *J. Am. Chem. Soc.* **2004,** *126* (25), 7780-7781.

52. Haes, A. J.; Van Duyne, R. P. A Nanoscale Optical Biosensor: Sensitivity and Selectivity of an Approach Based on the Localized Surface Plasmon Resonance Spectroscopy of Triangular Silver Nanoparticles. *J. Am. Chem. Soc.* **2002,** *124* (35), 10596-10604.

53. Mazzotta, F.; Johnson, T. W.; Dahlin, A. B.; Shaver, J.; Oh, S.-H.; Höök, F. Influence of the Evanescent Field Decay Length on the Sensitivity of Plasmonic Nanodisks and Nanoholes. *ACS Photonics* **2015,** *2* (2), 256-262.

54. Gu, X.; Tian, S.; Zhou, Q.; Adkins, J.; Gu, Z.; Li, X.; Zheng, J. Sers Detection of Polycyclic Aromatic Hydrocarbons on a Bowl-Shaped Silver Cavity Substrate. *RSC Adv.* **2013,** *3* (48), 25989-25996.

55. Huang, Y.-F.; Wu, D.-Y.; Zhu, H.-P.; Zhao, L.-B.; Liu, G.-K.; Ren, B.; Tian, Z.-Q. Surface-Enhanced Raman Spectroscopic Study of P-Aminothiophenol. *PCCP* **2012,** *14* (24), 8485-8497.

56. Kim, K.; Lee, H. S. Effect of Ag and Au Nanoparticles on the Sers of 4-Aminobenzenethiol Assembled on Powdered Copper. *J. Phys. Chem. B* **2005,** *109* (40), 18929-18934.

57. Ji, W.; Spegazzini, N.; Kitahama, Y.; Chen, Y.; Zhao, B.; Ozaki, Y. Ph-Response Mechanism of P-Aminobenzenethiol on Ag Nanoparticles Revealed by Two-Dimensional Correlation Surface-Enhanced Raman Scattering Spectroscopy. *J. Phys. Chem. Lett.* **2012,** *3* (21), 3204-3209.

58. Talley, C. E.; Jusinski, L.; Hollars, C. W.; Lane, S. M.; Huser, T. Intracellular Ph Sensors Based on Surface-Enhanced Raman Scattering. *Anal. Chem.* **2004,** *76* (23), 7064-7068.

59. Kho, K. W.; Dinish, U. S.; Kumar, A.; Olivo, M. Frequency Shifts in Sers for Biosensing. *ACS Nano* **2012,** *6* (6), 4892-4902.

CHAPTER 6

CONCLUSION AND FUTURE WORK

6.1 Conclusion

This research presented several aspects of engineering the properties of plasmonic nanostructures: manipulating surface chemistry to improve thin film deposition, using atomic layer deposition (ALD) to probe the fundamental optical properties of gold nanocrescents (AuNCs) in the visible and infrared (IR), and generating novel structures for surface enhanced spectroscopy.

The use of ultra-violet ozone (UVO) exposure as a cleaning process for reactivating aged Au nanostructures and alumina (Al_20_3) films was explored.[1] The surfaces of Al_20_3 coated gold nanodisks (Al_20_3-AuNDs) were successfully reactivated as shown by the growth of additional Al_20_3 layers as deposited by ALD. The use of UVO is believed to increase the uniformity of the Al_20_3 nucleation by generating a hydrophilic surface. By systematically approaching the cleaning and deposition of heterogeneous surfaces composed of Au nanostructures supported on glass, it was also shown that the use of oxygen plasma etches both the AuNDs and Al_20_3-AuNDs. This is an important finding as defect-free films are a key component of nanostructure protection and fabrication optimization.

Ultra-thin films are a significant accomplishment for plasmonic substrates due to the exponential decay of the plasmon from the metal surface. As a protective film is being deposited, the sensitivity of the plasmon to the local environment decreases exponentially. By improving thin film deposition and increasing the hardiness of the nanostructures, the physical protection and sensitivity of plasmonic substrates become less of a trade-off and approach an ideal system: a plasmonic nanoparticle coated with a defect-free thin film with high sensitivity to the local environment.

Atomic layer deposition was used to investigate fundamental properties of gold nanocrescents (AuNCs) by probing the decay length and sensitivity over a broad spectral range of resonances. Along with the results from future theoretical work, these results will provide insight to the efficiency of nanocrescents in the IR.

A novel substrate for surface-enhanced spectroscopy was developed that incorporates affordable and simple methods from top-down fabrication and bottom-up synthesis. This approach used the simple and inexpensive technique of nanosphere lithography to fabricate arrayed gold nanotriangles (AuNTs) and a one-pot synthesis to generate branched decorations on fabricated structures. These “nanomite” decorated structures show excellent enhancement over the undecorated structures in SERS along with increased refractive index sensitivity. By applying this to AuNCs, we have also shown that any fabricated Au structure can serve as a host to the synthesis while maintaining polarization-dependent resonances. This hybrid substrate is a significant development because it will allow for high enhancement spectroscopies in complex solutions without the risk of aggregation and nanoparticle crashing.

In collaboration with the Chemistry at the Space Time Center, my research has

focused on three aspects of plasmonics: structure protection and surface chemistry regeneration with UVO cleaning, and fundamental understanding of plasmon decay of the gold nanocrescent, and increased LSPR sensitivity via the nanomite synthesis. The use of UVO to regenerate aged Au and Al_20_3 films has already been put in place for long-distance shipping between Utah and our collaborators' labs in California. In addition to addressing stability for shipping, the oxide coatings protect against structural damage and molecular desorption. Future work will expand on the details of optimization and surface modification of these processes.

6.2 Future Work

6.2.1 *Surface Chemistry of UVO and Oxygen Plasma*

The focus of UVO compared to oxygen plasma exposure studies were based on the LSPR response of AuNDs. Future work should focus on identifying the quantitative chemical changes of these two methods as they relate to quality of Al_20_3 film, including implementing transmission electron microscopy (TEM) and scanning TEM energy-dispersive X-ray spectroscopy (S/TEM-EDS). Cross-sectional TEM could provide information about the physical thickness of the Al_2O_3 films as well as changes in the diameter of the AuNDs as a function of treatment. This could also be used to determine if the thickness ratios of the Al_2O_3 change depending on the cleaning process. While we would anticipate that the LSPR shift is indicative of the height of the nanostructure as well as diameter, such detailed information could impact the treatment of smaller nanostructures or structures with finer details than AuNDs. To date, early results from this work has shown that these experiments are not trivial.

The need for thin TEM grids requires optimization of the fabrication process for the specific needs of the grid that do not necessarily reflect the reality of fabricated structures on traditional substrates of silicon and glass. Implementation of X-ray photoelectron spectroscopy could provide insight, but also has inherent challenges, mostly due to the fact that the surface is heterogeneous and this makes interpretation of the results averaged over large areas of the surface non-trivial. This is further complicated by the secondary sputtering during the fabrication process, which occurs when Ar^+ plasma is used to etch background gold, leading to an even more complex interface. To overcome some of these issues, work towards these goals has moved to using AuNTs and a defect visualization approach.

With the nanosphere lithography technique for AuNTs, harsh etching conditions are no longer necessary which was a significant impediment for using 5 nm lacy carbon grids required for TEM imaging of these structures. The defect visualization technique takes advantage of the reactivity series of metal using the galvanic replacement reaction between Au and platinum (Pt).[2-3] In this experiment, pinhole defects expose the Au surface of the nanostructure to the surrounding medium. This exposed Au serves as the source of the deposition of Pt particles (Figure 6.1). Followed by TEM and STEM-EDS analysis, the chemical surface of the nanostructure could be mapped and the defect density based on the cleaning techniques would be calculated.

In line with identifying the defects using STEM-EDS, the galvanic reaction has successfully performed on AuNTs fabricated on glass slides (Figure 6.2). However, scaling the fabrication and galvanic reaction from large glass slides to TEM grids have not yielded reproducible results. To improve upon this, moving away from fabricated

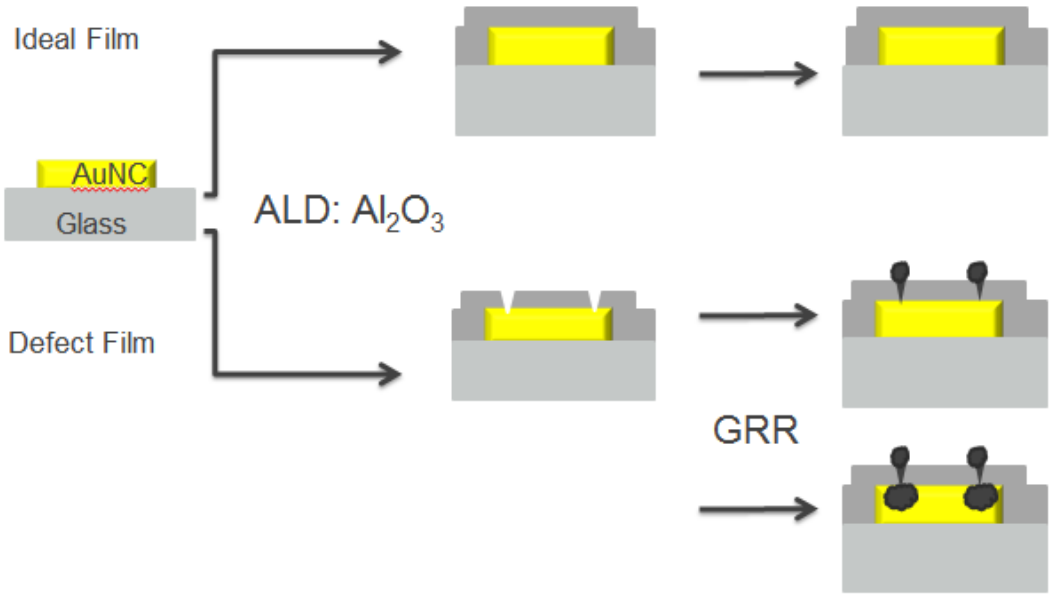

Figure 6.1 Platinum deposition scheme for pinhole defect visualization.

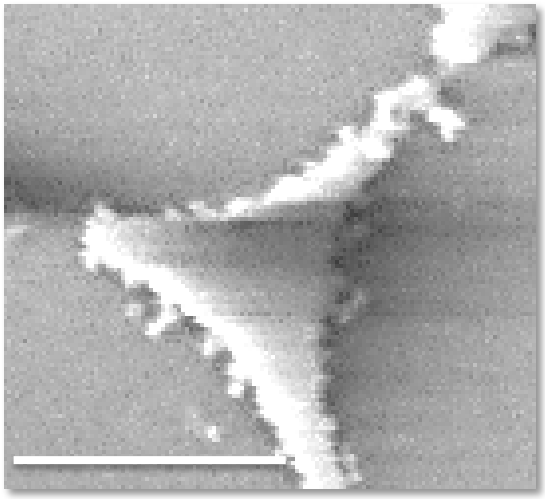

Figure 6.2 Platinum deposition on a AuNT.
Scale bar is 200 nm.

nanostructures may be necessary. By using gold-coated TEM grids, the impact of UVO and oxygen plasma can still be determined without the complications of sample fabrication and polystyrene template removal.

6.2.2 *Gold Nanocrescent Simulations in the IR*

Simulations are needed to determine the optical properties that are impacting the large nanocrescents that have resonances in the near-IR. It could be that the dielectric constant for the Au and Al_2O_3, though wavelength dependent in the simulations, does not accurately capture the physics of the nanoparticles because the values are based on films. An interesting approach could be to introduce grain boundaries and see how this affects the plasmonic resonance modes.

The geometry used for the finite-difference time-domain calculations was ideal: flat nanostructure, sharp tips with very little rounding. In collaboration with Dr. Nicolas Large and Dr. George Schatz, current work to address the theoretical and experimental mismatch includes developing a more realistic geometry of the AuNCs, such as rounded tips to modify the trend of the dispersion curves for the x-polarization. This is expected to decrease the sensitivity of the theoretical model and blue-shift the LSPR resonance. Studies using the adjusted geometry have shown much more accurate LSPR response for the smallest nanocrescent geometry investigated.[4] The tip-rounding is non-trivial in terms of development and computing cost, but current predictions are promising.

6.2.3 *Nanomite Synthesis*

The nanomite synthesis is a novel modification for fabricated structures and as such, the kinetics of the reaction and the physics of the nanomite structures, in terms of plasmonic response, are unknown. However, the initial work needs to identify the roles of ethanolamine, HEPES, and $AgNO_{3.}$ The apparent cooperativity of these capping and reducing agents could also be influenced by pH. Because the absence of ethanolamine yields nanomite decorations as well as nanoparticles in solution, the role of pH on the affinity of the piperazine ring to the non-crystalline host nanoparticles could signify a cooperative relationship between the HEPES and ethanolamine. Another option is that the host nanostructures are somehow donating the seeds or catalyzing the solution-based nanostar synthesis without requiring the nanostars to remain fixed to the substrate. Beyond these options, the production of nanostar byproducts could signify that ethanolamine only impacts the pH and beyond that, ethanolamine is simply a spectator in the synthesis.

The use of the host nanostructure as a catalyst is particularly interesting. If the solution is forming homogenously, that is the nanostar formation is solely based on the parent phase (the reaction solution), then the Gibbs free energy required to nucleate and then grow is favorable and the nanostructure is not required to catalyze the reaction. Determining if the host nanostructures are catalyzing the formation of the nanostars in solution, or if pH is the only factor, could provide experimental insight to the effect of pH on the surface free energy required for nucleation of the solution based nanostars. If catalyzing the formation of the nanostars in solution, the nanomite decorated substrates could provide a new route to nanoparticle synthesis over a broader range of experimental

conditions by decreasing the activation barrier of nucleation without requiring an additional synthesis for seed nanoparticles. If catalytically aiding the formation of stable nanostars at biological pH, the potential reusability of the NM@NT substrate for catalysis may be promising.

Another avenue of interest is introducing additional capping agents. While this deviates from the simple one-step synthesis scheme, the many branches of the NM can serve as the seeds to more advanced facet passivation methods. It is possible that minor changes in the current routine can also lead to longer branching, narrower arms, and interesting geometries.

6.3 References

1. Lancaster, C. A.; Shumaker-Parry, J. S. Surface Preparation of Gold Nanostructures on Glass by Ultraviolet Ozone and Oxygen Plasma for Thermal Atomic Layer Deposition of Al_2O3. *Thin Solid Films* **2016,** *612*, 141-146.

2. Podlovchenko, B. I.; Maksimov, Y. M.; Maslakov, K. I. Electrocatalytic Properties of Au Electrodes Decorated with Pt Submonolayers by Galvanic Displacement of Copper Adatoms. *Electrochim. Acta* **2014,** *130* (0), 351-360.

3. Straney, P. J.; Marbella, L. E.; Andolina, C. M.; Nuhfer, N. T.; Millstone, J. E. Decoupling Mechanisms of Platinum Deposition on Colloidal Gold Nanoparticle Substrates. *J. Am. Chem. Soc.* **2014,** *136* (22), 7873-7876.

4. McMahon, J. M.; Wang, Y.; Sherry, L. J.; Van Duyne, R. P.; Marks, L. D.; Gray, S. K.; Schatz, G. C. Correlating the Structure, Optical Spectra, and Electrodynamics of Single Silver Nanocubes. *J. Phys. Chem. C* **2009,** *113* (7), 2731-2735.

APPENDIX

SUPPORTING INFORMATION FOR CHAPTER 3

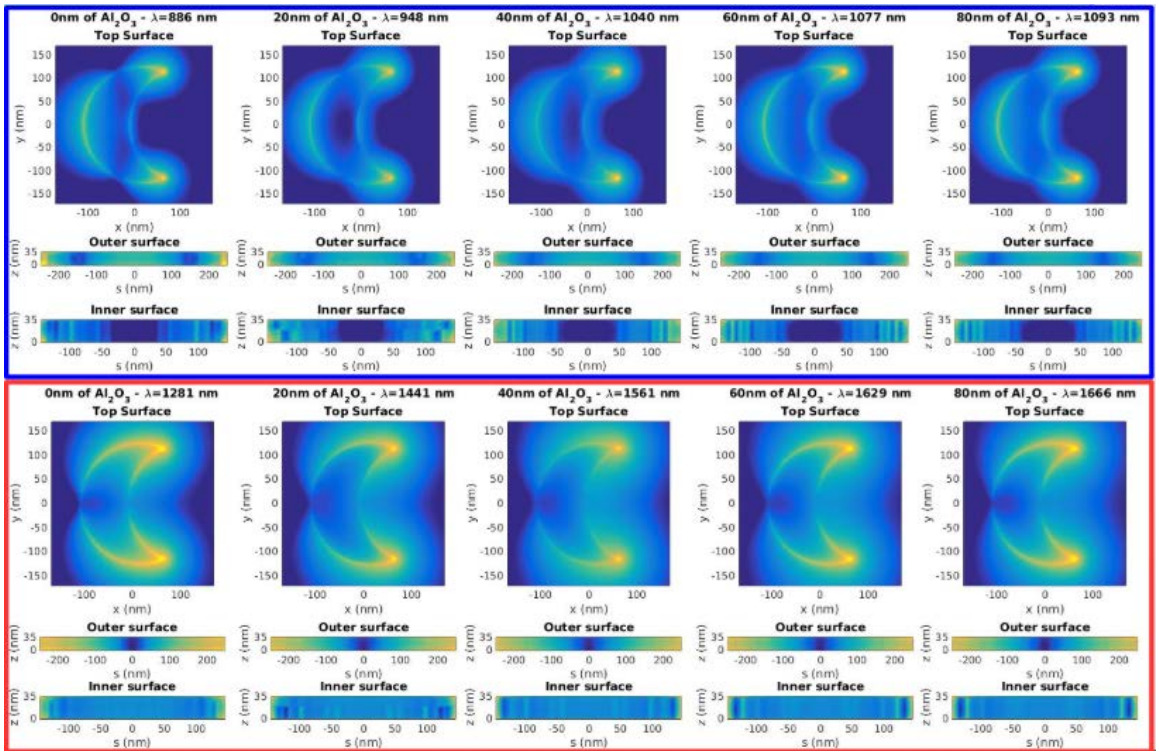

Figure A.1 Near-field distribution for $AuNC_{250}$.

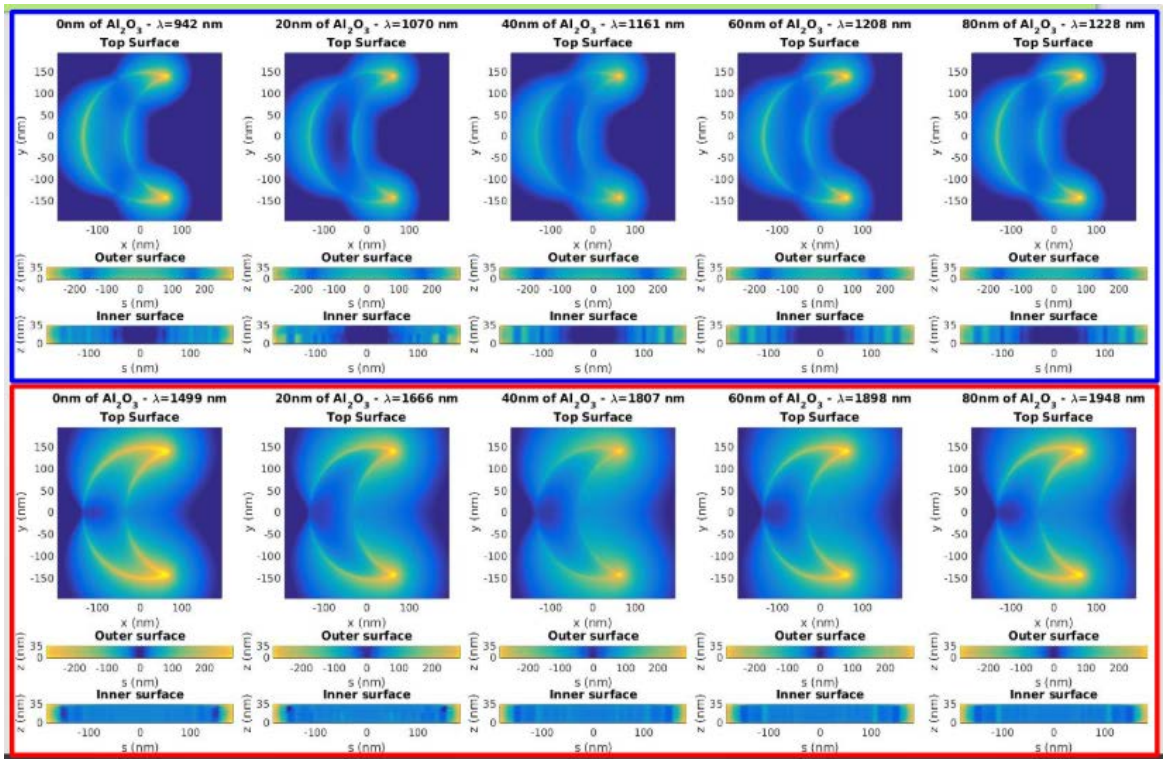

Figure A.2 Near-field distribution for $AuNC_{300}$.

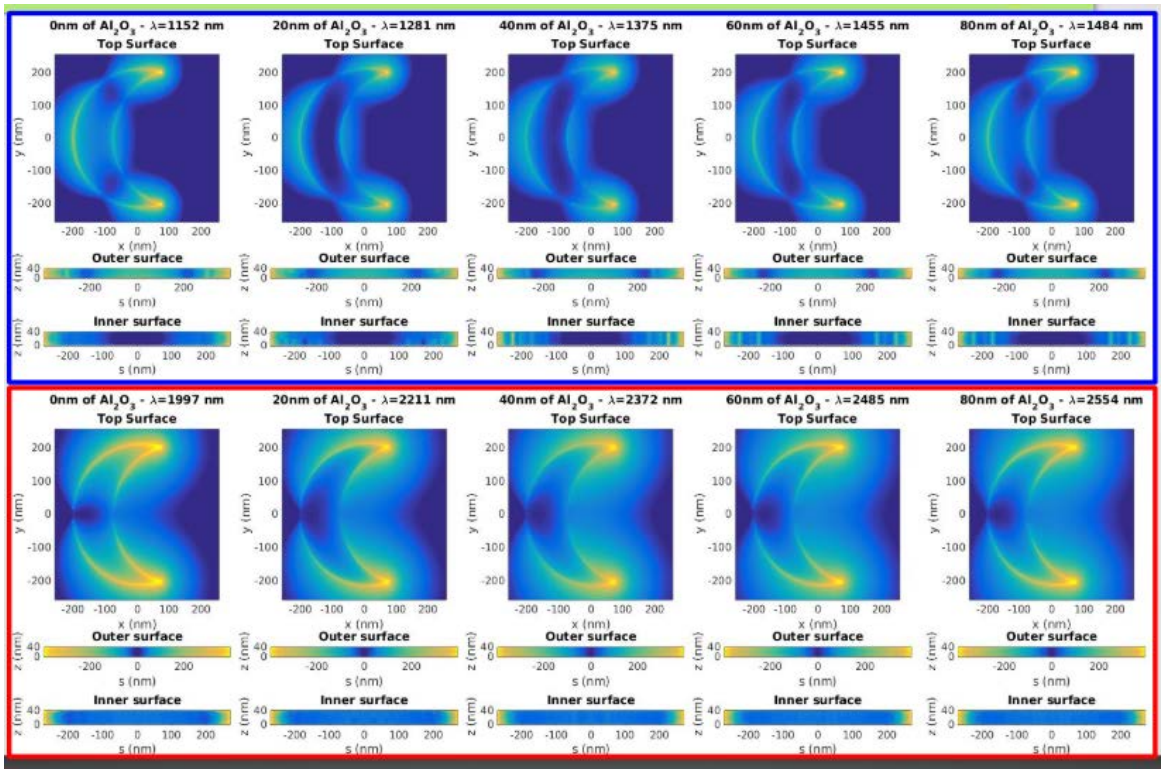

Figure A.3 Near-field distribution for $AuNC_{425}$.

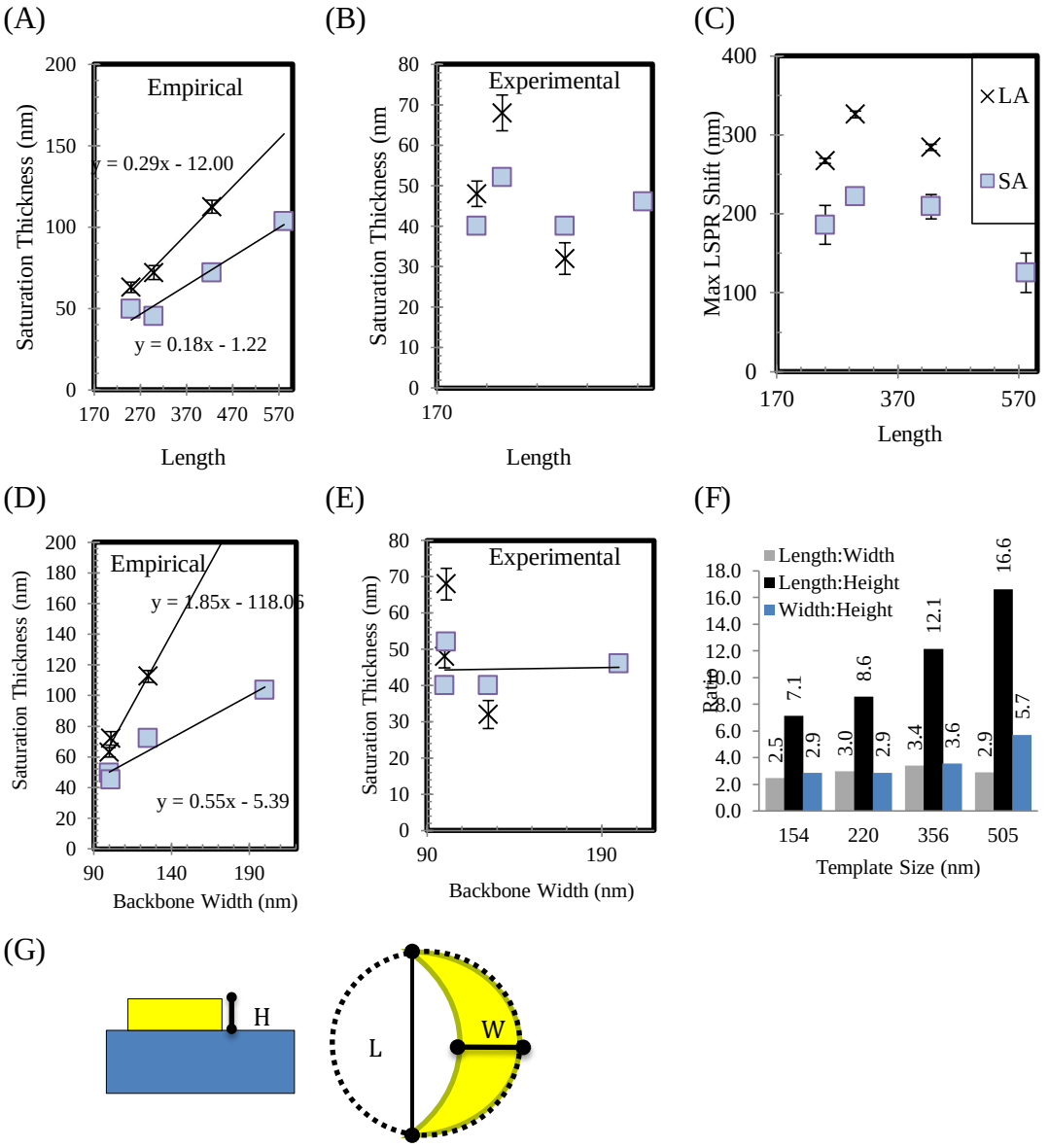

Figure A.4 Aspect ratio comparison of nanocrescents. (A) Saturation thickness (nm) versus length of nanocrescents based on the empirical fit of Eq. 3.1 to experimental data. (B) Saturation thickness (nm) versus length of nanocrescents based on the experimental data (C) Experimental average maximum LSPR shift (nm) of the nanocrescents compared to length (nm). (D) Saturation thickness (nm) versus backbone width of nanocrescents based on the analytical fit of Eq. 3.1 to experimental data. (E) Saturation thickness (nm) versus backbone width of nanocrescents based on the experimental data (F) Comparison of aspect ratios based on SEM images of nanocrescents for each template range. (G) Diagrams showing the length, width, and height measurements with respect to the nanocrescent geometry.